Numerical Simulations of Rarefied Gas Flows in Thin Film Processes

Development and Application of
a General Purpose DSMC Code

Numerical Simulations of Rarefied Gas Flows in Thin Film Processes

Development and Application of
a General Purpose DSMC Code

PROEFSCHRIFT

ter verkrijging van de graad van doctor
aan de Technische Universiteit Delft,
op gezag van de Rector Magnificus prof. dr. ir. J. T. Fokkema,
voorzitter van het College voor Promoties,
in het openbaar te verdedigen op
maandag 4 juni 2007 om 10:00 uur

door

Ruurd DORSMAN

natuurkundig ingenieur
geboren te Heinenoord

Dit proefschrift is goedgekeurd door de promotor:
Prof. dr. ir. C.R. Kleijn

Samenstelling promotiecommissie:

Rector Magnificus, voorzitter	
Prof. dr. ir. C.R. Kleijn,	Technische Universiteit Delft, promotor
Prof. dr. S.W. de Leeuw,	Technische Universiteit Delft
Prof. dr. D.J.E.M. Roekaerts,	Technische Universiteit Delft
Prof. dr. ir. A.A. van Steenhoven,	Technische Universiteit Eindhoven
Prof. dr. W.J. Goedheer,	FOM Instituut voor Plasmafysica Rijnhuizen en Universiteit Utrecht
Prof. dr.-ing. habil. G. Brenner,	Technischen Universität Clausthal

The work in this thesis was supported by The Netherlands Organisation for Applied Scientific Research TNO.

Keywords: gas flow, rarefied, Knudsen, simulation, DSMC, CVD, thin films, microfluidics

Printed by: Ponsen & Looijen B.V., www.p-l.nl

Respect and obey the Lord!
This is the beginning of knowledge.

Proverbs 1:7

Contents

Summary

Numerical Simulations of Rarefied Gas Flows in Thin Film Processes

Ruurd Dorsman, Delft University of Technology

Many processes exist in which a thin film is deposited from the gas phase, e.g. Chemical Vapor Deposition (CVD). These processes are operated at ever decreasing reactor operating pressures, reaching into the rarefied flow regime. The reason for this trend is that these low pressure conditions help improve the uniformity and the quality of the deposited film. Another important trend is a decrease of the dimensions of the structures that are deposited. For structures with a size of 70 nm, the gas flow can be characterized as rarefied even at atmospheric pressure.

At the same time, the use of numerical simulation tools for design and improvement of thin film deposition reactors is now widespread and generally accepted. These tools, however, are commonly based on continuum assumptions and cannot accurately account for rarefaction effects. Therefore, there is a need for numerical simulation tools capable of modeling rarefied internal gas flows. The work in this thesis is a first step in fulfilling this requirement. The aim is threefold: development, validation and application of a general purpose simulation tool for rarefied reacting internal gas flows.

To this end, the Direct Simulation Monte Carlo (DSMC) method was implemented in the 2D STARS and 3D X-Stream codes. The DSMC method was developed for high speed rarefied flow simulations in space applications, but is also suitable for low speed rarefied gas flows as e.g. found in inside deposition reactors.

After the implementation, validation of both codes was performed on a wide variety of problems, including low speed internal flows, supersonic flows, microfluidics, and thermal processes, as well as problems involving gas phase chemistry, trace species, surface interactions, and complicated geometries. Besides these flows, for which the data was taken from literature, a thin film deposition experiment was also designed and performed especially for the validation of the codes. The numerical results of the developed codes were very satisfactory in all cases, leading to the conclusion that the DSMC method in general, and the STARS and X-Stream codes specifically, are a very promising tool for use in internal rarefied gas flows, including thin film deposition processes.

Finally, the developed codes were used for calculations on three applications in the thin film industry, namely the heat transfer in a stagnation flow CVD reactor, thin film deposition through a shadow mask and the reaction rate of a gas at a surface with a reactive sticking coefficient.

The heat flux in the stagnation flow reactor was shown to be strongly dependent on the Knudsen (Kn) number, which is a measure for the rarefaction of the flow. For high Kn (which is the low pressure side of the rarefied flow regime), the heat flux profile was much more uniform than for low Kn, while the absolute heat flux decreased significantly. For low Kn, the DSMC results approached numerical continuum results obtained by commercial Computational Fluid Dynamics (CFD) codes.

For the deposition of a thin film through a shadow mask, the relation between the broadening of the deposited pattern and the distance between the mask and the substrate (the gap) was studied. In this case, the DSMC simulations were used to explain poorly understood experimental results, which showed an approximately square root relation between the gap size and the broadening. It was shown that the experimental results could be reproduced by the calculations. More importantly, also an explanation of the square root behavior could be given.

Finally, the STARS code was used to investigate a more fundamental issue, namely the reaction rate of a gas at a surface with a reactive sticking coefficient γ. An analytical theory exists for this reaction rate, but this theory is based on assumptions that are no longer valid in the rarefied flow regime. It was shown that the analytical theory is accurate for low values of γ, but that significant deviations of up to 35% can be expected for high values of γ. A correlation was developed to be able to predict this deviation as a function of the sticking coefficient and the near surface reactant mass fraction.

Samenvatting

Numerieke simulaties aan ijle gasstromingen in dunne laag processen

Ruurd Dorsman, Technische Universiteit Delft

Er bestaan veel verschillende processen, zoals bv. 'Chemical Vapor Deposition' (CVD), om vanuit de gasfase een dunne laag te deponeren. Deze processen worden bij steeds lagere druk uitgevoerd, zelfs tot in het ijle (*rarefied*) stromingsregime. De reden voor deze trend is dat de uniformiteit en de kwaliteit van de gedeponeerde lagen bij deze lage drukken sterk verbetert. Een andere belangrijke trend is de verkleining van de afmetingen van de gedeponeerde structuren. De gasstroming rond structuren met een afmeting van 70 nm kan, zelfs bij atmosferische druk, als *rarefied* beschreven worden.

Naast deze trends is het toepassen van programma's voor numerieke simulaties ten behoeve van het ontwerp en de verbetering van de dunne laag depositieprocessen wijdverbreid en algemeen geaccepteerd. Deze programma's zijn meestal echter gebaseerd op continuum aannames, en niet geschikt om *rarefied* effecten te modelleren. Er is dus duidelijk behoefte aan een programma dat in staat is om *rarefied* interne gasstromingen te berekenen. Het werk in dit boekje is een eerste stap om in die behoefte te voorzien. Het doel is drieledig: ontwikkeling, validatie en toepassing van een algemeen bruikbaar programma voor *rarefied* interne gasstromingen.

Om dit doel te bereiken is de Direct Simulation Monte Carlo (DSMC) methode in de 2D STARS en 3D X-Stream programma's geïmplementeerd. De DSMC methode is ontwikkeld voor berekeningen aan hoge snelheid *rarefied* gasstromingen in ruimtevaarttoepassingen, maar kan ook uitstekend toegepast worden bij lage snelheid *rarefied* gasstromingen zoals die in bv. depositiereactoren voorkomen.

Na de implementatie zijn beide programma's gevalideerd met een breed scala aan problemen, waaronder lage snelheid interne stromingen, supersone stromingen, microfluidics, en thermische processen, en ook problemen met gasfasechemie, met gassen in zeer lage concentraties, met oppervlakte-interacties en in ingewikkelde geometrieën. Naast deze stromingen, waarvan de benodigde gegevens in de literatuur bekend waren, is ook nog speciaal voor de validatie een dunne laag depositie-experiment opgezet en uitgevoerd. De resultaten van de berekeningen aan deze problemen waren zeer bevredigend, zodat geconcludeerd kan wor-

den dat de DSMC methode in het algemeen, en de STARS en X-Stream programma's in het bijzonder, veelbelovend zijn voor numerieke simulaties aan *rarefied* interne gasstromingen, inclusief dunne laag depositieprocessen.

De ontwikkelde programma's zijn uiteindelijk ook gebruikt voor berekeningen aan drie toepassingen in de dunne laag industrie, namelijk de warmteoverdracht in een stuwpuntsstromingsreactor (*stagnation flow* reactor), dunne laag depositie door een masker en de effectieve reactiesnelheid van gasmoleculen op een oppervlak met een gegeven reactiewaarschijnlijkheid.

De warmteoverdracht in een *stagnation flow* reactor bleek sterk afhankelijk te zijn van het Knudsen (Kn) getal, wat een maat is voor de ijlheid van het gas. Voor hoge Kn (wat overeenkomt met de lage druk kant van het *rarefied* stromings regime), was het profiel van de warmteoverdracht veel uniformer dan voor lage Kn, terwijl de absolute waarde van de warmteoverdracht significant verminderde. De DSMC resultaten bij lage Kn benaderden de resultaten die verkregen zijn met een commercieel 'Computational Fluid Dynamics' (CFD) programma.

In de studie naar dunne laag depositie door een masker is onderzoek gedaan naar het verband tussen de verbreding van het gedeponeerde patroon en de afstand tussen het masker en het substraat (de *gap*). In dit geval zijn de DSMC simulaties gebruikt om experimentele resultaten te verklaren. Deze onbegrepen resultaten lieten zien dat de verbreding bij benadering toeneemt met de wortel van de *gap* afstand. Er is aangetoond dat deze experimentele resultaten gereproduceerd konden worden met de berekeningen. Er is ook een verklaring gevonden voor de experimenteel bepaalde afhankelijkheid.

Als laatste is STARS ook gebruikt om onderzoek te doen naar een meer fundamenteel probleem, namelijk de reactiesnelheid van een gas bij een oppervlak met een gegeven reactiewaarschijnlijkheid γ. Er bestaat een analytische theorie voor deze reactiesnelheid, maar die is gebaseerd op aannames die niet geldig zijn in *rarefied* gasstromingen. Er is aangetoond dat de analytische theorie nauwkeurig is voor lage waarden van γ, maar dat er aanzienlijke afwijkingen van tot wel 35% kunnen optreden voor hoge waarden van γ. Er is een correlatie ontwikkeld om deze afwijkingen te kunnen voorspellen als functie van de reactiewaarschijnlijkheid en de massafractie van de reactant bij het oppervlak.

1. Introduction

1.1 Project background

1.1.1 Numerical simulation of gas flow

In many areas of science and industry, numerical simulation of gas flows has become an important tool for design and optimization of equipment. Almost all gas flows that are encountered can be computed by solving the continuum (Navier-Stokes) transport equations which describe the transport of mass, momentum and energy. These flows are characterized by the fact that the average mean free path λ of the gas molecules is very small in comparison to a characteristic dimension L of the flow. This dimension can be a physical dimension, e.g. a pipe diameter, or a flow dimension, e.g. the length scale $\left(\frac{1}{\phi}\frac{\partial\phi}{\partial x}\right)^{-1}$ on which some flow property ϕ changes significantly. The dimensionless Knudsen number Kn can be used to describe this situation:

$$\mathrm{Kn} = \frac{\lambda}{L} \tag{1.1}$$

If $\mathrm{Kn} < 0.01$, gas molecules travel only a small distance (compared to the geometry or flow dimensions) between collisions. For internal flows this means that molecules only very rarely collide with walls, and the flow is dominated by the characteristics of the inter-molecular collisions. The flow can then be described as a 'continuum' flow, which means that we can safely ignore the fact that a gas consists of many small particles. The continuum Navier-Stokes transport equations (including the continuum relations for the shear and the heat flux) can be used to calculate flow properties in this case.

Situations exist in which Kn is not so small, e.g. flows at low pressures, where λ becomes larger, or flows with a very small dimension L, e.g. microfluidics. The high Kn numbers in these flows indicate that a molecule travels a significant distance (compared to L) between collisions. For an internal flow, this implies that wall interactions occur more frequently and become important in describing the flow. The range where Kn is between $\sim$0.01 and $\sim$10 is called the rarefied or transitional regime. In this regime, the flow can no longer be described as a continuum and the well known transport equations, or more precisely, the equations for the viscosity and the heat flux, can no longer be used. In this regime, the particulate nature of

the gas becomes important and a different simulation method must be used.

Gas flows with Kn > 10 are called free molecular flows. In this regime, inter-molecular collisions rarely occur and the flow is completely dominated by the interaction between the gas and the walls.

1.1.2 Numerical simulations in different flow regimes

Numerical simulations in the continuum regime can be done using (commercially available) continuum Computational Fluid Dynamics codes based on partial differential equations describing the transport phenomena, e.g. the Navier-Stokes equations. Especially for laminar flows, these codes can produce accurate results for Knudsen numbers up to 0.01, but start deviating from reality for higher Kn. It is generally accepted that the range of applicability of these continuum codes can be extended into the rarefied regime up to Kn $\approx$ 0.1 by using special boundary conditions to take into account the possibility of a velocity slip or temperature jump at a surface.

Gas flows in the free molecular regime can be simulated using ray tracing of individual molecules with line-of-sight methods. As collisions with other gas molecules are very rare, only interactions with solid surfaces have to be taken into account. In the rarefied regime, both collisions with solid surfaces and other gas molecules are important, and have to be included in the simulation to obtain an accurate result. The Direct Simulation Monte Carlo (DSMC) method invented by Bird [1] is the only practical engineering method that can be used in the transitional regime. The DSMC method is also valid in the free molecular and continuum regimes, although the computational expenses become very large in the latter case.

1.2 Motivation and aim

The research described in this thesis was motivated by the fact that many processes (e.g. Chemical Vapor Deposition) used to deposit thin films on wafers in the IC industry are operated at ever decreasing reactor operating pressures. This pressure reduction is used to increase uniformity and quality of deposited layers.

Combined with the widespread use of numerical simulations for the design and optimization of thin film deposition equipment, this requires the availability of a simulation tool for internal reacting rarefied gas flows. For external flows (e.g. rarefied flow around space vehicles), a vast amount of literature and codes exists, but for internal flows as found in CVD, little is known.

The aim of this thesis is to describe the development, validation and application of a DSMC code that is specifically tailored for simulations of reacting rarefied internal gas flows. In subsequent chapters, the following research questions will be addressed:

1. Is the DSMC method a suitable tool for simulations of reacting rarefied gas flows as encountered in thin film process equipment? This question can be divided into three

essential parts:

(a) Can all relevant physical phenomena be incorporated?

(b) Are the results accurate?

(c) Are the computational efforts within reasonable limits?

These questions require a thorough investigation of the DSMC method, as well as a careful validation of the developed numerical code.

2. Can the DSMC method be integrated into a general purpose, 3D, non orthogonal CFD code for the purpose of simulations of thin film deposition equipment? If the DSMC method is to be applied in simulations of process equipment, complicated geometries should not be a problem. It will be investigated whether the DSMC method can be integrated into X-Stream, an existing general purpose CFD code.

3. Which experimental input data are required for DSMC simulations of thin film processes, and how critical are these to the accuracy of the simulation results?

4. What is the influence of rarefaction effects on quantities that are essential to thin film deposition, such as heat fluxes and reaction rates at surfaces?

In the future, the developed code and the acquired knowledge will be extended by other researchers, and applied to many problems in CVD and related fields. Besides applications in CVD, this knowledge will also be applied to other fields, such as e.g. microfluidics.

1.3 Rarefied flow simulations in the Department of Multi-Scale Physics

The work in this thesis marks the starting point of rarefied flow research at the Multi-Scale Physics department (part of the Applied Sciences faculty of the Delft University of Technology). Some 7 years ago, it was realized within this Department that in the field of research on Chemical Vapor Deposition, the need for low pressure numerical simulations would start growing rapidly. It was decided to take on the challenge to change the focus from continuum simulations using CFD to rarefied simulations using the DSMC method.

To date, 4 PhD candidates have been working on the development of a general purpose DSMC code, and the application of this code to internal rarefied gas flow problems. This does not only include low pressure simulations (e.g. vacuum equipment as used in CVD applications), but also microfluidics applications (e.g. microthrusters). The DSMC group led by Prof. Kleijn is one of a relatively small number of groups worldwide that is involved in research of *internal* rarefied gas flows.

1.4 Thesis outline

This thesis consists of 3 main parts: method, validation and application.

The numerical method is described in chapters 2 and 3. Chapter 2 gives a description of the specifics of the DSMC method that were used for the numerical simulations in this thesis. Chapter 3 provides the details of the implementation of this method in a 2D and a 3D code.

In chapters 4 and 5, extensive validation of the developed codes is performed to prove their value for the thin film deposition industry. The aim is to compare our DSMC results to experimental and numerical data from literature. For this comparison, a wide variety of problems will be investigated, including low speed internal flows, supersonic flows, microfluidics, thermal processes, gas phase chemistry, trace species, surface interactions, complicated geometries, and thin film deposition.

Chapter 4 describes validation against experimental and simulation data from literature, while chapter 5 gives the details of an experimental validation study that was performed by the author. This chapter describes an experiment that was designed especially for the purpose of validating DSMC codes. It will be shown that the developed DSMC codes can produce reliable results for all of these focal areas.

Chapters 6 and 7 demonstrate three example applications. These applications vary from practical applications in rarefied and free molecular flows (chapter 6), to the study of fundamental questions in thin film technology (chapter 7).

The first application is on the heat transfer in a very low pressure stagnation flow CVD reactor. The investigation will focus on the heat flux to the center of the susceptor and the uniformity of the heat flux across the susceptor for varying Knudsen and Péclet numbers. The results of the DSMC simulations will also be compared to continuum results.

The second application is on thin film deposition through a shadow mask. Previously, experiments were performed to study the broadening of the deposited film as a function of the distance between the substrate and the mask. The experimental results are poorly understood and this problem will be investigated using DSMC.

The third application is a more fundamental investigation of surface reaction models based on reactive sticking coefficients. For this problem, DSMC simulations will be performed to determine the accuracy of a commonly used theoretical model for the reaction rate. It will be investigated how large the model predictions deviate from the DSMC results, and whether it is possible to construct a correlation which is able to predict this deviation. The answers to these questions are relevant for continuum modeling of this type of boundary condition, which is often used in thin film deposition simulations.

This thesis ends with conclusions in chapter 8.

1.5 Acknowledgments

The research as described in this thesis was funded by the Netherlands Organization for Scientific Research (TNO). During this work, the author was a member of the J.M. Burger-

scentre Research School for Fluid Mechanics (JMBC). The support of these organizations is gratefully acknowledged.

2. The Direct Simulation Monte Carlo method

This chapter describes the basics of the Direct Simulation Monte Carlo (DSMC) method for numerical simulations of rarefied gas flows.

2.1 DSMC method overview

The DSMC method is not based on solving partial differential equations like the Navier-Stokes equations. Instead, it calculates the flow by calculating the paths and inter-molecular collisions of computational particles which represent molecules in the real flow. The position, velocity and internal energy of the computational particles are stored and updated each time step during a calculation. The two main assumptions of the method are:

- the decoupling of the translation of a computational particle and the collision with other computational particles, and
- the tracing of only a (very) small number of computational particles compared to the number of molecules in the real flow.

The first assumption means we can split each simulation time step into two steps:

- a movement step in which all computational particles are displaced and in which interactions with boundaries are computed, and
- a collision step in which inter-molecular collisions take place.

The second assumption means that it is not necessary to calculate the path of every real molecule, but that a small statistical sample is enough. The ratio F_{num}, which is defined as the ratio between the number of molecules in the real flow and the number of simulation particles, can be a very large number. In a simulation with multiple species, each computational particle thus represents F_{num} particles of a certain (single) species in the real flow.

From a more fundamental perspective, assumptions of dilute gas and molecular chaos are required also. In a dilute gas, the summed volume of all molecules occupies only a small fraction of the total volume. A consequence of this assumption is that the position and velocity distributions of two colliding particles are not correlated, which is the definition of molecular chaos. The same assumptions must be made in the derivation of the Boltzmann equation [2]. This equation mathematically describes a gas as a collection of particles with a certain distribution of their positions and velocities. It is generally accepted as the most basic equation that describes gas flows, and the Navier-Stokes equations can be derived from it. It has been shown [3] that the DSMC method converges to the Boltzmann equation in the limit of infinitely small cell size and time step, and infinite number of computational particles.

For some simple problems, the Boltzmann equation can be solved analytically, and numerical solutions can be obtained for a somewhat broader range of problems. For engineering problems, however, it is next to impossible to solve the Boltzmann equation, even numerically. An approximated form of the Boltzmann equation (e.g. using the Bhatnagar-Gross-Krook (BGK) model [4]) can be used in these cases, but this introduces errors in the solution. Another disadvantage of the Boltzmann equation is the fact that its definition does not include the possibility for chemical reactions. The DSMC method, being derived from the same physical principles as the Boltzmann equation, does not suffer from these shortcomings, and is therefore the preferred method for simulations of engineering type flows.

Figure 2.1 shows a typical DSMC calculation flow chart for a flow with a steady state solution. The steps in this flowchart will be discussed in the next sections.

2.2 Initialization

At the start of a computation, particles are generated in the flow domain according to the prescribed initial conditions. These conditions include a description of the flow domain, the initial number density n (for each of the species in the computation), the initial mass-average velocity $\vec{v}_{ma}$ and temperature T. The number of computational particles can be calculated using the prescribed value of F_{num} and the initial flow density. Each of these particles is then assigned a location, a velocity and a certain internal state for both rotational and vibrational modes. The location of the particles is chosen such that they are evenly distributed in the entire domain (for the most common case of a uniform initial density). The velocity of an individual particle is sampled from the Maxwellian distribution $f(\vec{v})$ appropriate for the initial temperature and the molecular mass m of the species which the particle represents [5]:

$$f(\vec{v}) = \left(\frac{m}{2\pi k_B T}\right)^{\frac{3}{2}} \exp\left[\frac{-m(\vec{v}-\vec{v}_{ma})\cdot(\vec{v}-\vec{v}_{ma})}{2k_B T}\right] \tag{2.1}$$

In this equation, k_B is the Boltzmann constant. The rotational and vibrational energy (if any) are also selected at random from their equilibrium distributions. For the rotational energy ϵ_r,

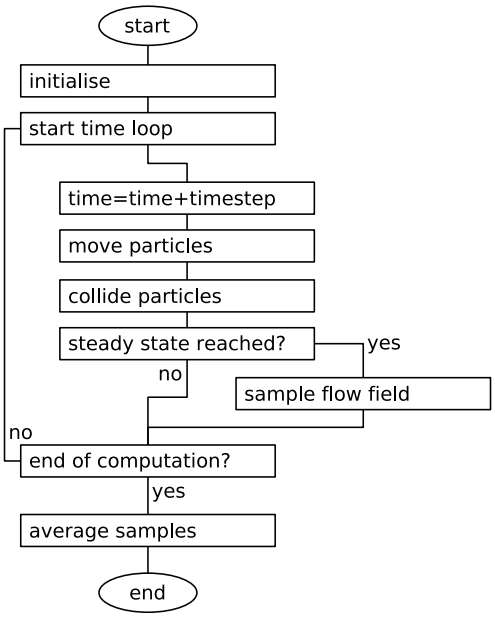

Figure 2.1: Typical DSMC flow chart.

which is treated in a classical way, this distribution is [6]:

$$f(\epsilon_r) \propto \epsilon_r^{\zeta/2-1} \exp\left[\frac{-\epsilon_r}{k_B T}\right] \tag{2.2}$$

Here, ζ is the number of rotational degrees of freedom. The vibrational energy is not treated in a classical way, but in a quantum harmonic oscillator model [6, 7]. The difference in the treatment of rotational and vibrational modes stems from the fact that the rotational modes are closely spaced and almost always fully excited (the characteristic temperatures are usually of the order of a few Kelvin). For this reason, rotational levels can be regarded as having a continuous energy distribution. For vibrational modes, the characteristic temperature is much higher (of the order of 1000 K) and the modes are widely spaced and rarely fully excited. Therefore, a quantum model is required for an accurate description of vibrational excitation. The vibrational energy ϵ_v is calculated from the discrete vibrational levels i_v and the characteristic vibrational temperature Θ as

$$\epsilon_v = i_v k_B \Theta \tag{2.3}$$

The distribution of the discrete vibrational levels is

$$f(i_v) \propto \exp\left[\frac{-i_v\Theta}{T}\right] \tag{2.4}$$

The number of degrees of freedom associated with a fully exited vibrational mode is 2. The number of rotational degrees of freedom and the characteristic temperature are species properties, and can be found in literature, e.g. [1].

2.3 Particle movement

In each DSMC time step, all computational particles are displaced. This calculation of the new location $\vec{x}_{t+\Delta t}$ is purely deterministic as the old location $\vec{x}_t$ and velocity $\vec{v}$ of each particle are known:

$$\vec{x}_{t+\Delta t} = \vec{x}_t + \vec{v} \cdot \Delta t \tag{2.5}$$

The consequences of equation 2.5 are different for 1D, 2D plane and 3D flows. For 1D flows, a computational particle needs only one location variable to uniquely define its position, and equation 2.5 will reduce to a scalar equation. For 2D plane and 3D flows, this equation becomes of order 2 and 3, respectively. In contrast to the treatment of the location, the particle velocity will always have 3 components, of which only the relevant components are used in equation 2.5. The reason for this is that the collision routines need the full 3D particle velocity.

In the case of 2D axisymmetric flows, the movement of a computational particle is treated completely 3D in Cartesian coordinates, and the new location is then transfered back to the appropriate 2D axisymmetric plane. This procedure is (schematically) shown in figure 2.2. The computational plane is indicated in this figure. All particles are located in this plane, and only 2 position variables are needed to describe their location. During the movement phase (using the full 3D version of equation 2.5), a particle will (starting from a position $\vec{x}_{old}$) leave this plane and end up in a location marked as $\vec{x}_{temp}$. The velocity (in plain Cartesian coordinates) does not change. The next step is to transfer the particle back to the computational plane, e.g. to position $\vec{x}_{new}$, *without* changing the axial and radial coordinate, and *without* changing the axial, radial and circumferential velocity components. In this step, the Cartesian velocity $\vec{v}_{old}$ changes to $\vec{v}_{new}$.

2.3.1 Boundary interaction

During the displacement of a computational particle, it might come in contact with a surface or an other boundary condition, e.g. an inlet or an outlet. If the path of a particle intersects with a solid surface, the interaction with this surface is calculated either as fully diffuse of fully specular [8]. In a diffuse reflection, the particle will be reflected with a velocity that is

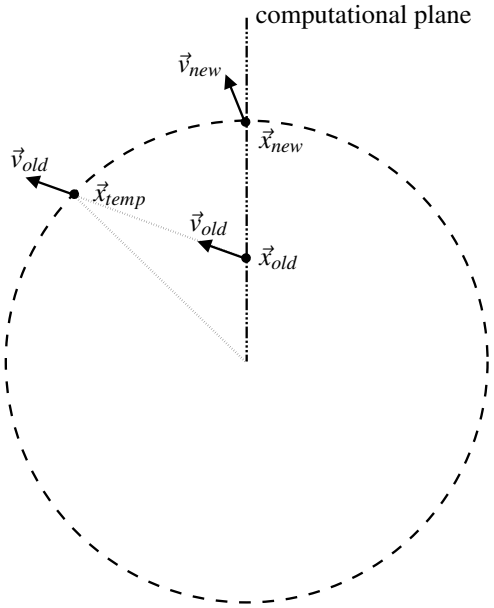

Figure 2.2: Schematic explanation of the displacement of a particle in 2D axisymmetric flows. Shown is a cross section of the flow normal to the flow axis.

sampled from the equilibrium velocity distribution in equation 2.1 with the surface temperature. The internal modes are also assigned new values which are taken from the equilibrium distributions (equations 2.2 and 2.4) for the surface temperature. For a specular reflection, only the velocity component normal to the wall is reversed, and all other particle properties remain equal. When a particle crosses an inlet or outlet boundary, it is removed from the simulation. A symmetry plane can also be used, its numerical implementation is identical to specular reflection at a surface.

During the movement phase of the calculation, new particles are also entered into the domain at the inlets and outlets. The number of new particles is calculated by assuming a Maxwellian velocity distribution (equation 2.1) with a given (predefined) number density (and species concentrations), average velocity and temperature. The individual particle properties are sampled from the equilibrium distributions (see section 2.2) for the inlet (or outlet) temperature and average velocity. An inlet or outlet boundary with fixed (predefined) properties will be referred to as a stream inlet or outlet boundary.

Mass flow inlet

A mass flow boundary is implemented as a combination of an inlet boundary and a diffuse wall. The required mass flow is converted to a net number of particles that must enter the computation at the mass flow boundary in a single time step. This number of particles is then introduced exactly as they would have been at a normal inlet boundary. To achieve the required mass flow, no particles are allowed to leave the domain at the mass flow inlet. Any particle coming from the flow domain and intersecting with the mass flow boundary will be reflected back diffusely as if a solid surface were present. This implementation exactly fixes the net mass flux to the specified value.

Pressure inlet and outlet

A pressure inlet and outlet is implemented as described by Piekos and Breuer [9]. For a pressure inlet, the temperature, pressure and species fractions are fixed, only the velocity is unknown. For a pressure outlet, only the pressure is fixed and the temperature, species fractions and velocity are unknown. The boundary is divided into sections and for each section the unknown variables are interpolated from the first cell in the flow nearest to the center of the section. The temperature and species fractions at the boundary are taken to be equal to their values in the cell, the velocity is multiplied by the particle number density ratio at the surface and in the cell to enforce conservation of mass.

The calculation of the boundary properties during the approach to steady state is done using a moving average filter of size N_{ma}, with typically $N_{ma} = 20$ samples. The reason for this is that, during the approach to steady state, the flow properties can change drastically. The values of the instantaneous average velocity, temperature and species fractions in the cell nearest to the surface section are calculated regularly as described in section 2.6. The statistical noise in this instantaneous sample is significant, but the moving average filter reduces this noise to an acceptable level. A more serious problem that applies only to the temperature calculation is the fact that the number of particles N in the cell is very small. It can be shown [10] that in this case, the statistically calculated temperature has a biased expectation value. The relative error between the biased estimate and the real temperature is equal to the inverse of the sample size N. To correct this, the correct local temperature T^* is determined from the calculated temperature T as:

$$T^* = T \cdot \frac{N}{N-1} \tag{2.6}$$

Sticking and accommodation coefficients

On diffusely reflecting surfaces, sticking and accommodation coefficients can be defined. The sticking coefficient γ ($0 \leq \gamma \leq 1$) is the probability that an impinging particle remains at the surface to become a part of the surface. In some cases one or more reaction products can be formed. If a sticking coefficient is defined for a surface, a random number is used to determine if surface sticking occurs for an individual incident particle.

The accommodation coefficient α ($0 \leq \alpha \leq 1$) is the fraction of impinging particles that will undergo diffuse reflection, while $(1-\alpha)$ is the fraction that reflects specularly. A surface with $\alpha = 1$ is thus a purely diffuse reflecting surface, while a surface with $\alpha = 0$ is purely specular reflecting. A random number is used to determine if an impinging particle will reflect diffusely or specularly. Different sticking and accommodation coefficients can be defined for different species and surfaces, but for $\gamma = 1$, the value of α has no meaning or relevance.

2.4 Particle collisions

The collisions are calculated using a Monte Carlo type scheme, hence the name Direct Simulation Monte Carlo. For this purpose, the simulation domain is divided into cells with maximum dimensions $(\lambda/3)\cdot(\lambda/3)\cdot(\lambda/3)$, or an equivalent 1D or 2D representation. In each time step, the collisions between the N computational particles in a cell can be calculated using the number of pairs and the collision probability P for each pair:

$$\#\text{pairs} = \frac{N(N-1)}{2} \tag{2.7}$$

$$P = F_{num}\frac{\Delta t \sigma_T c_r}{V} \tag{2.8}$$

In these equations, F_{num} is the ratio between the number of real molecules and the number of computational particles, σ_T is the total collision cross-section of the two particles, c_r the relative speed of the two particles, Δt is the time step and V is the volume of the cell. The fraction $\frac{\sigma_T c_r \Delta t}{V}$ is the probability that the computational particles will collide in a time step, the factor F_{num} is included to obtain the correct collision frequency. This method of calculating collisions is not very efficient as the value of P is usually very small. DSMC calculations therefore use an adapted method in which the number of pairs is reduced such that the collision probability for a pair can be increased:

$$\#\text{pairs} = \frac{1}{2}N^2 F_{num}\frac{\Delta t (\sigma_T c_r)_{max}}{V} \tag{2.9}$$

$$P = \frac{\sigma_T c_r}{(\sigma_T c_r)_{max}} \tag{2.10}$$

The value of $(\sigma_T c_r)_{max}$ has to be estimated at the start of a calculation, and must be adjusted if a higher value is found during the calculations. Note that the product of the number of pairs and P is not exactly the same in both cases:

$$\frac{P\cdot\#\text{pairs (eqs. 2.7 and 2.8)}}{P\cdot\#\text{pairs (eqs. 2.9 and 2.10)}} = \frac{N-1}{N} \tag{2.11}$$

Taking the true physics (with a very large number of molecules) into account, it can be seen that the product $P\cdot\#\text{pairs}$ should ideally be calculated as:

$$P\cdot\#\text{pairs} \propto N(F_{num}N - 1) \tag{2.12}$$

As $F_{num}N$ is usually extremely large compared to unity, the right hand side reduces to N^2F_{num}. As a result, the second method (equations 2.9 and 2.10) of calculating the collisions is physically correct.

The above equations can be easily extended to a gas mixture, resulting in an equation for the number of pair selections for collisions between species i and species j particles

$$\#\text{pairs}_{ij} = \frac{1}{2} N_i N_j F_{num} \frac{\Delta t \left((\sigma_T c_r)_{ij} \right)_{max}}{V} \tag{2.13}$$

The equation for the collision probability of the selected pair changes to

$$P = \frac{\sigma_T c_r}{(\sigma_T c_r)_{ij,max}} \tag{2.14}$$

For each of the total number of pairs, a pair of computational particles is selected from the cell at random. This means that their paths do not need to intersect, nor do they have to be close in physical space. This does not have a significant effect on the results, as long as the cell dimensions are smaller than $\lambda/3$. To further decrease the effect of the separation, a cell is divided into sub cells, and a pair is selected from the same sub cell if possible. The probability P is evaluated for each pair and a collision is accepted or rejected by comparing P to a random number.

2.4.1 Collision models

Collision models are used to determine the collision cross-section σ_T and the post-collision properties (velocity, internal energy) of the computational particles. Naturally, the locations of the particles are not changed during a collision. The parameters of a collision model determine the collision frequency of particles and the transfer of momentum and energy during a collision. On the macroscopic scale, these parameters determine the diffusion coefficient and the viscosity of the gas.

Two different collision models are used frequently in DSMC, namely the Variable Hard Sphere (VHS) [11] and the Variable Soft Sphere (VSS) [12, 13] models. Both of these models calculate a collision cross section $\sigma_T = \frac{\pi}{4} d^2$, with d the collision diameter which is a function of the relative velocity c_r of the two molecules:

$$d = d_{ref} \left[\left(\frac{2 k_B T_{ref}}{m_r c_r^2} \right)^{\omega - \frac{1}{2}} \frac{1}{\Gamma\left(\frac{5}{2} - \omega\right)} \right]^{\frac{1}{2}} \tag{2.15}$$

In this equation, k_B is the Boltzmann constant and m_r is the reduced mass:

$$m_r = \frac{m_1 \cdot m_2}{m_1 + m_2} \tag{2.16}$$

The reference diameter d_{ref}, the reference temperature T_{ref} and the viscosity-temperature exponent ω are parameters of the VHS and VSS model that can be derived from macroscopic gas properties (see section 2.4.2). The cross-section σ_T as required for equations 2.13 and 2.14 is defined (for a collision between particles of type i and j) as

$$\sigma_T = \frac{\pi}{4}(d_i + d_j)^2 \tag{2.17}$$

When a collision occurs, the deflection angle χ is given by

$$cos\left(\frac{\chi}{2}\right) = \left(\frac{b}{d}\right)^{\frac{1}{\alpha}} \tag{2.18}$$

In this equation, b is the miss distance (an impact parameter) and α is a VSS model parameter. For the VHS model, α is unity. The value of b is not known in a DSMC collision because the paths of the computational particles in a collision do not cross. As the ratio $\left(\frac{b}{d}\right)^2$ is distributed uniformly between 0 and 1, equation 2.18 is rewritten as

$$cos(\chi) = 2\left(\frac{b}{d}\right)^{\frac{2}{\alpha}} - 1 \tag{2.19}$$

For each collision, a value for χ can now be obtained easily using a single random number.

While the difference between the VHS and VSS models seems small, the inclusion of the α parameter has a significant influence. The VHS model can accurately reproduce the coefficient of viscosity μ, including a (realistic) temperature dependence in the form of $\mu \propto T^{\omega}$. The VSS model, through the inclusion of the parameter α, is also capable of accurately predicting the coefficient of (self) diffusion D and its temperature dependence, which the VHS model cannot.

Exchange of internal energy

During molecular collisions, not only momentum and translational energy, but also internal (rotational and vibrational) energy exchange may take place. This exchange is modeled using the Larsen-Borgnakke method [14, 15]. In every collision, every internal mode of both molecules is subjected to possible relaxation. Relaxation does not occur in every collision, this is controlled by a (predefined) relaxation time, which is usually defined in terms of an average number of collisions between relaxation. A separate random number procedure is applied to each internal mode in turn. If the relaxation is accepted for a specific internal mode with ζ_{int} degrees of freedom and energy $E_{int,old}$, the general Larsen-Borgnakke distribution function

$$f\left(\frac{E_{int,new}}{E_t}\right) = \frac{\Gamma(\zeta_{int}/2 + \zeta_{trans}/2)}{\Gamma(\zeta_{int}/2)\Gamma(\zeta_{trans}/2)}\left(\frac{E_{int,new}}{E_t}\right)^{\zeta_{trans}/2-1}\left(\frac{E_{trans,new}}{E_t}\right)^{\zeta_{int}/2-1} \tag{2.20}$$

is used to calculate the new energy $E_{int,new}$ in that mode. The translational mode (with relative translational energy E_{trans} and $\zeta_{trans} = 5 - 2\omega$ degrees of freedom, in which ω is the viscosity-temperature exponent taken from the VHS or VSS model) is used as an energy reservoir, and $E_t = E_{int,old} + E_{trans,old} = E_{int,new} + E_{trans,new}$ is the total available energy. During relaxation, a random value of $E_{int,new}$ is chosen with a probability according to equation 2.20. The relative translational energy is adjusted accordingly to keep the total energy constant.

2.4.2 Derivation of VHS/VSS parameters

For some species, the VHS and/or VSS parameters have been tabulated [1, 12, 13], but for many species they are unknown. Fortunately, Lennard-Jones parameters are available much more abundantly and the VHS/VSS parameters can be calculated from them. The calculation consists of 2 main steps:

1. calculation of the viscosity and diffusion coefficients (as a function of temperature) from kinetic gas theory [16] and Lennard-Jones parameters, and
2. calculation of the VHS/VSS parameters from these coefficients and their temperature dependence.

Calculation of viscosity and diffusion coefficients

First we define the following reduced temperatures T^* for species i and species i and j:

$$T_i^* = \frac{k_B T}{\epsilon_i} \tag{2.21}$$

$$T_{ij}^* = \frac{k_B T}{\sqrt{\epsilon_i \epsilon_j}} \tag{2.22}$$

In these equations, ϵ is the Lennard-Jones potential parameter[1]. With the tabulated integral functions $\Omega_\mu(T_i^*)$ and $\Omega_D(T_{ij}^*)$ [16], the following equation can now be used to determine the dynamic viscosity μ of a gas of species i [16, 17, 18] [2] :

$$\mu_i = \frac{5}{16} \frac{\sqrt{\pi M_i RT}}{\pi \sigma_i^2 N_A \Omega_\mu(T_i^*)} \tag{2.23}$$

In this equation, σ is the Lennard-Jones diameter (in m)[3], M is the molar mass (in kg/mol), R is the universal gas constant and N_A is Avogadro's number. The binary diffusion coefficient

[1] Please note that often the value of ϵ/k_B is tabulated (in K). In equations 2.21 and 2.22 the dimension of ϵ is J.

[2] The thesis by Kuijlaars [18] seems to contain a misprint in the equations for viscosity and the diffusion coefficient, including an erroneous factor of 10^{-20} in both equations.

[3] Please note that often the value of σ is tabulated in Å.

$\mathbb{D}_{ij}$ of species i and j can be calculated as [16, 17, 18] [2] :

$$\mathbb{D}_{ij} = \frac{3}{16} \frac{\sqrt{2\pi R^3 T^3}}{pN_A \pi \frac{1}{4}(\sigma_i + \sigma_j)^2 \Omega_{\mathbb{D}}(T^*_{ij})} \sqrt{\left(\frac{M_i + M_j}{M_i M_j}\right)} \tag{2.24}$$

Note that $\mathbb{D}_{ij}$ depends both on temperature T and pressure p. Equation 2.24 can be written (using SI units) as

$$\mathbb{D}_{ij} = 5.9551 \times 10^{-24} \frac{\sqrt{T^3}}{p \frac{1}{4}(\sigma_i + \sigma_j)^2 \Omega_{\mathbb{D}}(T^*_{ij})} \sqrt{\left(\frac{M_i + M_j}{M_i M_j}\right)} \tag{2.25}$$

in which the constant 5.9551 $J^{3/2}K^{-3/2}mol^{-1/2}$ is often replaced by the more accurate Wilke-Lee relation [19]:

$$6.77 - 0.0492 \sqrt{\left(\frac{M_i + M_j}{M_i M_j}\right)} \tag{2.26}$$

VSS parameters for a single species

This section describes the method to derive the VHS/VSS model parameters from the Lennard-Jones parameters for a single species. The required VSS parameters for a single species are:

- molecular mass m,
- reference temperature T_{ref},
- viscosity temperature exponent ω,
- VSS parameter α, and
- reference diameter d_{ref} at temperature T_{ref}.

The molecular mass m is simply the 'real-life' mass of one atom or molecule. The parameter ω can be determined using its definition:

$$\mu \propto T^{\omega} \tag{2.27}$$

The procedure to determine ω is simple. Using equation 2.23, the value of the viscosity is determined for several temperatures in a temperature range between a certain T_{low} and T_{high}. This range should reflect the expected temperature range present in the simulations. The power curve in equation 2.27 is then used to fit these points using a least squares fit. The reference temperature T_{ref} is calculated as the average of the temperature range used:

$$T_{ref} = \frac{T_{low} + T_{high}}{2} \tag{2.28}$$

The value of α can be deduced from the following relation between viscosity and the diffusion coefficient [1]:

$$\frac{\mu_{ref}}{\rho_{ref}(\mathbb{D}_{ii})_{ref}} = \frac{2+\alpha}{\frac{3}{5}(7-2\omega)\alpha} \tag{2.29}$$

The viscosity μ_{ref} and the self-diffusion coefficient $(\mathbb{D}_{ii})_{ref}$ at the reference temperature T_{ref} can be easily calculated using equations 2.23 and 2.24-2.26. Using the ideal gas law, ρ_{ref} is evaluated at the reference temperature. Note that $\mathbb{D}_{ii} \propto 1/p$ and $\rho \propto p$, meaning that α does not depend on the pressure. Also note that according to Bird [1] 'it is not clear whether α can reasonably be regarded as a constant in applications that involve large changes in temperature.' If VHS parameters are required, α is simply set to unity.

Finally, the reference diameter d_{ref} follows from [1]:

$$d_{ref} = \sqrt{\frac{5(\alpha+1)(\alpha+2)\sqrt{(mk_BT_{ref}/\pi)}}{4\alpha(5-2\omega)(7-2\omega)\mu_{ref}}} \tag{2.30}$$

Again, μ_{ref} can be easily calculated using equation 2.23.

VSS parameters for multiple species

This section describes the method to derive the VHS/VSS model parameters from the Lennard-Jones parameters for collisions between unlike particles. These are the required VSS parameters for collisions between species i and j particles:

- reduced mass m_r,
- reference temperature $(T_{ij})_{ref}$,
- reference diameter $(d_{ij})_{ref}$,
- viscosity temperature coefficient ω_{ij}, and
- VSS parameter α_{ij}.

The reduced mass m_r is calculated as:

$$m_r = \frac{m_i m_j}{m_i + m_j} \tag{2.31}$$

The reference diameter $(d_{ij})_{ref}$ and temperature $(T_{ij})_{ref}$ are simply calculated as the average of the individual species parameters, as determined from the theory in the previous section:

$$(d_{ij})_{ref} = \frac{(d_i)_{ref} + (d_j)_{ref}}{2} \tag{2.32}$$

$$(T_{ij})_{ref} = \frac{(T_i)_{ref} + (T_j)_{ref}}{2} \tag{2.33}$$

The value of ω_{ij} can be determined using the temperature dependence of the diffusion coefficient [1]:

$$\mathbb{D}_{12} \propto T^{\omega_{ij}+1} \tag{2.34}$$

Using equations 2.24-2.26, the value of ω_{ij} can easily be determined by using a least squares fit. Finally, the value of α_{ij} can be determined using this equation [1]:

$$\alpha_{ij} = \frac{8(5-2\omega_{ij})n_{ref}(\mathbb{D}_{ij})_{ref}\pi(d_{ij})_{ref}^2}{3\sqrt{2\pi k_B(T_{ij})_{ref}/m_r}} - 1 \tag{2.35}$$

The values of $(\mathbb{D}_{ij})_{ref}$ and n_{ref} are evaluated at temperature $(T_{ij})_{ref}$ using equations 2.24-2.26 and the ideal gas law. Again, the product $n_{ref}(\mathbb{D}_{ij})_{ref}$ is not dependent on the pressure so α_{ij} can be assigned a pressure-independent value. The discussion about the temperature range for which α_i is valid (below equation 2.29) also applies here.

The computations described in this thesis do not use equations 2.34 and 2.35, but simply calculate ω_{ij} and α_{ij} as

$$\omega_{ij} = \frac{\omega_i + \omega_j}{2} \tag{2.36}$$

and

$$\frac{1}{\alpha_{ij}} = \frac{1}{2}\left(\frac{1}{\alpha_i} + \frac{1}{\alpha_j}\right) \tag{2.37}$$

This is the same approach as taken in the authoritative DSMC reference book [1]. Tables 2.1 and 2.2 contain the VSS parameters of helium, argon and nitrogen as calculated using the theory above, and as listed in the reference book. The differences between the different parameter sets can be attributed to the inaccurate method of first converting measurements (of viscosity and diffusion) to L-J parameters and then converting the L-J parameters to VSS parameters. In general, VSS parameters from literature (which are usually determined directly from measurements of viscosity and diffusion) are preferred over VSS parameters that have been calculated from L-J parameters.

2.4.3 Calculation of the mean free path

When it comes to the determination of the mean free path λ in a gas, several methods are used. The first method (of the two that are used in this thesis) can be derived from the VHS or VSS collision model, and will be referred to as λ_{VHS}. For species i in a mixture with s species, the mean free path $\lambda_{VHS,i}$ is written as:

$$\frac{1}{\lambda_{VHS,i}} = \sum_{j=1}^{s}\left[\pi(d_{ij})_{ref}^2 n_j \left(\frac{(T_{ij})_{ref}}{T}\right)^{\omega_{ij}-1/2}\left(1+\frac{m_i}{m_j}\right)^{1/2}\right] \tag{2.38}$$

In this equation, $(d_{ij})_{ref}$, $(T_{ij})_{ref}$, and ω_{ij} are the VHS/VSS model parameters, n is the number density, T is the temperature and m is the molecular mass. The other method of determining the mean free path is by using the hard sphere (HS) collision model, resulting in the

	gas	m (kg)	d_{ref} (m)	T_{ref} (K)	ω	α
sec. 2.4.2	He	$6.65{\cdot}10^{-27}$	$2.28{\cdot}10^{-10}$	273	0.64	1.20
	Ar	$66.3{\cdot}10^{-27}$	$4.17{\cdot}10^{-10}$	273	0.85	1.60
	N_2	$46.5{\cdot}10^{-27}$	$4.18{\cdot}10^{-10}$	273	0.79	1.51
ref. [1]	He	$6.65{\cdot}10^{-27}$	$2.30{\cdot}10^{-10}$	273	0.66	1.26
	Ar	$66.3{\cdot}10^{-27}$	$4.11{\cdot}10^{-10}$	273	0.81	1.40
	N_2	$46.5{\cdot}10^{-27}$	$4.11{\cdot}10^{-10}$	273	0.74	1.36

Table 2.1: VSS parameters for helium, argon and nitrogen, determined by applying the equations in section 2.4.2. The parameters from reference [1] are also listed.

	gas-pair	m_r (kg)	d_{ref} (m)	T_{ref} (K)	ω	α
sec. 2.4.2	He-Ar	$6.04{\cdot}10^{-27}$	$3.22{\cdot}10^{-10}$	273	0.66	1.80
eqs. 2.34 & 2.35	He-N_2	$5.82{\cdot}10^{-27}$	$3.23{\cdot}10^{-10}$	273	0.66	1.60
	Ar-N_2	$27.3{\cdot}10^{-27}$	$4.17{\cdot}10^{-10}$	273	0.79	1.60
sec. 2.4.2	He-Ar	$6.04{\cdot}10^{-27}$	$3.22{\cdot}10^{-10}$	273	0.75	1.40
eqs. 2.36 & 2.37	He-N_2	$5.82{\cdot}10^{-27}$	$3.23{\cdot}10^{-10}$	273	0.71	1.35
	Ar-N_2	$27.3{\cdot}10^{-27}$	$4.17{\cdot}10^{-10}$	273	0.82	1.56
ref. [1]	He-Ar	$6.04{\cdot}10^{-27}$	$3.21{\cdot}10^{-10}$	273	0.73	1.64
	He-N_2	$5.82{\cdot}10^{-27}$	$3.21{\cdot}10^{-10}$	273	0.69	1.50
	Ar-N_2	$27.3{\cdot}10^{-27}$	$4.11{\cdot}10^{-10}$	273		1.33

Table 2.2: VSS parameters for collisions between different species molecules for helium, argon and nitrogen, determined by applying equations 2.34 and 2.35 or 2.36 and 2.37 in section 2.4.2. The parameters from reference [1] are also listed (a value for ω is not listed for Ar-N_2 pairs).

following equation:

$$\frac{1}{\lambda_{HS,i}} = \sum_{j=1}^{s} \left[\pi d_{ij}^2 n_j \left(1 + \frac{m_i}{m_j} \right)^{1/2} \right] \tag{2.39}$$

The HS model does not have a reference diameter that varies with temperature, and this model is only accurate at the temperature for which d_{ij} was determined. At this temperature, the values of λ_{HS} and λ_{VHS} differ and their ratio can be written as [20]:

$$\frac{\lambda_{VHS}}{\lambda_{HS}} = \frac{(7-2\omega)(5-2\omega)}{24} \tag{2.40}$$

The overall mean free path $\bar{\lambda}$ is determined (for both methods) as:

$$\bar{\lambda} = \sum_{i=1}^{s} \frac{n_i}{n} \lambda_i \tag{2.41}$$

2.5 Sampling

Due to the relatively (compared to the number of molecules in a physical system) low number of computational particles, computational results suffer from severe statistical noise and must be determined by sampling the molecular properties during many time steps (for a steady problem) or many ensembles (for an unsteady problem).

In the following sections, the most common case of a steady problem will be addressed. Ensemble averaging will be described in the section 2.5.3. In a steady problem, the flow properties do not change once the final solution has been reached (from some initial condition). Steady state sampling can be applied as soon as this steady state is expected to have been reached. Unfortunately, the user has to estimate the time needed to obtain steady state beforehand.

Flow field data and surface interaction data are obtained differently, as will be described in the next sections.

2.5.1 Flow sampling

Sampling of the flow is performed in a separate step inside the time step loop as shown in the DSMC flowchart in figure 2.1. The flow domain is divided into cells for the collision routines, and these cells are also used for the sampling. All properties of all particles within one cell (at the sampling time) are included in the accumulated sampling data of that cell. In each cell, the following particle properties are accumulated separately for all species:

- the number of particles,
- their velocity,

- the square of their velocity,
- their rotational energy, and
- their vibrational level.

All relevant flow data can be calculated from these data, as will be shown in section 2.6. Because the sampling data are accumulated on a per species basis, these flow properties can be calculated separately for all species, as well as for all species combined.

Note that it is not useful to sample the flow every DSMC time step, because two consecutive samples are usually highly correlated. For most simulations, sampling once every 4 time steps is sufficient.

2.5.2 Surface sampling

Sampling of surface properties is not performed as a separate step, but during the movement step, see figure 2.1. Every time (starting from the time at which steady state is expected to be reached) a computational particle interacts with a boundary (either a surface or an inlet/outlet), its incident and (if applicable) reflected properties are sampled. The following data is accumulated (separately for incident and reflected properties) for each predefined surface section:

- the number of particles,
- their velocity,
- the square of their velocity,
- their rotational energy, and
- their vibrational level.

These data allow calculation of e.g. incoming and outgoing:

- fluxes,
- normal and tangential momentum exchange, and
- total, translational, rotational and vibrational energy exchange.

Again, these data are accumulated on a per species basis, and can thus be calculated for each species separately, or for all species combined. Note that particles, which are entered through an inlet/outlet are also counted in the surface sampling routines.

2.5.3 Unsteady flows

For unsteady flows, sampling during many time steps is not possible. In this case, many ensembles have to be calculated, and the flow properties must be derived by averaging all samples of a specific time over all ensembles. In principle, the same data is sampled, and the same properties can be calculated from them. Note that calculating many ensembles for many time steps can be time and memory consuming due to the large number of ensembles which are needed and the necessity of storing sample data also as a function of time.

2.6 Sample averaging

At the end of a calculation, the flow properties such as the mass-average velocity $\vec{v}_{ma}$, the total, translational, rotational, and vibrational temperatures T, T_{trans}, T_{rot} and T_{vib}, and the number density n can be easily calculated.

Available sampling data (for species i in a particular computational cell) are the number sum $\sum N_i$, the velocity sum $\sum \vec{v}_i$, the sum of the velocity squared $\sum(\vec{v}\cdot\vec{v})_i$, the sum of rotational energy $\sum \epsilon_{r,i}$ and the sum of the vibrational level $\sum i_{v,i}$. Additional required data include the molecular mass m_i, the number of rotational degrees of freedom ζ_i and the characteristic vibrational temperature Θ_i.

For a simulation with k species and s samples, and a cell with volume V, the following equations can be used. The total number density is calculated as:

$$n = F_{num} \sum_{i=1}^{k} \left(\frac{\sum N_i}{sV} \right) \tag{2.42}$$

The equation for the mass-average velocity is:

$$\vec{v}_{ma} = \frac{\sum_{i=1}^{k} (m_i \sum \vec{v}_i)}{\sum_{i=1}^{k} (m_i \sum N_i)} \tag{2.43}$$

The translational temperature is determined as:

$$T_{trans} = \frac{\sum_{i=1}^{k} (m_i [\sum(\vec{v}\cdot\vec{v})_i - \vec{v}_{ma}\cdot\vec{v}_{ma} \sum N_i])}{3k_B \sum_{i=1}^{k} (\sum N_i)} \tag{2.44}$$

The rotational temperature is calculated as:

$$T_{rot} = \frac{2\sum_{i=1}^{k} (\sum \epsilon_{r,i})}{k_B \sum_{i=1}^{k} (\zeta_i \sum N_i)} \tag{2.45}$$

For the determination of the overall vibrational temperature, first the vibrational temperature $T_{vib,i}$ and the effective degrees of freedom $\zeta_{vib,i}$ for species i must be calculated:

$$T_{vib,i} = \frac{\Theta_i}{ln\left(1 + \frac{\sum N_i}{\sum i_{v,i}}\right)} \tag{2.46}$$

$$\zeta_{vib,i} = \frac{2\frac{\Theta_i}{T_{vib,i}}}{\exp\left(\frac{\Theta_i}{T_{vib,i}}\right) - 1} \tag{2.47}$$

The above equation calculates the effective number of degrees of freedom. This number differs from the theoretical value of 2 for any finite temperature. The reason for this difference is the use of a discretized quantum model for vibrational modes. The overall vibrational temperature can now be determined:

$$T_{vib} = \frac{\sum_{i=1}^{k}(\zeta_{vib,i} T_{vib,i} \sum N_i)}{\sum_{i=1}^{k}(\zeta_{vib,i} \sum N_i)} \tag{2.48}$$

Using the calculated values of the overall translational, rotational and vibrational temperature, the overall total temperature can be calculated as an average over all degrees of freedom:

$$T_{tot} = \frac{3T_{trans} + \frac{\sum_{i=1}^{k}(\zeta_i \sum N_i)}{\sum_{i=1}^{k}(\sum N_i)} T_{rot} + \frac{\sum_{i=1}^{k}(\zeta_{vib,i} \sum N_i)}{\sum_{i=1}^{k}(\sum N_i)} T_{vib}}{3 + \frac{\sum_{i=1}^{k}(\zeta_i \sum N_i)}{\sum_{i=1}^{k}(\sum N_i)} + \frac{\sum_{i=1}^{k}(\zeta_{vib,i} \sum N_i)}{\sum_{i=1}^{k}(\sum N_i)}} \tag{2.49}$$

Naturally, also in a simulation with multiple species, single species data (e.g. the translational temperature of a certain species, or the species concentration) can also be determined using the equations written above.

The statistical scatter in the average flow properties reduces with increasing sample size s. Hadjiconstantinou et al. [21] have shown that the relative statistical error E_ϕ in the calculated variable ϕ with a true average of $\bar{\phi}$ scales as:

$$E_\phi = \frac{\phi - \bar{\phi}}{\bar{\phi}} \propto \frac{1}{\sqrt{s\bar{N}}} \tag{2.50}$$

Here, $\bar{N}$ is the average number of particles in a cell. For the velocity, an additional scaling rule was derived (with c the thermal velocity):

$$E_v \propto \frac{c}{\bar{v}} \tag{2.51}$$

As a consequence of this scaling, flows with an average velocity much lower than the thermal velocity of the molecules need many more samples to reduce the scatter in the velocity.

As for the surface interaction data, the sampled data (e.g. summed incident velocity) can be converted to useful data (e.g. incident momentum flux) using trivial mathematics. These equations will not be discussed here.

2.7 Errors

2.7.1 Sources of error in DSMC

A DSMC gas flow simulation differs from reality in that time and space (for intermolecular collisions) are discretized and that the number of computational particles is small compared to the number of molecules in the real system. Consequently, the main sources of error are:

- the finite time step,
- the finite cell size, and
- the relatively low number of computational particles per cell.

Note that a fourth error exists, as discussed in section 2.6. This error is due to the statistical sampling, but can be reduced (in principle) to any required level by accumulating enough samples. The errors listed above do not arise from statistics, but must be regarded as discretization errors of the DSMC method.

The time step should be small to be able to justify the assumption that the movement and collision phases of the calculation may be decoupled. If the time step is too large, an unacceptable error may be introduced in the calculations, but if it is too small, the calculations will not be very efficient. A good rule of thumb [1] is to set the time step Δt no larger than one tenth of the mean collision time t_{mct}:

$$\frac{\Delta t}{t_{mct}} < \frac{1}{10} \tag{2.52}$$

The cell size should be small in order to prevent transport of energy or momentum over long distances in an unrealistically short time. This could happen if two particles located at opposite sides of a large cell collide. In order to prevent this, the cell size Δx should, as a rule of thumb, be kept smaller than one third of the mean free path λ [1]:

$$\frac{\Delta x}{\lambda} < \frac{1}{3} \tag{2.53}$$

The number of particles per cell N should be sufficient to prevent unphysical 'correlated' collisions, e.g. repeated collisions between the same particles. Another reason to keep the number of particles at this level, is to be able to capture the high energy tails of the velocity, rotational and vibrational distributions. As these high energy states are unlikely to occur, a computation with too few particles may completely neglect the influence of these states on the results. Bird [1] gives a rule-of-thumb for the minimal value of N:

$$N > 15 - 20 \tag{2.54}$$

2.7.2 Error dependence on DSMC parameters

Several authors have studied the convergence behavior of the three main DSMC error sources: the time step Δt, the cell size Δx and the number of particles per cell N. Chen and Boyd [22] studied the influence of N on the error in the temperature calculation. They report a dependence on N of the order $O\left(\frac{1}{N}\right)$ and for a case with $N = 20$, an error of less than 2% is found for sufficiently small Δt and Δx.

Alexander et al. [23] investigated the influence of the cell size Δx on viscosity and thermal conductivity. They find a dependence of the order of $O(\Delta x^2)$ and an error of less than 1.5% (in the limit of $N \to \infty$ and $\Delta t \to 0$) in the case of $\Delta x = \frac{1}{3}\lambda$.

Garcia and Wagner [24] and Hadjiconstantinou [25] have published results for the time step dependence of errors in viscosity, thermal conductivity and diffusion. They both conclude that the errors scale as $O(\Delta t^2)$, and give an error of less than 0.1% (in the limit for $N \to \infty$ and $\Delta x \to 0$) in the transport properties for $\Delta t = 0.1 \cdot t_{mct}$.

Rader et al. [26] studied the heat flux at a surface and the thermal conductivity of a gas using DSMC simulations, and found that the dependence on the parameters is $O\left(\frac{1}{N}\right)$ for N, $O(\Delta t^2)$ for Δt, and $O(\Delta x^2)$ for Δx. Their results also show that, using the rules in equations 2.52-2.54, the error in the heat flux and thermal conductivity is less than 2%.

2.8 Gas phase chemistry

Under some circumstances, collisions between molecules may lead to a gas phase chemical reaction. For a binary collision with two participating molecules, three types of elementary reactions are possible:

- an exchange reaction $AB + C \to A + BC$,
- a recombination reaction $A + B \to AB$, and
- a dissociation reaction $AB \to A + B$.

In a DSMC calculation, these three elementary reactions are allowed to occur during the collision phase as shown in figure 2.1. The procedures for the three reaction types will be treated in the subsequent sections. These procedures are based on the so-called Total Collision Energy model [27].

2.8.1 Exchange reaction

An exchange reaction can be defined as

$$AB + C \to A + BC \tag{2.55}$$

In an equilibrium situation, the effect of an exchange reaction can be written as

$$\frac{dn_{AB}}{dt} = \frac{dn_C}{dt} = -\frac{dn_A}{dt} = -\frac{dn_{BC}}{dt} = -k \cdot n_{AB} \cdot n_C \tag{2.56}$$

The reaction rate k completely defines the reaction. It can be described by the Arrhenius equation with Arrhenius parameters Λ and η and activation energy E_a:

$$k = \Lambda T^{\eta} \exp\left[\frac{-E_a}{kT}\right] \tag{2.57}$$

In each collision between particles a and b for which equation 2.55 is defined, the reaction probability is calculated using these equations for the total collision energy E_c and the average effective internal number of degrees of freedom $\bar{\zeta}_{int}$:

$$E_c = \frac{1}{2} m_r c_r^2 + \sum_{p=a,b} \left(\epsilon_{r,p} + i_{v,p} k_B \Theta\right) \tag{2.58}$$

$$\bar{\zeta}_{int} = \frac{1}{2} \sum_{p=a,b} \left(\zeta_{r,p} + \zeta_{v,p}\right) \tag{2.59}$$

In the summation, rotational and vibrational quantities are summed, please note that k_B is the Boltzmann constant. If the specific species has no rotational and/or vibrational modes, the corresponding terms should be omitted from the summation. The number of vibrational degrees of freedom associated with the vibrational modes is 2, but the use of a discrete quantum model reduces the *effective* vibrational degrees of freedom $\zeta_{v,p}$ to

$$\zeta_{v,p} = \frac{\epsilon_v}{k_B T_v/2} = \frac{i k_B \Theta}{k_B T_v/2} = 2i \frac{\Theta}{T_v} \tag{2.60}$$

The ratio of the characteristic vibrational temperature Θ and the vibrational temperature T_v is given by

$$\frac{\Theta}{T_v} = ln\left(1 + \frac{1}{\bar{i}}\right) \tag{2.61}$$

with $\bar{i}$ the average vibrational level of all molecules of the same species as p in the cell. The reaction probability $P_{exchange}$ for a colliding pair to undergo a chemical reaction can now be calculated as:

$$P_{exchange} = \begin{cases} 0 & \text{if } E_c \leq E_a \\ C_1 \left(E_c - E_a\right)^{C_2} \left(1 - \frac{E_a}{E_c}\right)^{\bar{\zeta}_{int} + 3/2 - \omega_{ab}} & \text{if } E_c > E_a \end{cases} \tag{2.62}$$

with C_1 and C_2 defined as

$$C_1 = \frac{\epsilon \Lambda \sqrt{\pi}}{2\sigma_{ab,ref}} \cdot \frac{\Gamma(\bar{\zeta}_{int} + 5/2 - \omega_{ab})}{\Gamma(\bar{\zeta}_{int} + 3/2 + \eta)} \cdot \sqrt{\frac{m_r}{2k_B T_{ref}}} \cdot \frac{T_{ref}^{1-\omega_{ab}}}{k_B^{\eta - 1 + \omega_{ab}}} \tag{2.63}$$

and

$$C_2 = \eta - 1 + \omega_{ab} \tag{2.64}$$

In the equation for C_1, ϵ is a symmetry factor, which becomes unity if the two particles are of the same species, and two if the species differ.

The remaining energy after the reaction, which is E_c corrected for the reaction heat, is distributed over all energy modes using the Larsen-Borgnakke distribution function [14, 15], see equation 2.20. In this equation, E_t should then represent the total unassigned energy, and ζ_{trans} should be changed to include all unassigned degrees of freedom, excluding those which belong to the mode that is being filled.

2.8.2 Recombination reaction

A recombination reaction can be defined as

$$A + B(+T) \rightarrow AB(+T) \tag{2.65}$$

Here T is a third body molecule (of a random species) which is needed to take away the energy that is released in a recombination. The effect of the reaction can be written as:

$$\frac{dn_A}{dt} = \frac{dn_B}{dt} = -\frac{dn_{AB}}{dt} = -k \cdot n_A \cdot n_B \cdot n_T \tag{2.66}$$

As T is a random species, the value n_T is simply the local total number density n. The reaction rate k can again be approximated using equation 2.57.

In each collision between particles of two species for which equation 2.65 is defined, the reaction probability is calculated almost the same as in the case of an exchange reaction. The only difference is the inclusion of the local total number density n to account for the third body molecule:

$$P_{recomb} = \begin{cases} 0 & \text{if } E_c \leq E_a \\ nC_1 (E_c - E_a)^{C_2} \left(1 - \frac{E_a}{E_c}\right)^{\bar{\zeta}_{int}+3/2-\omega_{ab}} & \text{if } E_c > E_a \end{cases} \tag{2.67}$$

The remaining energy after the recombination (which must be corrected for the reaction heat) is also distributed according to the Larsen-Borgnakke method. In this redistribution, the recombination product is collided (using the usual procedures) with a third body molecule to take away the excess energy.

2.8.3 Dissociation reaction

A dissociation reaction can be defined as

$$AB(+T) \rightarrow A + B(+T) \tag{2.68}$$

Again, T is a third body molecule (of a random species) which is needed to supply the required dissociation energy E_d. For a dissociation reaction, the only required parameter is the dissociation energy, an Arrhenius type equation is not necessary.

During the DSMC calculation, a dissociation may occur during the assignment of a new vibrational level to a molecule. How frequent this reassignment occurs is dependent on the vibrational relaxation time. When a dissociation is defined, the rotational energy is added to E_t in equation 2.20, and a new vibrational energy $E_{int,new}$ is chosen. Dissociation occurs whenever this vibrational energy is larger than the dissociation (or activation) energy in a collision. The remaining energy after dissociation is again distributed according to the Larsen-Borgnakke distribution.

2.9 Radial weighting factors

In a uniform 2D axisymmetric flow, the number of particles at (or near) a certain radial position r is proportional to r. In a simulation with evenly spaced cells in the radial direction, this means that the number of particles in the cell at the axis is very small, and the number of particles in the cell furthest from the axis is very large. To obtain a decent statistical sample of the flow near the axis, an extremely large number of particles would have to be included in the computation at large r. To circumvent this problem, radial weighting factors can be introduced.

In a simulation with radial weighing factors, each particle has a weight W (i.e. a single computational particle represents W real molecules) depending on its radial position r and a reference radius r_{ref}:

$$W = \frac{r}{r_{ref}} F_{num} \tag{2.69}$$

A particle far away from the axis will represent more real molecules than a particle close to the axis. As a result, a particle moving away from the axis has some probability (depending on the old and new W) to be removed from the simulation, and a particle moving toward the axis has some probability to be duplicated. The net result of this approach is that the number of computational particles is distributed evenly over the cells in the 2D computational domain, i.e. every cell (with equal axial and radial dimensions) will have an equal number of computational particles.

Within one cell, particles can have different weights due to the finite dimension of a cell in the radial direction. As a result, the collision routines should be changed accordingly. Fortunately, is was found [1] that the use of unchanged collision routines (i.e. using equal weighting for all particles within a cell) has a negligible effect on the flow.

On top of the basic implementation described above, some enhancements can be made. To prevent occurrence of identical particles within one cell, a buffer can be used for duplicated particles. If a particle is duplicated, the newly created particle is stored in a buffer, and a random buffer particle is entered into the flow.

Another enhancement stems from the observation [1] that the statistical scatter in the near-axis region is highly increased due to the introduction of weighting. To reduce this scatter, the weight of each particle is calculated as

$$W = \begin{cases} F_{num} & \text{if } r \leq r_{ref}, \\ \frac{r}{r_{ref}} F_{num} & \text{if } r > r_{ref} \end{cases} \tag{2.70}$$

This change effectively turns off radial weighting in the near axis region, which improves the near axis scatter.

2.10 Species weighting factors

Species weighting [28, 29] can be very useful in simulations with trace species which are present in (very) small concentrations. In reacting gas flow systems, such as e.g. Chemical Vapor Deposition reactors, it is not uncommon to have 1% reactant in 99% inert carrier gas. A normal DSMC simulation would have to trace 99 carrier gas particles for each trace gas particle. This means that 99% of the calculation time is devoted to the carrier, while it is the trace gas that is of interest. To circumvent this inefficient solution method, different weighting factors can be used, e.g. every species will have its own value of the F_{num} parameter. To distinguish between simulations without species weighting factors, W will be used as the ratio between the number of real and computational particles. The symbol W_a will thus denote the value of F_{num} for species a. In a simulation with weighting, the collision frequency of species with unequal weights is changed, and the major species particle properties do not change in every collision.

The derivation of the changes to the theory in equation 2.13 starts with an alternative representation of this equation. The number of collision pairs for a collision of a species a particle with a species b particle in a case with $W_a = W_b = W$ is

$$\#\text{pairs}_{a,b} = \frac{1}{2} n_b \left(\frac{n_a V}{W} \right) \Delta t (\sigma_T c_r)_{max} \tag{2.71}$$

The quantity $P^*_{a,b}$ is the probability that the properties of a species a particle are changed in a collision with a species b particle ($P^*_{b,a}$ is defined similarly). For a simulation with $W_a = W_b$, these are defined as

$$P^*_{a,b} = P^*_{b,a} = 1 \tag{2.72}$$

Please note the difference between P in equation 2.14 (which is used to determine if a selected pair will collide, both in simulations with and without weighting) and P^*. If a collision occurs, the new velocities of both a and b are computed, but in simulations with weighting, $P^*_{a,b}$ is then used to determine if the velocity of particle a is actually changed to this new value or remains unchanged.

In a simulation with trace species a and major species b, the weighting factor $W_a < W_b$. As equation 2.71 can only be used for equal weighting factors, the same weighting factor W_b

is used for both species in the following expression for collisions of a particle of trace species a with a particle of major species b:

$$\#\text{pairs}_{a,b} = \frac{1}{2} n_b \left(\frac{n_a V}{W_b} \right) \Delta t (\sigma g)_{max} = \frac{1}{2} n_b \left(\frac{n_a V}{W_a} \frac{W_a}{W_b} \right) \Delta t (\sigma g)_{max} \tag{2.73}$$

This artificially multiplies the number density of species a by a factor W_a/W_b. To obtain the correct collision frequency for a species a molecule, the value of $P^*_{a,b}$ needs to be modified ($P^*_{b,a}$ remains unchanged):

$$P^*_{a,b} = \frac{W_b}{W_a} \tag{2.74}$$

This is incorrect because $W_b/W_a > 1$, and thus the probability exceeds unity. This can be corrected by multiplying $P^*_{a,b}$ and $P^*_{b,a}$ by a factor W_a/W_b, and the #pairs by the inverse of this factor such that the product of #pairs and P^* remains equal. The result is

$$\#\text{pairs}_{a,b} = \frac{W_b}{W_a} \frac{1}{2} n_b \left(\frac{n_a V}{W_a} \frac{W_a}{W_b} \right) \Delta t (\sigma g)_{max} = \frac{1}{2} n_b \frac{n_a V}{W_a} \Delta t (\sigma g)_{max} \tag{2.75}$$

$$P^*_{a,b} = \frac{W_a}{W_b} \frac{W_b}{W_a} = 1 \tag{2.76}$$

$$P^*_{b,a} = \frac{W_a}{W_b} \tag{2.77}$$

For collisions between a major species b molecule and a trace species a molecule, the same approach can be used:

$$\#\text{pairs}_{b,a} = \frac{1}{2} n_a \left(\frac{n_b V}{W_a} \right) \Delta t (\sigma g)_{max} = \frac{1}{2} n_a \left(\frac{n_b V}{W_b} \frac{W_b}{W_a} \right) \Delta t (\sigma g)_{max} \tag{2.78}$$

This artificially multiplies the number density of species b by a factor W_b/W_a, the value of $P^*_{b,a}$ is corrected for this ($P^*_{a,b}$ remains unchanged):

$$P^*_{a,b} = 1 \tag{2.79}$$

$$P^*_{b,a} = \frac{W_a}{W_b} \tag{2.80}$$

The procedure for collisions between equal weight particles (e.g. of the same species, or of species with equal weight) remain unchanged from equation 2.71.

Random walks

Bird [1, 30] warns against the use of weighting factors in general, including radial and species weighting factors, due to random walks in momentum and energy. These occur whenever momentum and energy are not conserved in every collision, but only on average, as is the case in the implementation of species weighting as described above. Boyd [29] has constructed a new species weighting scheme which does exactly conserve momentum and energy (not during each collision, but over a series of collisions). In a collision between a major and trace species molecule, the change to the momentum of the major species molecules is always applied, but the change is reduced by an appropriate factor that is determined by the ratio of the weighting factors. Energy cannot be conserved simultaneously, the total energy slowly decreases. In Boyd's scheme, the total energy decrease due to collisions is monitored and accounted for by adding the appropriate amount of energy to major-major collisions.

The DSMC calculations with species weighting in this thesis use the implementation as described above, without any scheme to avoid random walks. In closed systems, with a fixed total energy, this is not an acceptable situation. The situation is different for applications with momentum and energy exchange to the surroundings (e.g. through a diffusely reflecting wall, an inlet or an outlet). In this case, the random walk in total system energy and momentum could be small compared to the fluctuations in these quantities due to the physical properties of the flow. This problem has been investigated by performing simulations of an 'open' geometry, both with and without species weighting factors. The results of this investigation can be found in section 4.9.

3. DSMC code development

This chapter describes the general structure and implementation choices of the DSMC codes developed in this thesis project. Two different codes are described: the 2D pure DSMC STARS code (section 3.1) and a general purpose 3D code called X-Stream with both continuum and DSMC capabilities (section 3.2). The 2D code was used to develop, debug and test the routines that are required for a functional DSMC code. This code was also used for performing research on simple geometries, as will be shown in following chapters. The 3D code was one of the main goals of the PhD project, and this code was constructed by relying on the tested routines of the 2D code. The 3D code is primarily applied to problems with complicated geometries.

3.1 2-Dimensional DSMC code

The STARS 2D DSMC code was developed in-house at the Delft University of Technology by the author. The acronym STARS stands for "Steady Two-dimensional or Axi-symmetric Rarefied flow Simulations". It is based on the description of DSMC as can be found in chapter 2. The code has the following properties and features:

- 2D plane and axisymmetric versions (within a single code)
- stream inlet and outlet, vacuum, diffuse and specular wall, symmetry plane, pressure inlet and outlet, and mass flow inlet boundary conditions.
- VHS [11] and VSS [12, 13] collision models with the Larsen-Borgnakke model [14, 15] for internal energy exchange
- chemical reactions of the exchange, recombination and dissociation type
- radial and species weighting factors
- flow field and surface interaction data output in Tecplot [31] format
- multi block Cartesian grids with variable grid cell size according to geometric progression

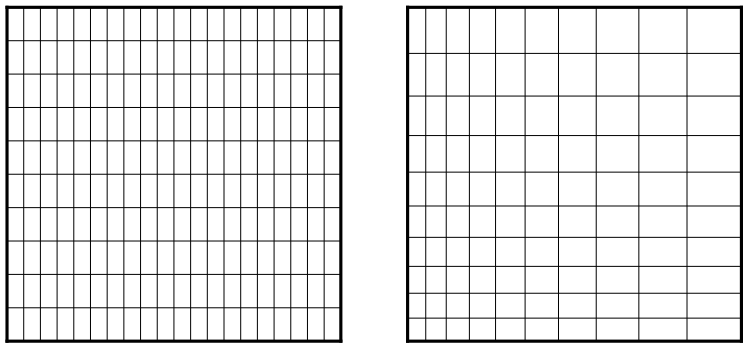

Figure 3.1: An example of uniform (left) and geometrically progressing (right) 2D Cartesian grid.

- fully parallelized by means of MPI [32]
- case file input
- restart file
- programming language Fortran 90

The features that are an integral part of the DSMC method have already been discussed in the previous chapter. The code specific features will be discussed below.

3.1.1 Multi block Cartesian grid

In DSMC, a grid is required for calculating the particle collisions and obtaining samples of the flow. In principle, these two DSMC steps can use different grids, but in STARS, the collision and sampling grids are identical. The grid in a computational block is a simple Cartesian, rectangular grid, with the possibility of including geometrically progressing cell sizes, as shown in figure 3.1. The computational advantage of this type of grid is the ease by which a molecule at a certain position can be linked to the cell in which it is located. For a uniform grid (with cells of uniform dimensions), this calculation is straightforward. For progressing grids, the analytical expression for the cell # (in the x-direction) as a function of the position x is:

$$\text{cell \#} = 1 + \lfloor \frac{\ln\left[1 - (1-r)\frac{x-x_{min}}{a}\right]}{\ln(r)} \rfloor \tag{3.1}$$

In this equation, a is the size of the first cell, which starts at x_{min} and $\lfloor . \rfloor$ denotes truncation to a lower integer. The parameter r is the progression parameter, the first cell has size a, the second $a \cdot r$, the third $a \cdot r^2$, etc.

Unfortunately, not all 2D plane or axisymmetrical geometries can be represented by a simple rectangular block. To be able to compute more complicated geometries, a multi-block approach can be adopted. In this approach, the domain is divided into two or more rectangular blocks. In each block, an independent (i.e. the grid nodes at the block boundary do not need to coincide) rectangular grid as described above can be used, with or without progression. Particles crossing the boundary between two blocks are simply transferred between blocks and the corresponding grids. The cell in which the particle is located in the new block can be easily determined based on the particle location.

3.1.2 Parallel computations

To increase calculation speeds of DSMC computations, parallelization has been implemented in STARS using MPICH [32]. Advantage is taken of the multi-block approach explained above. Each block is calculated on a separate processor, and particles that move between blocks (e.g. from block A to block B) through a block interface boundary during a time step are stored in a temporary array on the processor that handles block A. Most likely, the same will happen in block B, and all particles that move from block B to block A are also stored in a temporary array (on processor B). Note that the remaining time for translation of each particle is also stored.

Once all the particles in all blocks have been moved, the temporary arrays are exchanged using the MPI protocol, and the particles in these arrays are introduced in the appropriate block. These newly added particles can now finish their required displacement in their new block. Note that the particles that are for instance introduced into block A from block B may leave again (e.g. back to block B, or to another block C) during the same time step, so the exchange of particles is an event that reoccurs until all particles have reached their final location for the current time step.

The temporary array is constructed using a Fortran 90 TYPE statement that contains all relevant information about the particle, e.g. remaining time step, location, velocity, species, rotational and vibrational energy. The transfer of data through MPI is also performed using a special MPI Type structure, which is created such that all particle data is transferred with one call to MPI routines.

Load balancing can be achieved by manually dividing the entire geometry in blocks with (almost) equivalent computational loads. This process is not automated, and therefore requires an estimate of the final solution before the simulation is started. For computations with a poor block distribution, the loads of different processors can be highly unbalanced.

3.1.3 Case file input and restart file

The STARS code has been made more user friendly by introducing a case file input method. The case file format is very similar to the format used by the 3D code, an example case file can be found in section 3.2.4. Every line of this text file contains a keyword representing one of the computation parameters, followed by the value of the parameter (e.g. "`F_NUM 1.0e10`"). The keywords are organized in groups and sub-groups, and an intelligent parser is used to import all parameters into the program.

During the calculation, a restart file is written regularly to be able to restart a calculation. This can be convenient when a computation is stopped (e.g. because of a hardware failure) or when it is discovered that the steady time as defined in the case file is too short, and should be made larger. After resetting the sampling parameters, the computation can now be continued without the need to redo the calculation.

3.1.4 Fortran 90

The Fortran 90 programming language was used for the development of the STARS code. This language has certain advantages above the well-known but old Fortran 77. The most notable new features of Fortran 90 that are used in the code are:

- Dynamic allocation of variables
- Type definitions
- Pointers

Dynamic allocation provides an easy method to use the same executable for different calculations, while the use of types and pointers speeds up the code significantly.

3.2 3-Dimensional X-Stream code

The 2D STARS code as described in the previous section, has been integrated in an existing 3D CFD code called X-Stream [33, 34, 35]. X-Stream has been developed at the Netherlands Organization for Applied Scientific Research TNO, from which it is commercially available. A tailored version for the simulation of glass furnaces is marketed as GTM-X and a tailored version for the CVD industry as CVD-X. The following sections describe X-Stream, the integration of DSMC in the CFD code, the method for dealing with a 3D grid, and the last section gives an example of an X-Stream case file.

3.2.1 General X-Stream description

X-Stream is a general purpose Computational Fluid Dynamics (CFD) code, developed and supported by TNO. The code is a multi-domain, multi-physics simulation tool with a structured, boundary fitted and multi-block grid.

The equations that are solved are the incompressible Navier-Stokes equations, the energy equation, and additional equations appropriate for the specific problem, e.g. turbulence, combustion, radiation or chemistry equations. A Finite Volume Method is used on a collocated grid [36].

The problem can be split into multiple domains, in which different physical processes take place, and thus different equations must be solved. An example of such a computation is the melting of glass by combustion. The molten glass can be described by laminar flow, while the combustion gas flow must be solved using turbulence, radiation and combustion models. X-Stream handles the transition between these domains automatically.

Each domain can be split into multiple blocks so that any geometry can be modeled. A boundary fitted, structured grid is created separately for each block in such a way that the grids on both sides of a block or domain interfaces are connected at the interface, i.e. the vertices of the grids coincide at the interface.

Grids can be created in a graphical program called X-GUI [37], a version of FEMGV 7 [38] adapted for use with X-Stream. The same program is also used as a post-processor to view simulation results. For clarity, the pre- and post-processor modes of X-GUI are called Pre-Stream and Post-Stream, respectively. When starting a new calculation, a geometry and grid are created using Pre-Stream, which writes a case and grid file. After entering additional information in the case file, X-Stream performs the calculation based on the data in these files. At the end of the calculation, a datafile in Post-Stream format is generated, which can then be visualized using Post-Stream.

Additional features of the code include monitor points, p-modifiers, automatic grid refinement and parallelization. Several monitor points can be defined in the case file, and during the calculation, the value of e.g. flow variables at these points is printed to a file, so that the value can be monitored during the computation.

P-modifiers allow a portion of the grid to be excluded from the calculations. A p-modifier is defined as a volume in Pre-Stream, which lies in one or more blocks. The grid is generated as usual, but the cells in the p-modifier volume are marked. During the CFD calculation, these cells will be treated as a solid, where no flow is calculated. Note that using p-modifiers results in staircase like volumes, the grid is not fitted around the p-modifier.

X-Stream can perform automatic grid refinement for a block without the need to re-mesh the geometry in Pre-Stream. Each cell (in the block where the grid is being refined) is simply split into 8 new cells, placing new vertices exactly in between old vertices. This refinement can be specified per block.

X-Stream is a parallel code, it can divide the calculation over several processors if required. This division is done per block, i.e. each block is always calculated in a single process, but one process can contain more than one block. X-Stream automatically divides blocks over the available processes, such that a computation with N blocks can be performed on any number of processors between 1 and N.

3.2.2 Integrating DSMC in X-Stream

Starting point for the integration of DSMC in the existing X-Stream code was the 2D STARS code that was developed in the earlier phase of the project and that was described in section 3.1. Integration in X-Stream required the extension to 3D, and various other adjustments. The most notable change is the determination of the cell in which a computational particle is located. In rectangular grids, this is an easy task, but for boundary fitted grids, this is much more complicated.

Apart from this change, which will be discussed extensively in section 3.2.3, some other changes had to be made. First of all, the keywords required for DSMC were included in the general X-Stream case file. The code was also changed to handle existing X-Stream variable formats, e.g. for grid data and results data, and to comply with existing structures for parallelization and restart files.

The final result of the integration is a single program which can be used for both CFD and DSMC calculations. Both types of calculations use the same grid data format, the same case file format (although the contents of the case file will vary), and the same pre- and post-processor. This close interaction between CFD and DSMC will be extended (in the future) to include hybrid simulations, with CFD in one domain and DSMC in the other.

Many of the features of X-Stream were ported to DSMC simulations, including monitor points, p-modifiers and the parallelization features.

3.2.3 Locating particles in a 3D boundary fitted grid

In the boundary fitted grid which is used in X-Stream, no direct relation exists between the x, y, z coordinates of a point and the cell in which the point is located. For DSMC however, it is of vital importance that it is known in which cell a particle is located at the end of each movement step. This information is obtained by tracing the path of a particle during a time step from its initial cell, through all subsequent cells to the destination cell, or more accurately, from the initial sub cell to the destination sub cell. The reason for using sub cells, apart from decreasing the average collision distance as described in section 2.4, is to reduce the difficulties associated with particle tracing.

For this tracing, each hexahedral cell is decomposed into 2 halves, and then into 6 tetrahedral cells (tets) [39] as shown in figure 3.2. The i, j, k coordinates denote the ordering number of a cell in the structured block. The sub cell arrangement is identical for all cells, and the sub cells are number from 1 to 6.

At the beginning of a time step, the location *and* the cell i, j, k coordinates *and* the sub cell number of the particle is known. The sub cell is defined using the x, y, z coordinates of the 4 points or vertices, where x_1 is the x coordinate of the first vertex, etc. Using equation 2.5, the new location $\vec{x}_{new}$ of the particle is determined using the old location $\vec{x}_{old}$ and the particle velocity $\vec{v}$. If the rules-of-thumb for a good DSMC calculation (see section 2.7) are obeyed, a significant fraction of all particles will remain in the same cell. Therefore, the following

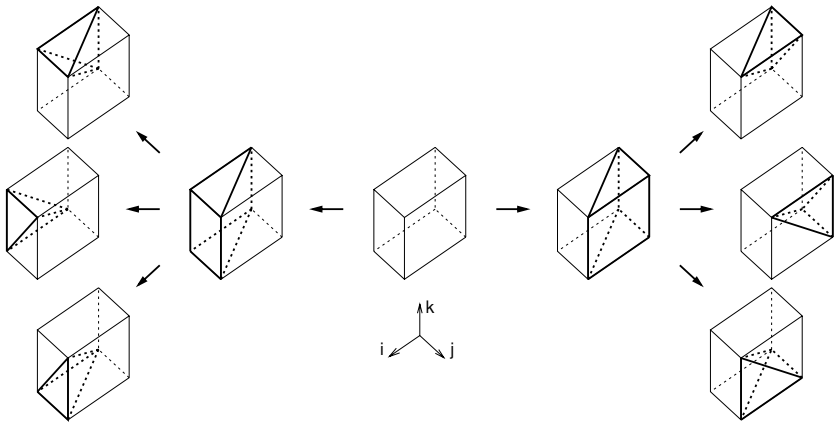

Figure 3.2: Decomposition of a hexahedral cell into 6 tetrahedra [39].

equations are used to transform the particle x,y,z location to ξ,η,ζ coordinates which are relative to the original cell [40] (see figure 3.3):

$$\begin{pmatrix}\xi\\ \eta\\ \zeta\end{pmatrix} = \frac{1}{6V}\begin{bmatrix}a_{11} & a_{12} & a_{13}\\ a_{21} & a_{22} & a_{23}\\ a_{31} & a_{32} & a_{33}\end{bmatrix}\begin{pmatrix}x_{new}-x_1\\ y_{new}-y_1\\ z_{new}-z_1\end{pmatrix} \tag{3.2}$$

Here, the coefficients a can be calculated as[1]:

$$\begin{aligned}
a_{11} &= (z_4-z_1)(y_3-y_1)-(z_3-z_1)(y_4-y_1)\\
a_{21} &= (z_2-z_1)(y_4-y_1)-(z_4-z_1)(y_2-y_1)\\
a_{31} &= (z_3-z_1)(y_2-y_1)-(z_2-z_1)(y_3-y_1)\\
a_{12} &= (x_4-x_1)(z_3-z_1)-(x_3-x_1)(z_4-z_1)\\
a_{22} &= (x_2-x_1)(z_4-z_1)-(x_4-x_1)(z_2-z_1)\\
a_{32} &= (x_3-x_1)(z_2-z_1)-(x_2-x_1)(z_3-z_1)\\
a_{13} &= (y_4-y_1)(x_3-x_1)-(y_3-y_1)(x_4-x_1)\\
a_{23} &= (y_2-y_1)(x_4-x_1)-(y_4-y_1)(x_2-x_1)\\
a_{33} &= (y_3-y_1)(x_2-x_1)-(y_2-y_1)(x_3-x_1)
\end{aligned} \tag{3.3}$$

The equation for the tet volume V is:

$$6V = (x_2-x_1)a_{11} + (x_3-x_1)a_{21} + (x_4-x_1)a_{31} \tag{3.4}$$

[1]The article of Kenwright and Lane [40] seems to contain a misprint in the definitions of matrix coefficients a. The error can be seen easily by observing that all coordinates should be relative to those of point 1.

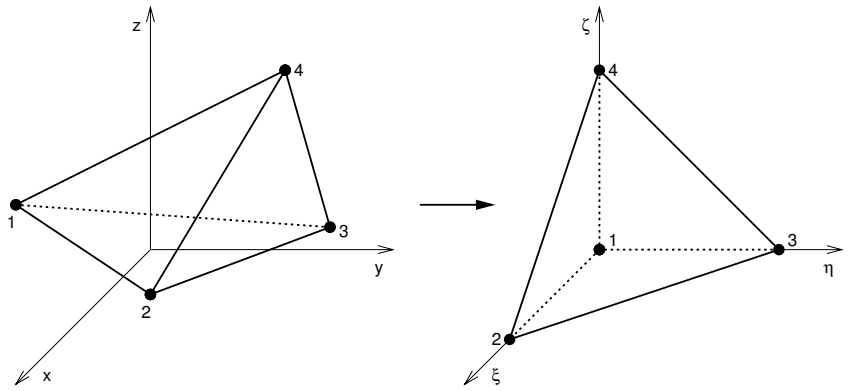

Figure 3.3: Conversion [40] from natural x, y, z coordinates (left) to ξ, η, ζ coordinates relative to the tet (right). Note that the ξ, η, ζ coordinates of vertices 1, 2, 3 and 4 are (0,0,0), (1,0,0), (0,1,0) and (0,0,1), respectively.

Note that the coefficients a and the tet volume V do not depend on the location of the particle. Therefore, they only have to be calculated once at the beginning of the simulation. The particle is located inside the sub cell if

$$\begin{aligned} \xi &\geq 0 \\ \eta &\geq 0 \\ \zeta &\geq 0, \text{ and} \\ \xi + \eta + \zeta &\leq 1 \end{aligned} \tag{3.5}$$

Each of the four conditions in the above equation represents the crossing of one of the four faces of the tet. If one or more of these conditions is violated, the new particle location is outside the initial sub cell. If only one condition is violated, the face through which the particle left the cell is known:

$$\begin{aligned} &\text{if} \quad \xi < 0 \quad \text{the exit face vertices are 1, 3 and 4} \\ &\text{if} \quad \eta < 0 \quad \text{the exit face vertices are 1, 2 and 4} \\ &\text{if} \quad \zeta < 0 \quad \text{the exit face vertices are 1, 2 and 3} \\ &\text{if } \xi + \eta + \zeta > 1 \text{ the exit face vertices are 2,3 and 4} \end{aligned} \tag{3.6}$$

If more than one condition is violated, the intersection point for each of the faces belonging to these violations must be calculated. This intersection point is calculated in terms of coordinates α,β relative to the face, see figure 3.4. Using the face with vertices 1, 2 and 3 as an

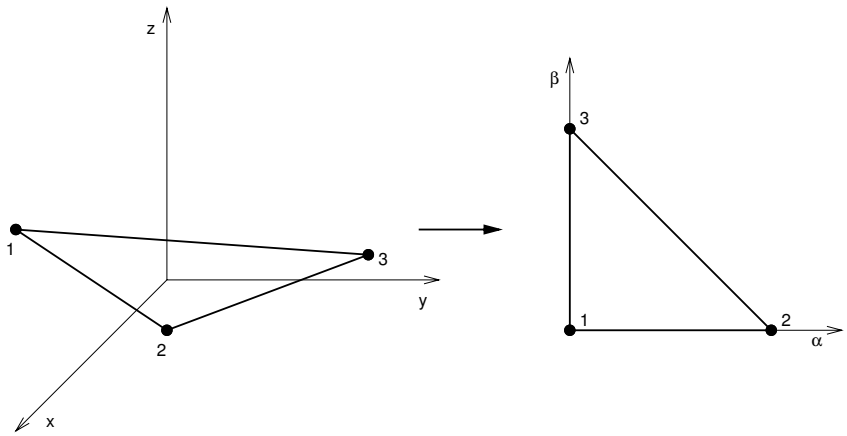

Figure 3.4: Conversion [41] from natural x, y, z coordinates (left) to α,β coordinates relative to the face (right). Note that the α,β coordinates of vertices 1, 2, and 3 are (0,0), (1,0), and (0,1), respectively.

example, the intersection point is calculated as [41]:

$$\alpha = \frac{[(\vec{x}_3 - \vec{x}_1) \times \vec{v}] \cdot [\vec{x}_{old} - \vec{x}_1]}{[(\vec{x}_3 - \vec{x}_1) \times \vec{v}] \cdot [\vec{x}_2 - \vec{x}_1]} \tag{3.7}$$

and

$$\beta = \frac{[(\vec{x}_2 - \vec{x}_1) \times \vec{v}] \cdot [\vec{x}_{old} - \vec{x}_1]}{[(\vec{x}_2 - \vec{x}_1) \times \vec{v}] \cdot [\vec{x}_3 - \vec{x}_1]} \tag{3.8}$$

The particle path intersects with the face if

$$\begin{aligned} \alpha &\geq 0 \\ \beta &\geq 0, \text{ and} \\ \alpha + \beta &\leq 1 \end{aligned} \tag{3.9}$$

For a tetrahedron as shown in figure 3.3, the above conditions can only be satisfied for one face, and this is the face through which the particle exits the tet. For a structured grid, the sub cell on the opposite side of the exit face is known, and the above procedure is repeated for new sub cells until equation 3.5 is satisfied. At that point the destination sub cell (at the end of the time step) of the particle is known.

Note that many particles remain inside their original sub cell during the displacement, and most of those that leave the sub cell will only violate one of the conditions of equation

3.5. As a result, equations 3.7 and 3.8 only have to be evaluated for a small fraction of the particles. Also, a majority of the particles that leave their original sub cell will only pass one face and end up in a neighboring sub cell.

3.2.4 Example case file

All computational parameters for a calculation in X-Stream have to be written in a case file. To give an impression of such a file, a (simplified) case file for a DSMC calculation in X-Stream is given below. The grid information is stored in a separate grid file, which is automatically created by the pre-processor. The descriptions on the right of the solid line are only included for clarification, these comments are not part of the case file.

```
BEGIN NAMES                                  | each keyword group
  CASE_NAME              casename              | is surrounded by a
  OUTPUT_FILENAME        casename.out          | BEGIN and an END
  GRID_FILENAME          casename.grd          | statement
END NAMES                                    |
                                             |
BEGIN DOMAIN domain1                         | a domain is a group of blocks
  BEGIN APPLY_MODEL                          | sub groups are also used
    APPLY_DSMC           TRUE                | switch between DSMC/CFD
  END APPLY_MODEL                            |
  BEGIN INITIAL_VALUE                        |
    U_VELOCITY           100.                |
    V_VELOCITY           0.0                 | } x,y,z velocities in m/s
    W_VELOCITY           0.0                 |
    PRESSURE             0.01                | in Pa
    TEMPERATURE          500.                | in K
  END INITIAL_VALUE                          |
END DOMAIN                                   |
                                             |
BEGIN MONITOR                                |
  MONITOR_FILENAME               casename.mon|
  CHECK_MONITOR_AFTER_TIMESTEP   100         | output every 100 time steps
  BEGIN DEFINE_MONITOR mon1                  |
    POINT                        0.05 0.01 0.0 | x,y,z coordinates of
                                             | monitor point in m
  END DEFINE_MONITOR                         |
  BEGIN MONITOR_OUTPUT                       |
    MY_MONITOR                   mon1 PRESSURE | variable to be monitored
  END MONITOR_OUTPUT                         |
END MONITOR                                  |
```

```
BEGIN DSMC
  F_NUM                 1.0e10
  STEADY_TIME           0.01                    in s
  SAMPLE_FREQUENCY      4                       # time steps between samples
  BEGIN DSMC_SPECIES N2
    MASS                                46.5e-27  molecular mass in kg
    REFERENCE_DIAMETER                  4.17e-10  in m
    REFERENCE_TEMPERATURE               273.      in K
    VISCOSITY_TEMPERATURE_EXPONENT      0.74      VHS/VSS ω parameter
    VSS_PARAMETER                       1.        VSS α parameter
    ROTATIONAL_DF                       2.0       rotational degrees of freedom
    ROTATIONAL_RELAX_TIME               5.        relaxation time in # collisions
    VIBRATIONAL_CHAR_TEMPERATURE        3371.     vibrational characteristic
                                                  temperature in K
    VIBRATIONAL_RELAX_TIME              5.        relaxation time in # collisions
  END DSMC_SPECIES
END DSMC

BEGIN TRANSIENT
  TIME_DEPENDENT_CASE   TRUE                    always true for DSMC
  TIME_STEP             1.0e-5                  in s
  TIME_STEPS            50000                   total # of time steps
END TRANSIENT

BEGIN BOUNDARY inlet1 INLET
  U_VELOCITY                    100.
  V_VELOCITY                    0.              } x,y,z velocities in m/s
  W_VELOCITY                    0.
  PRESSURE                      0.015           in Pa
  TEMPERATURE                   300.            in K
END BOUNDARY inlet1

BEGIN BOUNDARY outlet1 OUTLET
  U_VELOCITY                    120.
  V_VELOCITY                    0.              } x,y,z velocities in m/s
  W_VELOCITY                    0.
  PRESSURE                      0.008           in Pa
  TEMPERATURE                   550.            in K
END BOUNDARY outlet1
```

```
BEGIN BOUNDARY wall1 WALL
  U_VELOCITY                    0.
  V_VELOCITY                    0.
  W_VELOCITY                    0.
  TEMPERATURE                   600.
END BOUNDARY wall1
```

} stationary wall

in K

3.3 Code performance

In this section, the required calculation times as a function of the Knudsen number, as well as the parallel scalability of the STARS and X-Stream codes will be presented.

3.3.1 Calculation times

The time required for a DSMC calculation depends on the Knudsen number. This can easily be seen by inspecting the major DSMC steps as shown in figure 2.1. The main time consuming phases of the calculation are the movement, collision and sampling phases. *For a 2D calculation* obeying the rules for a good DSMC calculation as described in equations 2.52, 2.53 and 2.54, the dependency on Kn of each of the three phases can be described as follows.

The time t_{move} for the movement phase is proportional to the total number of computational particles, which is proportional to Kn^{-2}:

$$t_{move} \propto (\#\ \text{particles}) \propto \frac{1}{\mathrm{Kn}^2} \tag{3.10}$$

This equation ignores the influence of the computational boundaries, which are also relevant in the movement phase. In principle, an increased Kn leads to an increased time step, which leads to an increased probability that a particle collides with a surface. The exact relation of the time needed to calculate the surface interactions t_{surf} depends on the geometry, and can not be given as a general expression. For a simple rectangular domain, t_{surf} can be approximated as

$$t_{surf} \propto (\#\ \text{particles}) \cdot \Delta t \propto \frac{1}{\mathrm{Kn}^2} \cdot \mathrm{Kn} \propto \frac{1}{\mathrm{Kn}^1} \tag{3.11}$$

Generally, in flows with a very low Kn, the number of computational particles that interact with a boundary during a time step is very small compared to the total number of computational particles in the flow. In flows with a high Kn, this ratio is very high, approaching unity at a Knudsen number of about 10. At this Kn, each particle reaches (on average) one boundary in a single time step. For even higher Kn, the number of interactions with a boundary increases further as the average number of boundary interactions per particle per time step increases from unity to (in principle) infinity. The total time required for the movement phase ($t_{move} + t_{surf}$) in therefore proportional to Kn^{-2} at low Kn, and to Kn^{-1} at high Kn.

The time t_{coll} required for the collision phase can be derived from equation 2.9. In each cell, the number of collision pairs, and thus the required calculation time, can be described as:

$$(\#\text{ pairs}) \propto \frac{(\#\text{ particles per cell})^2 F_{num} \Delta t}{V_{cell}} \tag{3.12}$$

The number of particles in a cell is a constant (according to equation 2.54), F_{num} and Δt are linearly proportional to Kn and V is inversely proportional to the total number of cells, leading to $V \propto \mathrm{Kn}^2$. As a result, the number of collision pairs in each cell in a time step is independent of the Knudsen number. This leads to

$$t_{coll} \propto (\#\text{ cells}) \propto \frac{1}{\mathrm{Kn}^2} \tag{3.13}$$

The time t_{samp} needed for sampling is directly proportional to the number of computational particles, and is therefore proportional to Kn^{-2}:

$$t_{samp} \propto (\#\text{ particles}) \propto \frac{1}{\mathrm{Kn}^2} \tag{3.14}$$

By comparing the above equations, it is clear that most of the steps in a 2D DSMC calculation scale with Kn^{-2}. Only the interaction with surfaces shows a dependency (in a simple case) of Kn^{-1}. As discussed above, the surface interactions only become important at high Kn, where t_{move}, as well as t_{coll} and t_{samp} are much smaller than t_{surf}.

For a full 3D calculation, the above calculation times should be all be multiplied with a factor Kn^{-1}, leading to a scaling of the calculation time as Kn^{-3} at low Kn. Please note that the above scaling rules apply to the computation time *per time step*. When performing a numerical calculation over a fixed physical time, the number of time steps scales with Kn^{-1}, leading to a scaling of the total calculation time as Kn^{-3} (2D) or Kn^{-4} (3D) at low Kn.

The Knudsen scaling behavior of the STARS and X-Stream codes was studied using computations of argon gas in a simple rectangular 2D domain of size 1x2 m. The total number of particles and cells is listed in table 3.1. Note that, according to the rules in section 2.7, both the total #cells and the #particles scale with Kn^{-2}. As the X-Stream code is inherently 3D, only one cell was used in the third dimension for all cases, leading to a 2D dependency on Kn as described above. Two stream boundaries are located at the 1 m long boundaries and the 2 m long boundaries are diffusely reflecting surfaces. The gas and the walls are stationary and at a constant temperature, and the Knudsen number was varied by varying the number density. Each simulation was performed on a single AMD MP 1800+ processor with 1 GB of memory.

The results for the total calculation time per time step are depicted in figure 3.5. Both the STARS and X-Stream codes show a very similar behavior, the CPU time per time step being proportional to $\mathrm{Kn}^{-2.4}$ at low Kn. This is significantly different from the theoretical Kn^{-2} behavior (also shown in the figure). This is most likely due to the decreased efficiency of the code when working with large dynamically allocated arrays and other overhead issues

Kn	#cells	#particles
0.02	400 x 200	$2.0 \cdot 10^6$
0.05	160 x 80	$3.2 \cdot 10^5$
0.1	80 x 40	$8.0 \cdot 10^4$
0.2	40 x 20	$2.0 \cdot 10^4$
0.5	16 x 8	$3.2 \cdot 10^3$
1.0	8 x 4	$8.0 \cdot 10^2$
2.0	4 x 2	$2.0 \cdot 10^2$

Table 3.1: Listing of the number of cells (in the x and y direction) and number of particles for the determination of the Kn dependency of calculation time.

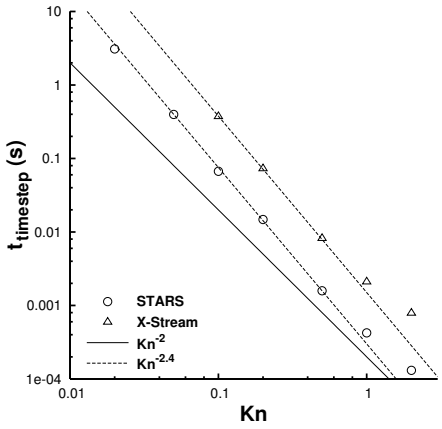

Figure 3.5: Scaling of the CPU time per time step as a function of the Knudsen number for the STARS and X-Stream codes for a 2D problem.

such as reading from and writing to files on disk. Starting at approximately Kn = 1, the slope clearly decreases. This can be attributed to the increased influence of t_{surf} as described above.

Figure 3.5 also shows that an X-Stream calculation takes 5 times longer than a comparable STARS simulation (at low Kn). Of course, the reason for this is the increase in calculation time associated with the full 3D particle tracing from cell to cell (see section 3.2.3). As a result, it is much more efficient to use the STARS code whenever possible, and to use X-Stream only for 3D flows.

Rough estimations can be made as to which problems (i.e. which Kn numbers) can still be calculated within a reasonable time limit (i.e. 10 days on 20 CPU's). For not to complicated 2D problems, a calculation with Kn as low as 0.03 should be possible within these limits. For 3D problems, this Kn limit is much higher, and lies at about 0.08. It must be noted that these are very rough estimates, and depend on the details of the problem.

3.3.2 Parallel scaling efficiency

The same test case problem as applied for the Kn dependency is used to study the parallel scaling efficiency. The problem was calculated on 1, 2, 4 and 8 processors for different values of the Kn number (Kn=0.02, 0.1, and 0.5, settings can be found in table 3.1). For the computations on more than one processor, the length of the computational domain in the x direction was split up into 2, 4 or 8 sections. For the X-Stream calculations, the number of cells in the third dimension is again set to unity to mimic a 2D behavior that can be compared to the STARS behavior. These calculations were performed on a Beowulf cluster operated under Linux, with cluster nodes that each contained two AMD MP 1800+ processors (running at 1533 MHz) and 1 GB of memory. The nodes are connected through standard 100 Mbit network interface cards. The 1, 2, 4, and 8 processor jobs were calculated on 1, 1, 2, and 4 cluster nodes, respectively.

The results for the parallel scaling efficiency of the STARS and X-Stream codes is shown in figure 3.6. The speedup in this figure is defined as the reduction of the total calculation time, compared to a calculation on one processor. The ideal speedup (indicated by the solid line) is also shown. The deviation from the ideal line is caused by the extra time needed for the communication between different processors.

Comparing the STARS results for different Knudsen numbers, it becomes clear that the speedup improves for reducing Kn. This is a very fortunate circumstance, as these low Kn calculations have the longest calculation times, as has been shown in the previous paragraph. If these low Kn cases are calculated in parallel, a significant reduction of computation time can be achieved.

For high Kn flows, parallelization results in an increased calculation time. Fortunately, these cases run relatively quickly, and parallelization is not of major importance.

Comparing the STARS and X-Stream speedup, it becomes clear that X-Stream achieves a better speedup at the same value of Kn. The reason for this is the fact that the X-Stream code, being fully 3D, requires longer calculation times for similar problems. In this case, the 3D

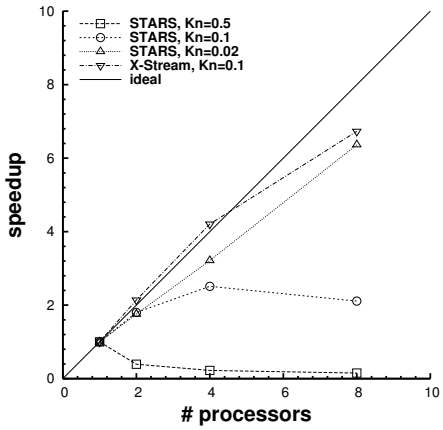

Figure 3.6: Parallel scaling properties of the STARS and X-Stream codes.

X-Stream calculation took approximately 5.5 times longer than the 2D STARS calculation (on 1 processor). The total calculation time is thus increased, while the total communication time (in these similar cases) remains the same. The relative time needed for the communications (compared to the total calculation time) therefore decreases, leading to a better parallel scalability.

4. Validation of the developed codes against data from literature

This chapter describes the validation of the STARS and X-Stream codes by using experimental, numerical and theoretical results from literature, as well as consistency tests of the chemistry and species weighting implementations.

4.1 Supersonic leading edge

In this section, a comparison will be made between results of the DSMC2 code by Bird [1] and our STARS code for a 2D nitrogen shock over a flat plate. This problem is referred to as the supersonic leading edge problem in reference [1]. The geometry for this case is shown in figure 4.1

The 2D domain is 1 m long and 0.6 m high, and contains 100x60 cells, each with 4 sub cells. Grid progression is used in both the x and y directions, with a ratio of the last and first cell sizes of 2 in both directions. The VHS collision model is used, using standard nitrogen parameters with a reference temperature of 273 K.

The boundary conditions on the left, top and right side of the picture are stream boundaries, with $n = 1.0 \cdot 10^{20}$ m^{-3}, $T = 300$ K, and $v_x = 1412.5$ m/s. The flat plate, which starts at a distance of 0.07145 m from the beginning of the computational domain, and extends to the end of the domain, is diffusely reflecting with a temperature of 500 K. The boundary upstream of the plate is a symmetry plane.

The time step is $4.0 \cdot 10^{-6}$ s, and a total of 200,000 time steps is calculated. Steady state is assumed to have been reached after $2.4 \cdot 10^{-3}$ s. Approximately 37,500 computational particles were used.

A comparison of the results of the DSMC2 and STARS codes can be seen in figure 4.2. Since all DSMC parameters, initial and boundary conditions are identical for both calculations, it is expected that the simulation results are identical. The figure clearly shows that the simulation results for the number density, the x velocity, the rotational temperature and the total temperature are almost indistinguishable, leading to the conclusion that the basic func-

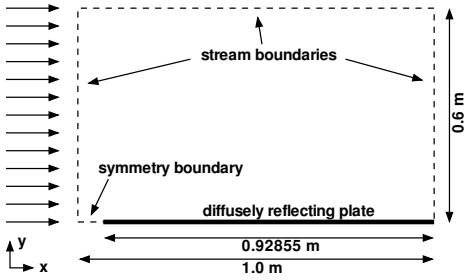

Figure 4.1: The geometry for the supersonic leading edge problem. The dashed rectangle denotes the computational domain, the solid line on the bottom represents the flat plate. The direction of the upstream flow is shown by the arrows.

tionality of the STARS DSMC implementation (moving particles, colliding, and sampling) is working as expected.

4.2 Flow between parallel disks

Gochberg [42] has previously compared DSMC simulations of radial flow between parallel disks to analytical continuum theory using Maxwell's slip coefficient and the Chapman-Cowling expression for viscosity. The geometry of this parallel disk configuration is shown in figure 4.3. The distance $2H$ between the plates is 8.7 mm, the inlet is located at a radial position of 26.1 mm and the outlet is at 87 mm. Helium is used as a test gas.

Based on analytical theory, Gochberg gives the following equation for the throughput Q (in Pa·m^3/s) through the gap between the disks:

$$Q = Q_{fm} \cdot \left[\frac{\pi}{32\mathrm{Kn}} + \frac{\pi}{4} \frac{2/\mathrm{Kn}}{1+2/\mathrm{Kn}} + \frac{1}{1+2/\mathrm{Kn}} \right] \tag{4.1}$$

with $\mathrm{Kn} = \lambda_{HS}/2H$ the Knudsen number, and Q_{fm} the throughput in the free molecular flow regime, which can be formulated as:

$$Q_{fm} = \frac{4}{3}\pi c H^2 \frac{p_1 - p_2}{\ln(r_1/r_2)} \tag{4.2}$$

In this equation, c is the average thermal velocity, p is the pressure and r is a radial position. Subscripts 1 and 2 denote different radial positions. Gochberg found an excellent agreement between experimental data, DSMC simulations and the analytical equations 4.1 and 4.2.

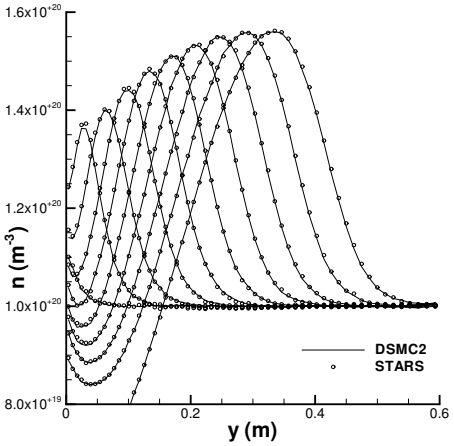

(a) Profiles of nitrogen number density n.

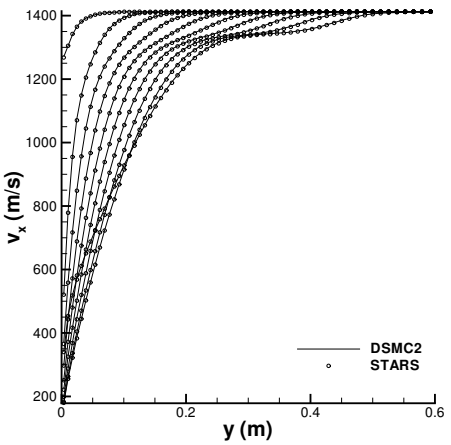

(b) Profiles of x velocity v_x.

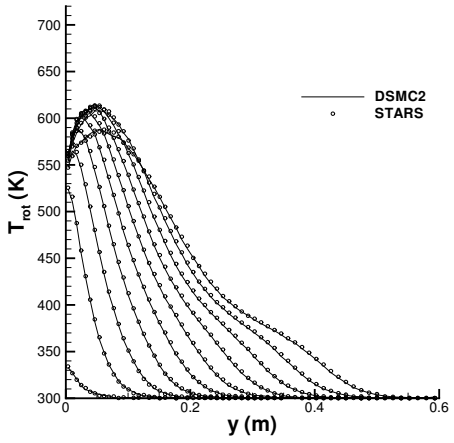

(c) Profiles of rotational temperature T_{rot}.

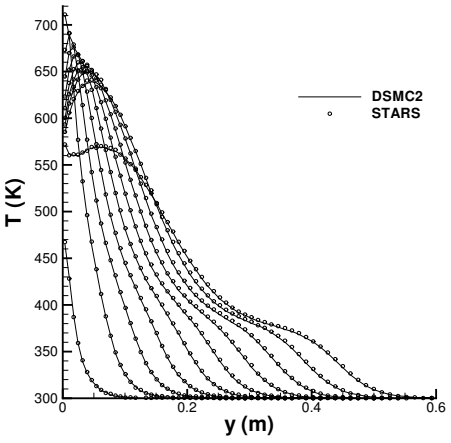

(d) Profiles of total temperature T.

Figure 4.2: A comparison of the results of Bird's DSMC2 code [1] and the STARS code for the supersonic leading edge. Shown are the DSMC2 (line) and STARS (symbols) profiles on lines perpendicular to the plate (i.e. with constant x) at 10 different x coordinates.

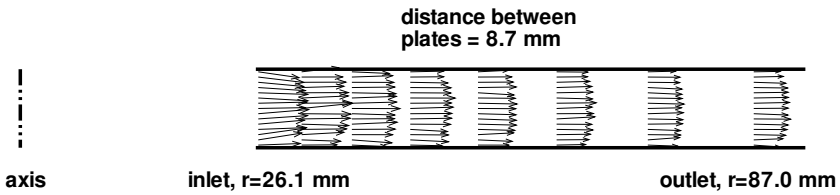

Figure 4.3: The geometry for the simulations on the radial flow between parallel disks. The inner and outer radii of the disks are used as boundaries for the computation. The arrows show velocity profiles from the simulation with Kn∼125.

For these equations, it is important to note that Gochberg uses the hard sphere definition of the mean free path λ. The STARS code calculates Kn in the VHS/VSS manner, and thus equation 2.40 must be applied to obtain a mean free path that can be used in equation 4.1. For the current problem using Helium as a gas, the value of ω is 0.66, and the ratio in equation 2.40 equals 0.87.

The relation between Q and the molecular flow rate $\frac{dN}{dt}$ can be written as:

$$Q = k_b T \frac{dN}{dt} \tag{4.3}$$

Following Gochberg, the results will be presented in the form of the dimensionless throughput B:

$$B = \frac{Q}{Q_{fm}} \tag{4.4}$$

A series of simulations was performed, with Kn varying from 0.064 to 125. In each simulation, the throughput was determined by monitoring the particle flow rates at the inlet and the outlet. In a steady state situation, the flow rates should be independent of the radial position, and this is confirmed by the fact that the data for the inlet and outlet are identical. The comparison of the results to the theory of equation 4.1 is shown in figure 4.4. As can be seen clearly, the agreement is very satisfactory. The simulation results accurately follow the trend of decreasing B for increasing Kn at low Kn, and constant B at high Kn. The position of the change from a varying B to a constant B is also reproduced accurately. A minimum in the throughput is found at Kn $\simeq$ 2, an effect that is also observed for flow through tubes and is known as the Knudsen minimum. It can thus be concluded that STARS performs very well in this validation case.

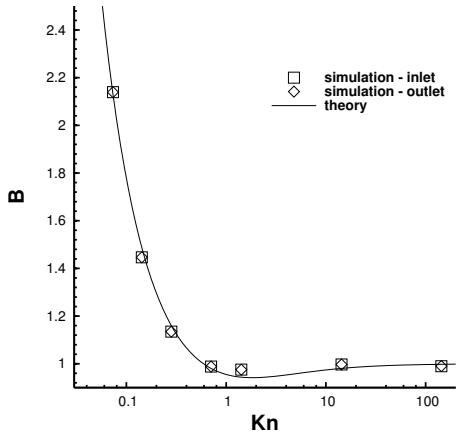

Figure 4.4: The dimensionless throughput B as a function of the Kn number for the flow between parallel disks. The squares represent the simulation throughputs at the inlet and the diamonds denote the throughputs at the outlet. The solid line is the theory of equation 4.1. Kn is defined using the hard sphere mean free path.

4.3 Flow trough a micro channel

Shih et al. [43] have experimentally studied the flow of helium and nitrogen through a micro channel with length $L = 4000\,\mu$m, width $w = 40\,\mu$m, and height $h = 1.2\,\mu$m. They also present an analytical theory for this flow, based on the Navier-Stokes equations and the Maxwell model for the velocity slip v_{wall} at the wall (assuming fully diffuse reflection):

$$v_{wall} = \lambda \left| \frac{du}{dy} \right|_{wall} \tag{4.5}$$

Using this model, the following equations can be derived for the mass flow rate $\dot{m}$ and the profile of the pressure p as a function of the position x along the channel:

$$\dot{m} = \frac{h^3 wm}{24 \cdot k_b T L \mu} p_o^2 \left[\left(\left[\frac{p_i}{p_o} \right]^2 - 1 \right) + 12 \mathrm{Kn}_o \left(\frac{p_i}{p_o} - 1 \right) \right] \tag{4.6}$$

$$\frac{p(x)}{p_o} = -C + \sqrt{C^2 + \left[1 - \frac{x}{L} \right] \left[\left(\frac{p_i}{p_o} \right)^2 + 2C \frac{p_i}{p_o} \right] + \frac{x}{L} [1 + 2C]} \tag{4.7}$$

with

$$C = 6 \cdot \mathrm{Kn}_o \tag{4.8}$$

In these equations, m is the molecular mass, T is the temperature (which is constant throughout the channel), μ is the continuum viscosity, p_i and p_o are the pressure at the inlet and outlet, respectively, and Kn_o is the Knudsen number at the outlet (with Kn based on the hard sphere definition of the mean free path and the channel height h). Shih et al. compared their experimental results to these equations, and found a good agreement for the pressure, and a very good agreement for the mass flow rate for Kn from 0.07 to 0.16. This makes the above equations ideal for validation of a DSMC code.

The validation calculation was carried out using the 2D STARS code, using a channel with a length L of 2000 μm and a total height of 1.2 μm, of which half was simulated. The 3D nature of the original experimental setup can be accurately reduced to this 2D geometry due to the high w/h ratio. The total length of the channel was shortened to reduce computation times. As a test gas, helium was used with VHS model parameters taken from Bird [1]. The VHS model was chosen because diffusion is not important and (again) reduction of the required computation time. The temperature of the entire system is 300 K and the pressures at the inlet and outlet were 159052 Pa and 99407 Pa, respectively, resulting in a Kn number varying from 0.092 to 0.15.

The mass flow rate in the simulation is $1.49{\cdot}10^{-12}$ kg/s (with $w = 40\ \mu$m), which is 0.6% lower than that predicted by equation 4.6. This comparison is in agreement with the findings of Shih et al. that the theory predicts the mass flow rate quite accurately. The predicted mass flow rate is 66% higher than the value predicted by equation 4.6 for $\mathrm{Kn}_o = 0$ (no-slip continuum flow). This clearly demonstrates the large deviations from continuum theory for this case.

The results of the simulated pressure profile are compared to the theory in figure 4.5. It is clear that the simulation profile slightly differs from the theoretical result. The results given by Shih et al. for the pressure profile (comparing the theory with experiments) show similar deviations, with the experimental pressure slightly below the theoretical predication for their 8.7 psig case, which corresponds to the pressure drop in our simulations. Xie et al. [44] also performed DSMC simulations on micro channels, and they also find a small difference between their simulated pressure profile and the experimental results by Shih et al. Their DSMC results show a slightly lower pressure in the middle of the channel, the same trend as is seen in figure 4.5. Given these other results, the deviation from the theoretical line for the pressure profile can most likely be attributed to some rarefaction effect that has a slight influence beyond the slip velocity. Together with the excellent prediction of the mass flow rate, it can be concluded that STARS performs very well in this validation case.

4.4 Plume impingement on a flat plate

Legge [45, 46] and Döring [47] have experimentally studied the impingement of a plume on a flat plate. Measured quantities are surface pressure, wall shear stress (both measured by Legge) and heat flux (measured by Döring). Both Legge and Döring used a setup resembling the geometry shown in figure 4.6. The jet nozzle has a radius R of 0.5 mm, and the distance

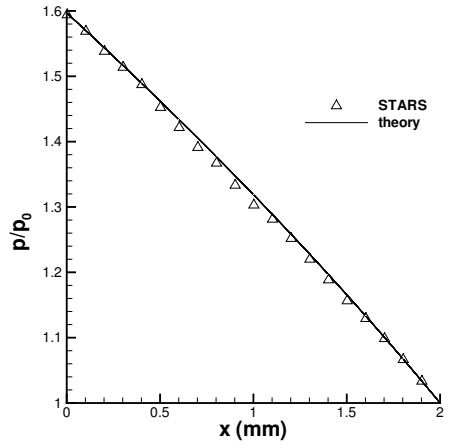

Figure 4.5: The pressure profile along the micro channel. Shown are the STARS simulation result and the theoretical line as predicted by equation 4.7.

L between the nozzle and the surface is 40 mm. The background pressure during the experiments was 0.045 Pa for Legge's experiment and 0.090 Pa for Döring's experiment. Nitrogen was used both in the jet and as a background gas.

The DSMC computations of these cases were performed using the STARS code, applying radial weighting factors. The axi-symmetric computational domain included the area between the nozzle and the surface (not including the nozzle internal flow) and extended $2.5L$ radially. For the simulation, the VSS properties for N_2 were taken from Bird [1]. The temperature of the surface and the (stagnant) background gas were taken to be 300 K, and following Liu et al. [48], the exit conditions at the nozzle were assumed sonic and taken as 300 K, 323 m/s and 532 Pa.

Both Liu et al. [48] and Hyakutake and Nishida [49] have performed DSMC simulations on Legge's experimental cases, and Liu et al. have also computed Döring's experimental results. The experimental data by Legge was taken from Hyakutake and Nishida's paper because their figures were of much better quality than Legge's original publication. The data produced by Döring was taken from the figures in the paper by Liu et al., because the original report is very difficult to find. The experimental and computational results are shown in figures 4.7, 4.8 and 4.9. Following Legge's papers, the pressure p and shear stress τ profiles are made dimensionless by using the nozzle reservoir pressure p_0 (which was 1000 Pa), the nozzle radius R and the distance L between the nozzle and the surface.

The simulated surface pressure profile in figure 4.7 is accurate for r/L larger than approximately 0.5, but overestimates the experimental results at smaller r. A similar trend is found

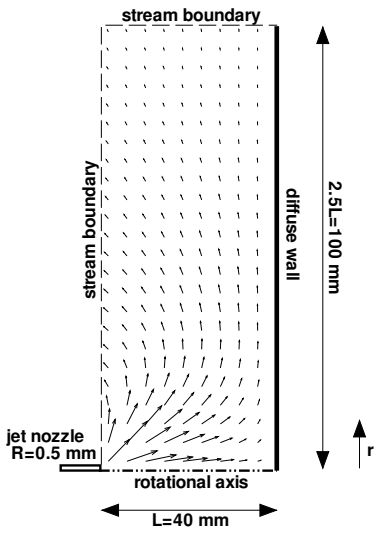

Figure 4.6: The geometry for the plume impingement on a flat plate. The arrows show a representative average flow field.

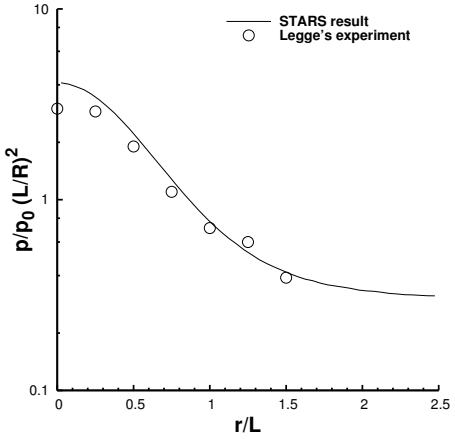

Figure 4.7: Surface pressure results for the case of plume impingement on a flat plate. Shown are the STARS simulation results (solid line) and the experimental results by Legge [45, 46] taken from the paper by Hyakutake and Nishida [49].

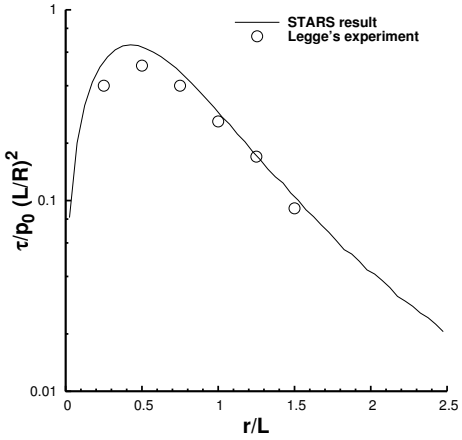

Figure 4.8: Shear stress results for the case of plume impingement on a flat plate. Shown are the STARS simulation results (solid line) and the experimental results by Legge [45, 46] taken from the paper by Hyakutake and Nishida [49].

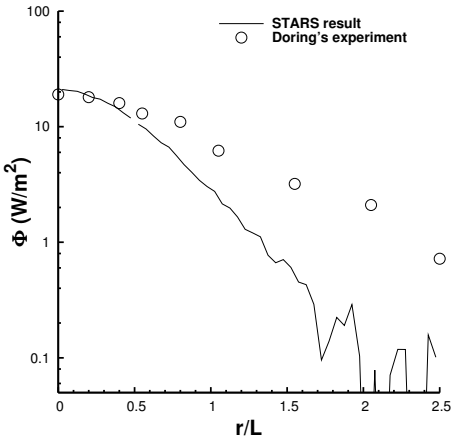

Figure 4.9: Heat flux results for the case of plume impingement on a flat plate. Shown are the STARS simulation results (solid line) and the experimental results by Döring [47] taken from the paper by Liu et al. [48].

in both Liu et al. and Hyakutake and Nishida (not shown), albeit that their computations produce an accurate estimate of the experimental data for small r, and underestimate the results for large r. The only known difference between the STARS simulations and those of Liu et al. and Hyakutake and Nishida is that both latter DSMC computations were performed using the VHS model, in contrast to the STARS computations which used the VSS model. An additional STARS calculation using the VHS model did not show a significant difference in the results, and the reason for the different DSMC results is therefore not known.

The simulated shear stress profile in figure 4.8 shows a similar trend as the surface pressure. At large r/L, the prediction is accurate, while at small r, there is a slight overestimation. This overestimation is also found in the results of Liu et al., while the results of Hyakutake and Nishida show a slight underestimation (both not shown). In any case, the results reproduce the experimental profile relatively well.

The most significant difference between the experiments and the simulations can be found in figure 4.9, where the simulated heat flux is compared to the experimental findings. It can be seen clearly that the STARS results decay much faster than the experimental results, a trend that is also reported by Liu et al. The heat flux at $r/L = 0$ is predicted correctly.

Taking into account all the results presented in this section, it is clear that STARS can reproduce the experimental results to a satisfactory degree for the surface pressure and the shear stress. For the heat flux to the surface at larger radii, the comparison is not good. The more or less identical DSMC results by Liu et al., however, seem to indicate that some physically relevant phenomena (e.g. radiation, which is not taken into account in the simulations)

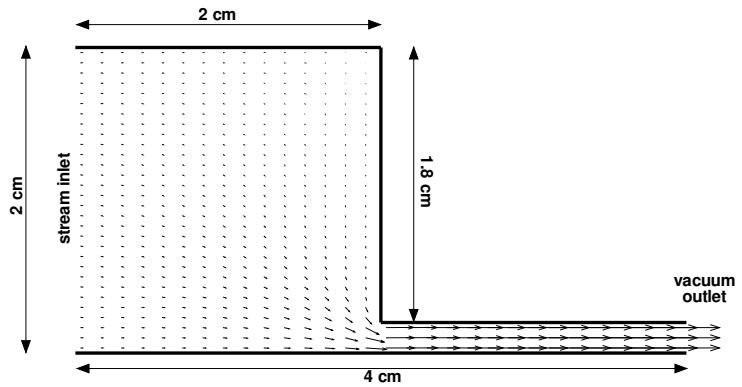

Figure 4.10: Geometry for calculation of the acceleration of a gas through a sudden contraction.

or experimental uncertainty (e.g. in the measured surface temperature) gives a significant contribution to the experimental heat flux.

4.5 Acceleration through a sudden contraction

In this validation case, a gas is accelerated through a sudden contraction as shown in figure 4.10. The total length of the 2D computational domain is 4 cm, which is divided in a 2 cm long section which is 2 cm high and a 2 cm section which is 0.2 cm high. The conditions of the more or less stagnant gas at the inlet on the left are a temperature T of approximately 700 K and a number density n of $1.0 \cdot 10^{21}$ m^{-3} (giving Kn=0.970 based on the upstream gas conditions and the height (2 mm) of the contraction), $3.0 \cdot 10^{21}$ m^{-3} (giving Kn=0.320), and $1.2 \cdot 10^{22}$ m^{-3} (giving Kn=0.081). At the exit on the right the boundary condition is a vacuum. The surfaces are all specularly reflecting, which prohibits energy transfer to or from the gas at the surfaces. At the bottom of the domain, this specular surface can also be seen as a symmetry plane, as there is no (computational) difference between a specularly reflecting surface and a symmetry plane.

During the acceleration through the contraction towards the vacuum, the temperature of the gas decreases rapidly. This decrease can be explained by noting that the energy required for the acceleration of the molecules can only be provided by the internal energy of the gas. The temperature change ΔT (in K) can be derived using standard thermodynamical principles

and is written as:

$$\Delta T = -\frac{mN_A}{2c_p}\left(v^2 - v_{inlet}^2\right) \tag{4.9}$$

In this equation, m is the molecular mass (in kg), N_A is Avogadro's number, c_p is the molar specific heat at constant pressure (in J mol^{-1} K^{-1}), v is the average gas velocity (at the location for which the temperature difference is being calculated), and v_{inlet} the velocity at the inlet. In the computations, argon gas was used (with VSS parameters) for which $c_p = \frac{5}{2}R$, with R the universal gas constant.

Numerical results for this problem were obtained using the STARS and X-Stream codes, as well as the DSMC2 code by Bird [1]. The comparison of these three results for the Kn=0.970 case can be seen in figure 4.11(a). In this and all subsequent figures, the temperature profile in the lowest row of cells next to the bottom surface is presented. It can be seen clearly that the resulting profiles are almost identical for all three codes.

In figures 4.11(b), 4.11(c), and 4.11(d), the STARS results are compared to the theory of equation 4.9. The velocity v, which is required for evaluation of equation 4.9 is taken from the simulation results. From these three figures, it becomes clear that the difference between the numerical and theoretical results increases with increasing Kn, even though the validity of equation 4.9 does not depend on the Knudsen number. The reason for this difference is the fact that the gas is not in equilibrium, especially in the high speed part of the flow. As a consequence, the temperature calculation as described in section 2.6 (which is based on the assumption that the velocity distribution is Maxwellian), no longer gives accurate results.

Alternatively, the temperature can be calculated from the pressure, using the surface pressure and the ideal gas law. The surface pressure is simply defined as the total momentum change of all molecules that collide with the surface per unit of area and per unit of time. In an equilibrium situation, both methods of calculating the temperature will lead to the same result. To distinguish the temperature calculated according to section 2.6 (and the pressure which is derived from this temperature), and the temperature that is derived from the surface pressure, subscript labels 'flow' and 'wall' will be used below.

Figure 4.12 shows the temperature (left y-axis) and pressure (right y-axis) calculated using both methods. Comparing the lines marked T_{flow} and T_{wall}, it is clear that there is a significant difference between the two methods, especially at the location of the contraction, but also in the high speed part of the flow. In this part of the flow, the T_{wall} line compares much better to the theoretical temperature according to equation 4.9 than the original T_{flow} result, while both methods give good results at the inlet for obvious reasons.

With these results, the trend that lower Kn gives a better agreement with theory, which was observed in figure 4.11, can be explained. At lower Kn, the deviation from equilibrium becomes smaller, and the calculation of the flow temperature becomes more accurate. This can be seen most clearly in the results for Kn=0.081 (figure 4.11(d)), where the numerical results are seen to be almost identical to the theory.

The main conclusion at the end of this section is that both the STARS and X-Stream codes show the correct behavior in this validation case. The reason for the deviation from the

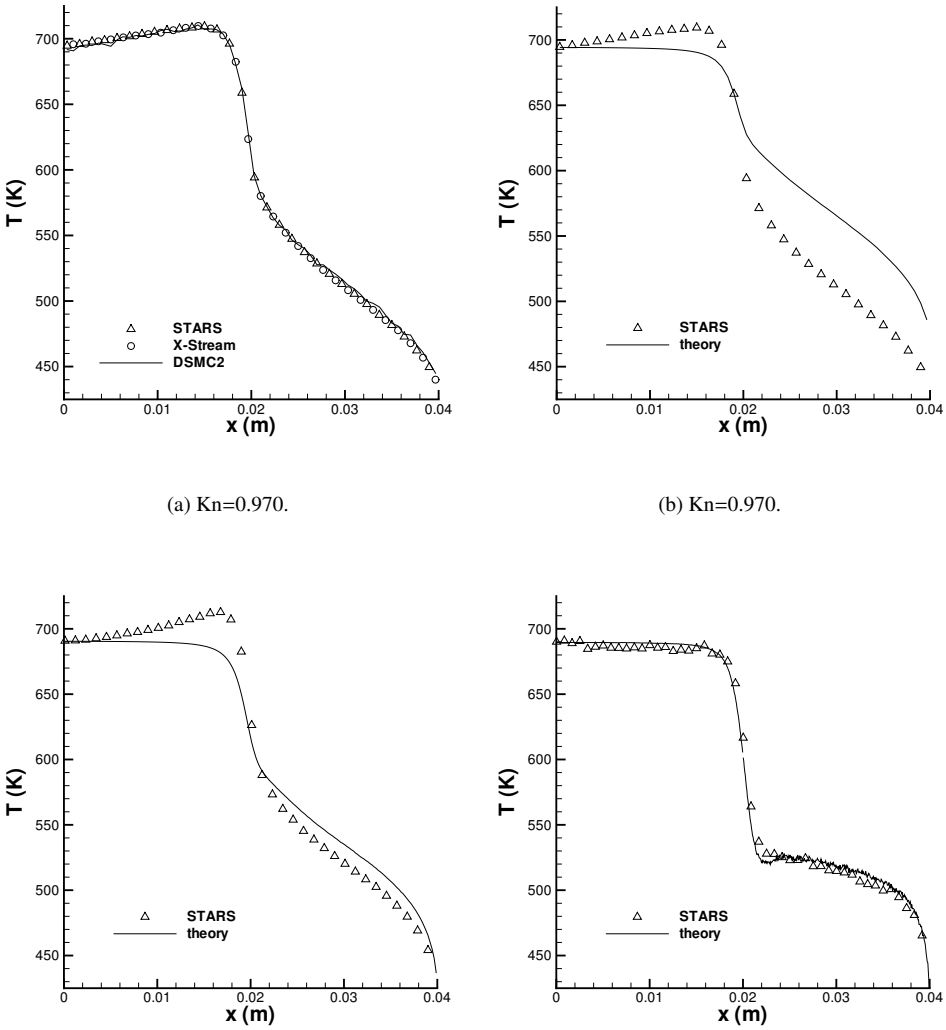

(a) Kn=0.970.

(b) Kn=0.970.

(c) Kn=0.320.

(d) Kn=0.081.

Figure 4.11: Results for the gas flow trough a sudden contraction at different upstream Kn numbers. Top left: comparison of the STARS, X-Stream and DSMC2 results. Other figures: comparison of the STARS results with the theory of equation 4.9 for different Kn.

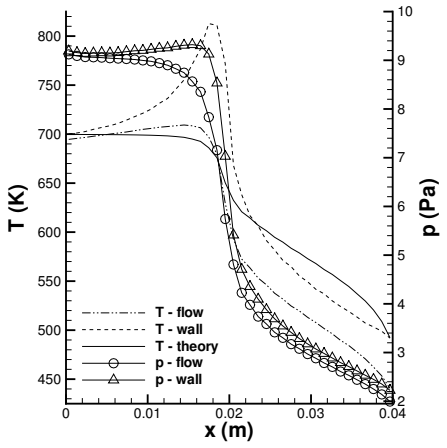

Figure 4.12: Results for the calculations at Kn=0.970, showing the effect of the non equilibrium velocity distribution on the temperature and pressure calculations. The temperature scale is on the left y-axis, the pressure scale on the right y-axis.

theory in equation 4.9 at high Kn is understood, and at low Kn an almost perfect agreement is obtained.

4.6 Gas flow in a semiconductor process chamber

Shufflebotham et al. [50] have performed an experimental and numerical investigation of the gas flow in a semiconductor process chamber. The experimental setup consisted of a stagnation flow geometry as shown in figure 4.13. Nitrogen gas was injected through a total of 16 small inlet holes evenly distributed around the circumference of the gas inlet plate. The gas flow at the inlet is sonic (choked flow) and has a temperature (due to the temperature decrease arising from the adiabatic expansion through the holes) of 239 K. The temperature of most surfaces was 298 K, except for the susceptor which was heated to 303 K. The pump at the outlet operated at a pump speed of 2000 l/s (manufacturer data). It should be noted that, at the pressures relevant for this case, the pump speed as given by the manufacturer is expected to have a significant (but unknown) uncertainty.

Pressure profile measurements were taken at three locations. Two radial profiles were measured at 0.5 inch (1.27 cm) and 2.5 inch (6.35 cm) upstream of the susceptor, and an axial profile (at r=0) was measured upstream of the susceptor. Different inlet conditions were used, with the flow rate varying between 100 and 500 standard cubic centimeters per

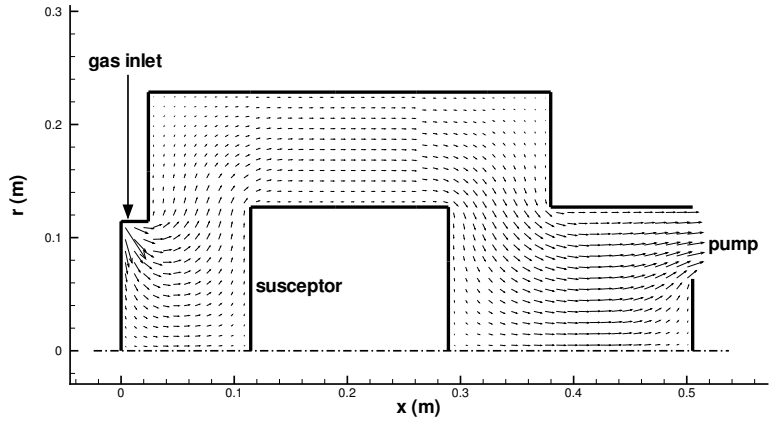

Figure 4.13: The geometry used for the calculation of the gas flow in a chamber.

minute (sccm). The pressures in the system (at the measuring locations) varied between approximately 0.15 and 0.7 Pa.

As noted above, Shufflebotham et al. performed 2D axi-symmetric DSMC simulations on this case. In these simulations, the 16 inlet holes reduced to a thin slit. To obtain an acceptable expansion of the inflowing gas, the DSMC collision step was turned off in the (single) cell which contained the inlet. This leads to an acceptable agreement with a realistic expansion behavior [51].

The pump action was treated physically, i.e. a certain number of computational particles N in the pump volume is removed from the simulation at each time step Δt [51]. The exact value of N depends on the pump speed S and the number density n just above the pump entrance:

$$N = \frac{\Delta t S n}{F_{num}} \tag{4.10}$$

The exact size of the pump volume is not relevant, as long as it is large enough to contain more particles than that are to be removed.

For the validation of the STARS and X-Stream codes, 2D axi-symmetric (STARS) and 3D (X-Stream) calculations were performed on this problem. The 100 sccm case was calculated using both codes, while the STARS code was also applied to the 200 sccm case. It is expected that the 3D X-Stream results will give better agreement to the experimental data, especially because of a better representation of the gas inlets. For the STARS simulation, small changes were made in the code to correctly represent the gas inlet and pump outlet. These changes were very similar to those described above for Shufflebotham's calculations. The X-Stream code, being fully 3D, was not altered. At the inlet, the jets were calculated fully 3D, with the jet opening equal to the size of the face of a single cell. The dimensions of this face are

significantly larger than the size of the inlet holes in the experiments. At the outlet, a stream boundary was used with properties (pressure, temperature and velocity) as taken from the STARS result.

The STARS and X-Stream pressure results are shown in figure 4.14, together with the experimental results. The top two figures show the computational results of the STARS and X-Stream codes for the radial profiles at 0.5 and 2.5 inch upstream of the susceptor for the 100 sccm experimental case. The bottom left figure shows the STARS radial profile results for the 200 sccm case, and the bottom right figure shows the axial profiles for both cases and both codes. Each figure also contains the relevant experimental data.

Figure 4.14(a) shows that the STARS results for the radial pressure profiles agree with the experimental data in order of magnitude. The numerical and experimental profiles show a similar trend, but the exact shape of the experimental profile, with a sharp decrease, a minimum and then a plateau, is not reproduced accurately. Also, the difference between the two profiles (at 0.5 and 2.5 inch upstream of the susceptor) is much more pronounced in the experimental data. The results for the 200 sccm case (figure 4.14(c)) shows very similar deviations from experiments.

The 3D X-Stream simulation (figure 4.14(b)) shows almost exactly the same behavior as the STARS simulation. Concerning these 2D simulations, this seems to indicate that it is adequate to turn off molecular collisions in the first cell near the inlet to obtain an accurate jet expansion. The 3D pressure results are slightly higher than the 2D results, and show a slightly better comparison to the experimental results for small r.

Finally, the last figure shows the axial pressure profiles for all cases. As expected, the 2D STARS and 3D X-Stream almost coincide. Both simulation results do not predict the correct profile shape, giving a more or less constant pressure throughout the displayed range. This corresponds to the findings of the DSMC simulations of Shufflebotham et al. (not shown), who find a comparable flat axial profile.

Summarizing, the 2D STARS and 3D X-Stream predictions agree well with each other due to the slight adaptations in the STARS code. The jet expansion at the inlet is captured well in the 2D simulations when the collisions in the first cell are turned off. In the 3D simulations, this alteration of the DSMC method is not needed. The numerical results of both codes only agree with the experimental data in order of magnitude, as the experimentally determined pressure minimum is not recovered in the simulations. These findings correspond to the DSMC simulation results of Shufflebotham et al. (not shown), who report a similar behavior. Note that in Shufflebotham's 2D simulations, the jet inlet is also modeled by prohibiting collisions in the first cell.

As for the 3D X-Stream calculation, a better agreement could be expected. The most likely reason for any mismatch is the modeling of the jet inlets. As noted above, the dimensions of the inlet holes, which were modeled as a mass flow boundary, were larger than the holes used in the experiments. However, the difference between experimental and numerical data is much larger than would be expected based on this minor difference. Certainly, the complete absence of the pressure minimum in the numerical profiles cannot be explained in

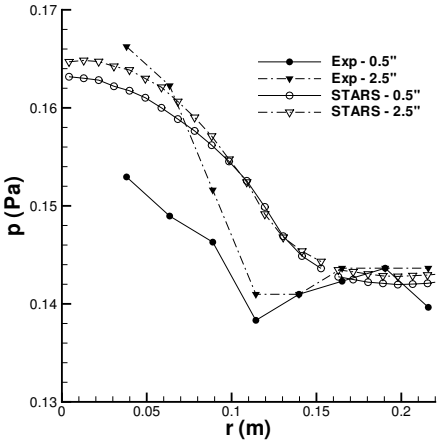

(a) STARS radial pressure profile with 100 sccm flow at 0.5 and 2.5 inch upstream to the susceptor.

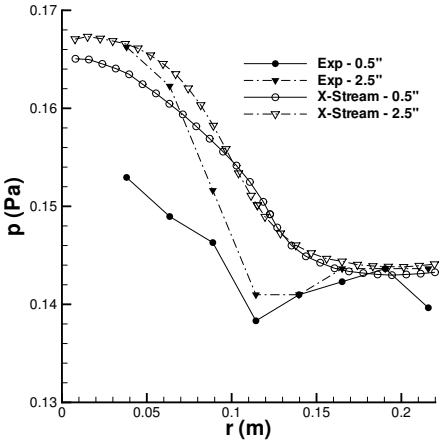

(b) X-Stream radial pressure profile with 100 sccm flow at 0.5 and 2.5 inch upstream to the susceptor.

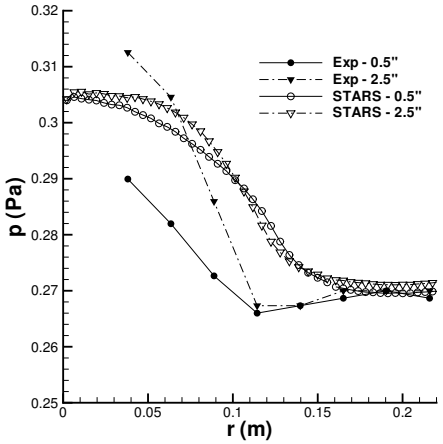

(c) STARS radial pressure profile with 200 sccm flow at 0.5 and 2.5 inch upstream to the susceptor.

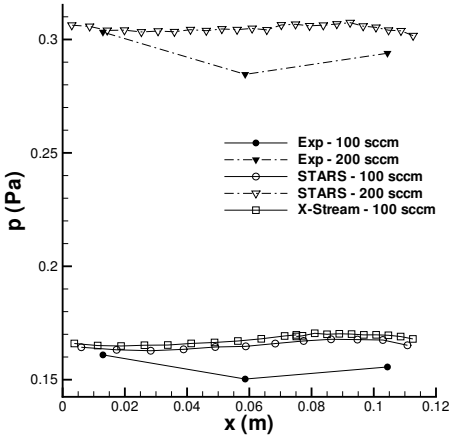

(d) STARS and X-Stream axial pressure profiles (100 & 200 sccm). $x = 0$ is located at the susceptor.

Figure 4.14: Pressure profiles of the CVD chamber gas flow case for 100 and 200 sccm flow.

this way.

In the given geometry, there is no reason to expect a minimum in the pressure, even though this minimum appears at a radial position which is equal to the radius of the susceptor. As three different DSMC codes all obtain very similar results, the question arises whether an important detail of the experiments was overseen. For example, the experimental pressure measurements were performed using two displacable manometers, which might have influenced the local flow conditions. In this context, it must also be noted that the data were taken at an equipment manufacturer, and not at a university lab [51].

4.7 Flow around a sphere

The main difference between the STARS and X-Stream codes is the fact that the latter is a fully three dimensional code. To validate the 3D particle movement routines of the X-Stream implementation, flow around a sphere was chosen as a validation test case.

Russell [52] measured the density distribution ahead of a sphere in a rarefied supersonic flow under varying conditions, and Wu et al. [53, 54] have published results of DSMC calculations of one of these experimental cases. Following Wu, we select as a test case Russell's experiment with a Reynolds number of 30, which is a nitrogen flow around a sphere with diameter $D = 1.28$ cm. The free stream conditions are a number density $n_\infty = 9.77 \cdot 10^{20}$ m^{-3}, temperature $T_\infty = 66.25$ K and velocity $v_\infty = 696.8$ m/s, resulting in a Mach number Ma = 4.20 and a Knudsen number $\mathrm{Kn}_\infty = 0.1035$ (based on the sphere diameter). The sphere surface is assumed to be fully diffusive and held at 300 K. The computational geometry (see figure 4.15) is constructed using a 45° segment of the flow, containing 8400 cells. The sphere curve is constructed using 56 segments.

Results of the calculation are presented in figure 4.16 and 4.17. Both figures show the flow properties on the stagnation line ahead of the sphere, with the distance on the x-axis scaled by the sphere diameter D. The center of the sphere is at $x/D = 0$, and the stagnation point is at $x/D = -0.5$.

The first figure shows the number density profile (made dimensionless with n_∞), comparing the X-Stream results to the measurements by Russell. Russell's data were obtained from a figure in the paper by Wu et al. [53]. The numerical and experimental data show a very similar behavior. A slightly steeper gradient is found in the simulations, this is in agreement with the DSMC results by Wu et al. (not shown), who obtain a very similar result. Given the experimental observation by Russell that low Reynolds flows are difficult to generate, and may give rise to some disturbance in the free stream flow, the comparison between the simulations and experiments is very satisfactory. This is confirmed by the fact that the X-Stream calculations give a density ratio at the stagnation point of 4.75, which is very close to the value of 4.8 reported by Wu et al.

Figure 4.17 shows results for the translational and rotational temperatures on the stagnation line. The X-Stream results are compared to the DSMC results by Wu et al., no experimental measurements of these quantities are available. The figure clearly shows an excellent

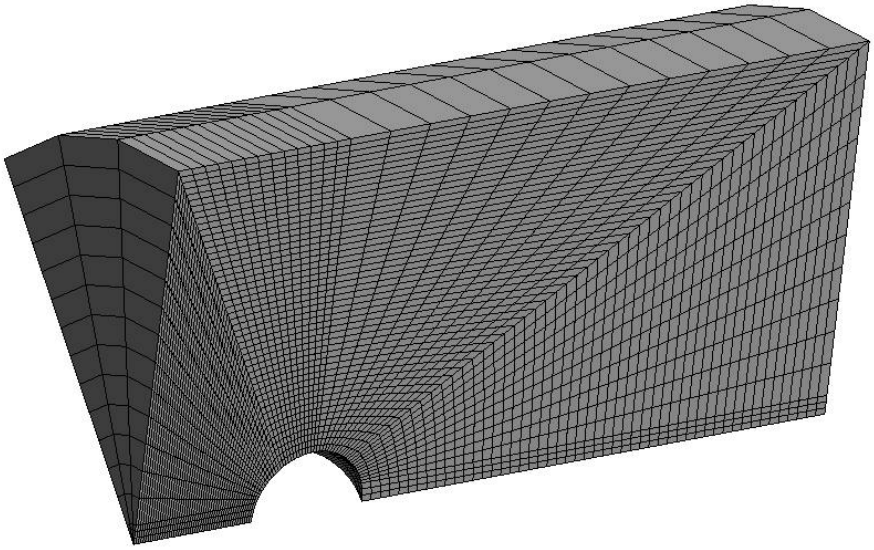

Figure 4.15: The 3D computational geometry for the calculation of the flow around a sphere.

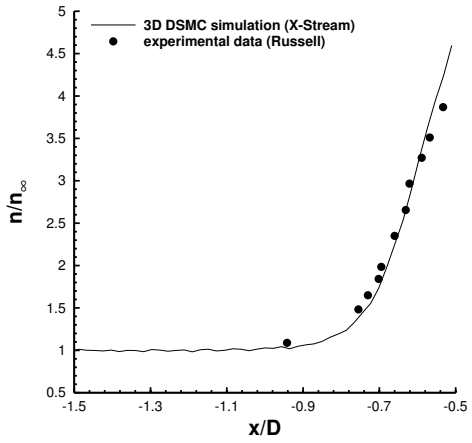

Figure 4.16: The number density profile on the stagnation line for the flow around a sphere. Shown are the 3D X-Stream DSMC simulation results and Russell's experimental data [52].

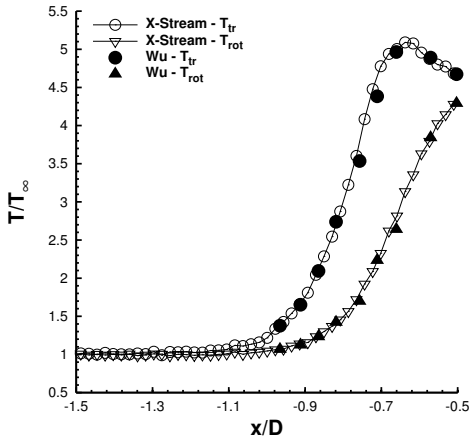

Figure 4.17: The translational and rotational temperature profiles on the stagnation line for the flow around a sphere. Shown are the X-Stream simulation results and Wu's simulation data [53].

agreement in the temperature profiles of both simulations.

Given the presented results, it can be concluded that the X-Stream code performs very well in this full 3D case with curved boundaries.

4.8 Consistency of chemistry routines

To check the implementation of the gas phase chemistry models as described in section 2.8, a zero dimensional STARS simulation was performed using 5 artificial species and 3 different artificial reversible reactions. The species will be referred to as A, B, C, AB and BC, and the following exchange, recombination and dissociation reactions are defined:

$$A + B \leftrightarrow AB \tag{4.11}$$

$$AB + C \leftrightarrow A + BC \tag{4.12}$$

$$A + C \leftrightarrow AC \tag{4.13}$$

The three atomic species A, B and C do not have internal energy modes, while AB and BC have both rotational and vibrational modes. The characteristic vibrational temperatures of AB and BC were defined to be of the order of the total temperature in the system. The dissociation energies were chosen such that the vibrational levels at which dissociation occurs were 8 and 7 for AB and BC, respectively.

The reaction rates for the exchange and recombination reactions are defined by Arrhenius parameters (equation 2.57), and the effect of these reactions can therefore be predicted analytically for this zero dimensional case using equations 2.56 and 2.66. The dissociation rates (i.e. of the reverse reactions of 4.11 and 4.13) are more difficult to predict, especially because the rotational energy is also included in the total energy available for dissociation. Nevertheless, it was attempted to derive an expression for the dissociation rate, keeping in mind that it will not be exact, by multiplying the collision rate and the dissociation probability during a collision. This dissociation probability was constructed using the (known) distributions of the vibrational levels and an estimate of the average collision energy. This last estimation is inaccurate due to the uncertainty in the effective number of vibrational degrees of freedom and the inclusion of the rotational energy in the total energy available for dissociation.

In figure 4.18, the results of the STARS computation are compared to these analytical formulas for different situations. Each sub figure shows the change in composition of the gas relative to the initial composition in which the number fractions of all species had an equal value of 0.2. Three sub figures show the effect of applying only one of the 6 reactions described above.

Figure 4.18(a) shows the results when only the forward reaction of equation 4.11 is applied. The STARS results for the changes in the gas composition due to this recombination reaction exactly follow the prescribed Arrhenius reaction rate.

Figure 4.18(b) shows the results when only the forward reaction of equation 4.12 is applied. This time, the STARS results slightly deviate from the analytical result. It was found that this is due to the difficulties associated with the determination of the effective vibrational degrees of freedom in equation 2.60. The result of a STARS simulation for which AB did not have any vibrational modes showed an excellent agreement to the analytical expression, comparable to the result for the recombination reaction described previously. Please note that the recombination reaction does not suffer from this shortcoming because the reactants involved do not have any vibrational modes.

Figure 4.18(c) shows the results when only the backward reaction of equation 4.11 is applied. As described above, the expression for the dissociation rate is not expected to be exact, and this is seen in the figure. The dissociation rate predicted by the approximate model is higher than the STARS rate. The dotted lines denote the same rate expression, but scaled (by slightly increasing the average collision energy which is required for the determination of the dissociation probability per collision) to fit the STARS results. This scaled expression adequately fits the simulated change in gas composition.

Finally, figure 4.18(d) shows the effect of applying all 6 possible reactions simultaneously. For the dissociation reactions, the scaled reaction rate expressions were used. Clearly, the STARS results for the changes in the composition in time show excellent agreement with those following from the rate expressions, leading to the conclusion that the gas phase chemistry works as expected.

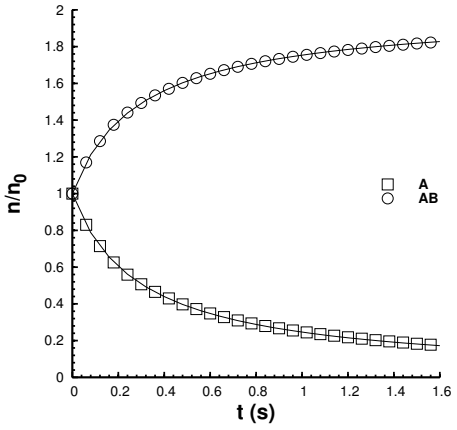

(a) Recombination reaction: $A + B \rightarrow AB$.

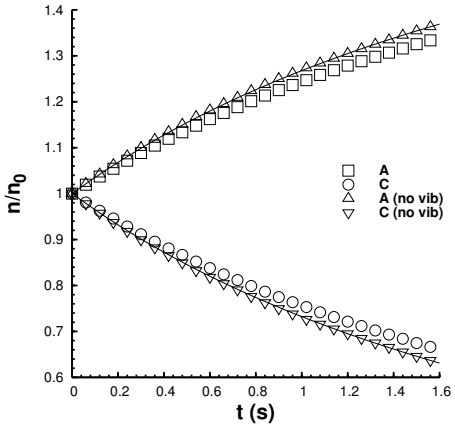

(b) Exchange reaction: $AB + C \rightarrow A + BC$. The STARS results with and without vibrational modes are both shown.

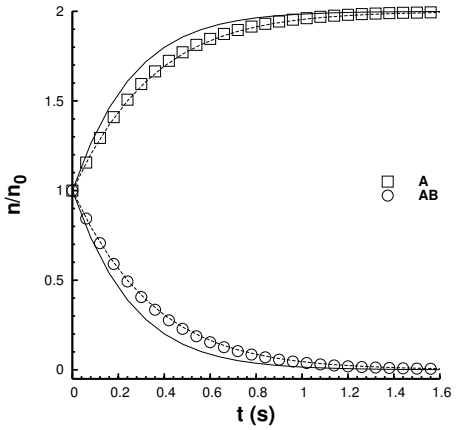

(c) Dissociation reaction: $AB \rightarrow A + B$. Shown are the unchanged (solid line) and scaled (dotted line) rate expression results.

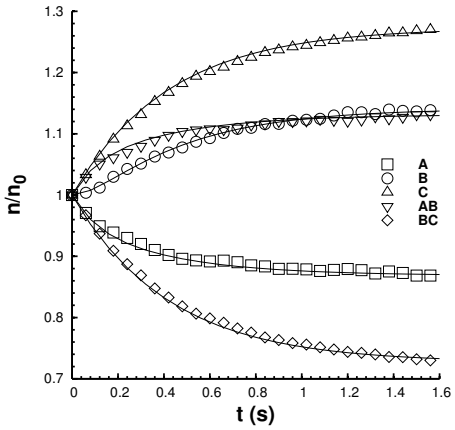

(d) All possible reactions.

Figure 4.18: Changes in gas composition due to chemical reactions in equations 4.11, 4.12, and 4.13. Shown are the STARS results (symbols) and the analytical solutions (lines).

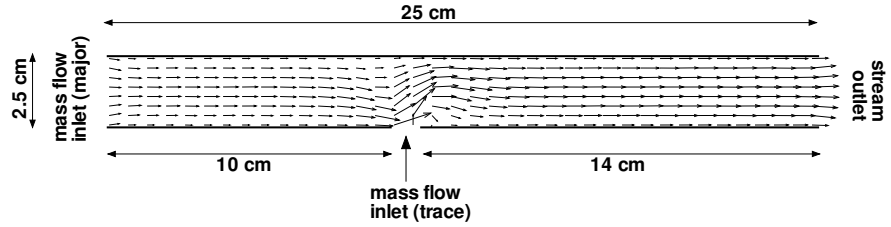

Figure 4.19: The geometry used in the validation of the species weighting implementation.

case	major mass flow (molecules/s)	trace mass flow (molecules/s)	trace fraction	time step (μs)	steady time (ms)	# time steps
1	$1.25 \cdot 10^{20}$	$1.25 \cdot 10^{19}$	0.1	1.0	2.5	$1 \cdot 10^{5}$
2	$1.25 \cdot 10^{20}$	$1.25 \cdot 10^{18}$	0.01	1.0	2.5	$1 \cdot 10^{5}$
3	$1.25 \cdot 10^{20}$	$2.50 \cdot 10^{17}$	0.002	0.1	1.5	$2 \cdot 10^{5}$

Table 4.1: Description of the species weighting validation cases. The time step for the case 3 simulations was reduced to prevent crashes of the program. Due to the extremely large number of computational particles required for the simulation without WF, the calculation was distributed over 5 processors. Unfortunately, the MPI protocol could not handle the large communications between blocks for the 1 μs time step, but a reduction of the time step solved this problem.

4.9 Validation of species weighting routines

To validate the species weighting routines as described in section 2.10, a series of simulations including small concentrations of trace species was performed with STARS both with and without weighting factors (WF). The 2D plane geometry that was used for these simulations is shown in figure 4.19. The main flow (of the major species) in this case is from the mass flow inlet (on the left) to the stream outlet (on the right). A trace species is injected into the flow through another mass flow inlet (at the bottom). The different conditions for the 3 cases that were examined are listed in table 4.1. As can be seen in this table, the major species number flow is identical for all cases, but the trace species number flow varies between 0.2 and 10% of the major species flow. Corresponding species fractions are also applied at the stream outlet, with the overall outlet number density fixed to the constant value of $2.0 \cdot 10^{20}$ m^{-3} for all cases. The Knudsen number at the outlet is approximately 0.28.

The computational domain is 25 cm long and 2.5 cm high. The trace mass flow inlet is 1 cm wide and starts 10 cm downstream of the main mass flow inlet. The temperature boundary conditions are 300 K, except for the trace mass flow boundary, which is at 500 K. All surfaces are diffusely reflecting, and each simulation uses 150x15 cells. In the results presented here, both the major and trace species have the properties of argon, using the VSS model.

For each case, results of the trace species number density n_{trace}, the number flux F_{in} of trace species molecules that collide with the top surface (located opposite to the trace inlet), as well as the incoming trace species momentum flux (denoted by mv to prevent confusion with the pressure) are compared for simulations with and without WF. The results are shown in figure 4.20. This figure shows results for the profile of n_{trace} along the channel at three different heights and the results on mv and F_{in} as a function of the distance coordinate along the top surface.

The DSMC scatter in the case 3 solutions is much larger than for case 1 and 2. The reason for this is that the case 3 calculations were performed with a smaller total simulated time (see table 4.1), leading to less effective sampling due to correlations between consecutive samples (also see section 2.5).

Careful examination of these figures shows that in all three cases, the results of the simulations (with identical major and trace species VSS parameters) with and without WF yield almost identical results for all variables shown. Other simulations (not presented here) using different VSS parameters for the major and trace species also show this excellent agreement between simulations with and without WF. To increase the system sensitivity to fluctuations in the total energy (as described in section 2.10), some simulations were also performed with specularly, instead of diffusely reflecting surfaces. Again, the results for simulations with and without WF (also not shown) are very similar.

Table 4.2 clearly shows the advantage of using WF in simulations with trace species. As can be seen, the case 1 simulation without WF took 15 hours to finish, which is almost 3 times longer than the simulation using WF. For case 2, this ratio is 23 and for case 3 almost 90. Please note that for case 3 two times more time steps were computed compared to cases 1 and 2.

At the end of this section, it can be concluded that the species weighting method as described in section 2.10 is very useful for simulations with trace species. It was shown that, for an 'open' geometry (allowing for physical fluctuations of the total energy, i.e. with inlets, outlets and/or diffusely reflecting surfaces), a simulation with weighting factors produces identical results as a simulation without weighting factors, but in a much shorter (wall) time.

4.10 Concluding remarks

At the end of this chapter, it can be concluded that both the STARS and X-Stream codes perform well in all the validation cases. The results of the two codes match with each other for identical calculations, and also with the results of other DSMC codes. Also, a good

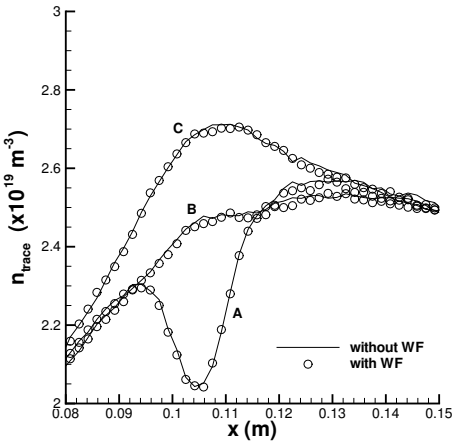

(a) Trace species number density profiles (case 1).

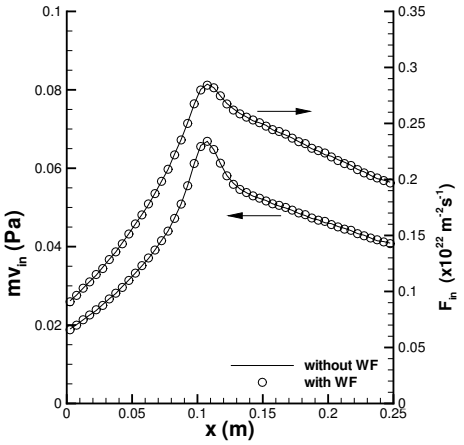

(b) Trace species momentum (mv_{in}) and number (F_{in}) fluxes (case 1).

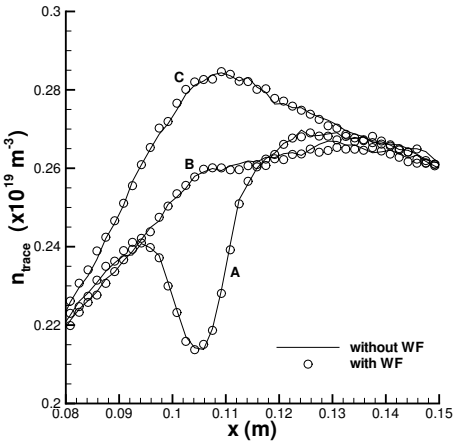

(c) Trace species number density profiles (case 2).

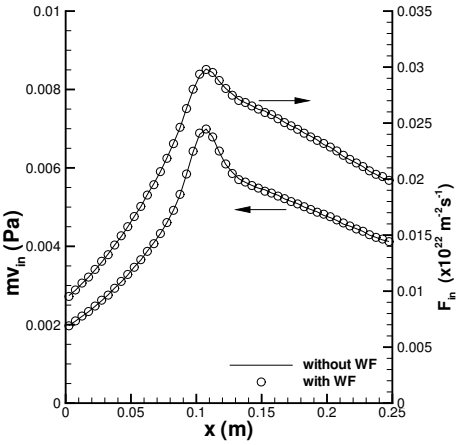

(d) Trace species momentum (mv_{in}) and number (F_{in}) fluxes (case 2).

Figure 4.20: *(Continued on next page)*

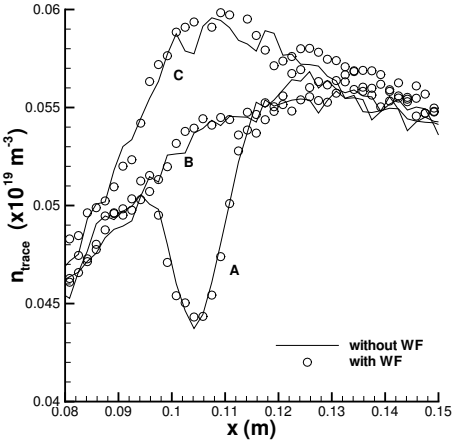

(e) Trace species number density profiles (case 3).

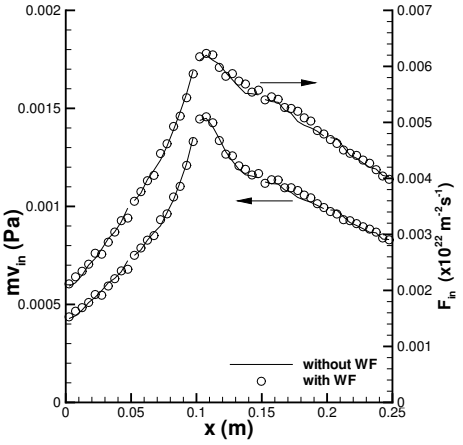

(f) Trace species momentum (mv_{in}) and number (F_{in}) fluxes (case 3).

Figure 4.20: *(Continued from previous page)* Comparison of the simulations with and without species weighting factors (WF) for cases 1-3 (see table 4.1). Profiles of the trace species number density n_{trace} are shown on the left. The three lines are profiles at the bottom (A), center (B) and top (C) of the channel. Trace species momentum (mv_{in}) and number (F_{in}) fluxes to the top surface are shown on the right.

case	WF used ?	WF ratio	wall time (h)	# major particles	# trace particles
1	no	-	15.0	$546 \cdot 10^3$	$42 \cdot 10^3$
	yes	7.0	5.2	$78 \cdot 10^3$	$42 \cdot 10^3$
2	no	-	133.6	$5686 \cdot 10^3$	$44 \cdot 10^3$
	yes	70.0	5.8	$81 \cdot 10^3$	$44 \cdot 10^3$
3	no	-	879.1	$28522 \cdot 10^3$	$45 \cdot 10^3$
	yes	350.0	9.8	$82 \cdot 10^3$	$46 \cdot 10^3$

Table 4.2: Simulation data of the species weighting validation cases. The case 3 calculation without WF was calculated on 5 processors, the total calculation time is therefore estimated as 5 times the actual time, multiplied by an estimated efficiency of 0.8.

agreement with experimental data or analytical equations is obtained in almost all cases. In cases where the agreement was not good, satisfactory explanations of the cause of the differences were given.

It was also shown that the chemistry and species weighting implementations function very well.

5. Zinc deposition experiments for validation of Direct Simulation Monte Carlo calculations of rarefied internal gas flow

This chapter describes a validation experiment that was performed for the sole purpose of validating the STARS and X-Stream DSMC codes for a film deposition process.

The entire chapter has been submitted to the Journal of Vacuum Science and Technology A [55] with the title 'Zinc Deposition Experiments for Validation of Direct Simulation Monte Carlo Calculations of Rarefied Internal Gas Flows'. The authors are R. Dorsman, J.F.M. Velthuis[1], J.P. Zijp[1], A.M.B. van Mol[1] and C.R. Kleijn. As a result, this chapter shows some overlap with other parts of this thesis.

5.1 Abstract

Specially designed experiments were performed for the validation of Direct Simulation Monte Carlo calculations of rarefied internal gas flows. Hot zinc vapor was released into a cold-wall deposition chamber filled with a background gas at low pressure in which two silicon wafers were mounted. The deposited zinc layers on these wafers have been measured in four different experiments, with varying background gas species (argon and helium) and background pressures (0.031 - 0.25 Pa). The background gas conditions were chosen such that the Knudsen numbers based on the zinc mean free path range from 0.34 to 2.8. The experimental results have been compared to simulation results.

[1]TNO, Stieltjesweg 1, Delft, The Netherlands

5.2 Introduction

In recent decades, Computational Fluid Dynamics has become a very important tool in fluid flow engineering. It is generally based on the numerical solution of the Navier-Stokes (and related) equations. The underlying assumption that the fluidum can be treated as a continuum loses its validity for gas flow at high ($\gtrsim$0.01) Knudsen numbers. More specifically, for vacuum equipment with typical flow dimensions of cm's to dm's, the continuum assumption becomes invalid for pressures below 50-500 Pa (for N_2 at 300 K).

The Direct Simulation Monte Carlo (DSMC) [1] method is the most widely used simulation method for rarefied engineering type flows, in which the mean free path is not negligible compared to the characteristic flow dimensions. The method was developed by G.A. Bird in the 1960's [56], and has since been applied primarily to rarefied flows in hypersonic space applications, e.g. Space Shuttle re-entry flow calculations [57]. The DSMC method is based on tracing the individual paths of a large number of computational particles, which each represent a sample from the real molecules in the gas. It has been shown [3] that solutions of the DSMC method converge to solutions of the Boltzmann equation for large numbers of computational particles. In the last decade, the DSMC method has also been applied to film deposition processes, e.g. sputtering [58], flows around sub-micron features on a wafer [59] and a full silicon deposition process [60].

A multi-purpose, 3D, curvilinear mesh Direct Simulation Monte Carlo (DSMC) code [61, 62] based on the method as described by Bird [1] is being developed in collaboration between the Delft University of Technology and the Netherlands Organization for Applied Scientific Research TNO for calculating internal rarefied gas flows with chemical reactions. One of the main application area's for the newly developed code is the field of Chemical Vapor Deposition (CVD) [63]. The code has been validated using a wide range of literature results, but no useful experimental data was found in the field of deposition of thin films. The main reason for this is the fact that most experiments are aimed at creating perfectly uniform films, e.g. [64], which is not ideal from the validation point of view. Also, existing literature usually does not provide precise information of the conditions, e.g. temperature and pressure.

Therefore, this paper presents measurements in an experimental setup in which the conditions could be monitored and controlled with sufficient accuracy, and, more importantly, in which the deposited films were not uniform. The goal of the experiment was to deposit a thin metal film on a surface, and to compare thickness measurements of this film to DSMC calculations.

5.3 Experiments

The experiments were performed in a large ($\sim$1 m^3) Balzers BAK vacuum vessel which could be evacuated down to around 10^{-5} Pa with a diffusion pump. An accurately known argon or helium background pressure could be introduced in the vessel. Inside the large vessel, a smaller ($\sim 1.5 \cdot 10^{-3}$ m^3) cold-wall deposition chamber was used for the actual experiment.

The (chrome coated) copper deposition chamber (see figure 5.1) was connected to the vessel through a large 4 cm hole at the top. An effusion source filled with liquid zinc was mounted at the bottom of the chamber. This source provided a steady flux of hot zinc vapor into the chamber, where the zinc would deposit on the cold walls. To facilitate measurements of the deposited layers, two silicon wafers were mounted inside the chamber. The wafer closest to the zinc source will be referred to as the bottom wafer, the other one as the top wafer. The wafers could be removed from the setup after the deposition experiment to be subjected to zinc layer thickness measurements.

The experimental procedure consisted of the following steps:

- aeration of the vacuum vessel
- placement of new wafers inside the chamber
- evacuation of the vessel to $2{\cdot}10^{-4}$ Pa or lower (measured on a separate Bayard-Alpert ion gauge), which is at least a factor 100 lower than the lowest operating pressure
- heating of the source and waiting for the zinc to melt and reach the required temperature (± 25 minutes)
- introduction of the background gas, and waiting for stabilization until the required pressure is reached (± 5 minutes)
- opening and closing of the shutter, that separates the zinc source from the deposition chamber (300 seconds open time)
- closing of the background gas supply
- cooling of the zinc in the source until solidification (± 7 minutes)
- (after cooling to below 100°C) aeration of the vacuum vessel
- removal of the wafers, immediately followed by evacuation of the vessel (note that the small amount of zinc that deposited on the walls of the chamber was not removed between consecutive experiments)
- ex-situ measurements of the local zinc layer thicknesses on the wafers

An arrangement of a shutter and shutter plate (aluminum) was needed to be able to determine the deposition time accurately. In the closed position, the combination of the shutter and the shutter plate could completely separate the top of the chamber from the zinc source. This was necessary to prevent zinc from depositing on the wafers during the heating and cooling of the source. It was checked experimentally that no zinc reached the wafers with the shutter closed.

Figure 5.1 shows a schematic overview of all components in the axi-symmetric geometry. The inner diameter of the chamber is 11.5 cm. The height of each of the three sections is

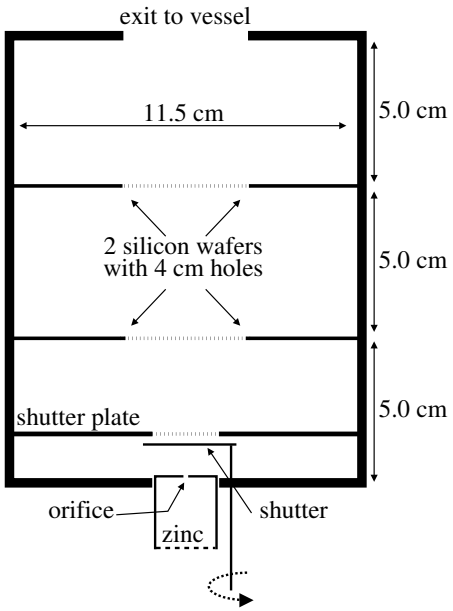

Figure 5.1: The geometry of the deposition chamber. The wafer closest to the zinc source will be referred to as the bottom wafer, the other one as the top wafer. Note that only the shutter can be rotated. The shutter plate is fixed.

5.0 cm. The vertical distance between the orifice and the bottom wafer is 4.75 cm. The shutter plate is fixed 1.6 cm above the chamber bottom and has a 2 cm Ø hole. The wafers used for the experiment were prepared with a 4 cm hole in the center to let the zinc flow past both wafers and to allow the background gas to reach all parts of the deposition chamber.

5.3.1 Background gas conditions

Three of the four experiments were performed using argon as a background gas at three different pressures: 0.031, 0.088, and 0.25 Pa. The mean free path λ of zinc atoms at room temperature in these situations is 14, 5.0, and 1.7 cm, respectively. This gives Knudsen numbers (defined as λ/H with H the distance between the two wafers) of 2.8, 1.0, and 0.34, showing clearly that the experimental conditions are in the rarefied flow regime. The last experiment was done using helium at 0.088 Pa. The mean free path of zinc is 3.0 cm at this pressure, resulting in a Knudsen number of 0.60. The background pressure could be obtained and kept steady using a needle valve gas inlet in combination with a throttle on the diffusion

pump. Accurate measurements were done in the large vacuum vessel using a Pfeiffer CMR 275 capacitance gauge, with an error of less than 1% of the measured value.

The main influence of the background gas conditions on the deposition profile is to be expected on the top wafer. When the pressure is low, zinc atoms travel from the orifice to the wafers (almost) without collisions. The resulting deposition profile on the top wafer will then have a sharp transition due to the shadow effect of the bottom wafer. At high pressures, the zinc atoms collide a few times before reaching the top wafer, and thus the shadow effect will be much less, and the transition much smoother.

5.3.2 Temperature control

Zinc was evaporated from a commercial effusion source (NTEZ40 from MBE), which contained two type K thermocouples and a hot filament to heat the contents. The temperature was controlled using a PID controller and one of the two available thermocouples. The reading of the thermocouple differed from the actual zinc temperature. Calibration was done using a thermocouple inside the zinc. The difference between the reading and the zinc temperature was approximately 35 K. The calibration also provided data about the time it took for the zinc temperature to reach the steady state. The zinc in the source was kept at a steady temperature of 718 K, which is just above the melting temperature of 692.7 K.

The source was separated from the chamber by a small 2 mm Ø orifice which was 0.2 mm thick. The temperature of the orifice was actively monitored using a thin type K thermocouple and maintained at a value of 700 K by a PID controlled resistance heater soldered onto the orifice. This was necessary to prevent formation of a solid zinc film on the orifice which could eventually block the hole. The temperature of the walls of the deposition chamber was measured during all experimental runs using a standard type K thermocouple. Due to the large thermal mass of the chamber, the temperature did not significantly vary from the room temperature of ~292 K. The temperature of the bottom wafer was also monitored using a thermocouple. Its temperature increased slightly during an experimental run due to the radiation from the heated orifice, but the temperature never exceeded room temperature by more than 8 K.

5.3.3 Surface treatment

Before each experimental run, the wafers were cleaned extensively in a nitrogen and in an oxygen plasma barrel etcher run. It was found that the sticking coefficient of zinc atoms on the silicon itself (even after extensive cleaning) was very low, and therefore the lower sides of the wafers (i.e. the sides facing the zinc source) were coated with a thin (50 nm) molybdenum layer to improve sticking of the zinc. The top sides were not coated. As a result, very little zinc deposited on these top sides. Also, very little zinc was found to deposit on all other walls in the deposition chamber.

After an experimental run, the wafers were processed as quickly as possible to reduce the influence of the formation of a zinc oxide layer (see section 5.5). The zinc layer was removed

along two thin (~1 mm wide) lines, extending radially from the inner to the outer edge of the wafer. The thickness of the zinc was measured at various radial locations along each of the two lines. These measurements were performed using a Veeco Dektak 8 surface profiler with a 5 μm tip and a force of 4 mg. The inaccuracy is approximately 5 nm.

The zinc removal was done by HCl etching. The path to be etched was first surrounded by polyamide tape. Then diluted HCl was applied to the exposed zinc and washed away with purified water after approximately 30 seconds. The tape was then removed and the wafer dried using clean N_2 gas. Zinc is quickly dissolved in the HCl solution, while the molybdenum layer is not affected. No zinc was found on the tape after removal.

5.4 Numerical simulations

The DSMC method is a particle based simulation method which calculates flow properties by tracing the path of a representative number of molecules (including intermolecular collisions) and sampling their properties. This particulate basis of the method allows accurate investigation of non-equilibrium flows as encountered in rarefied flow regimes because the local molecular velocity and energy distributions are allowed to vary freely. Physical phenomena such as velocity slip and temperature jump at a surface, which are known to occur in situations where the mean free path of the gas is large, can therefore be reproduced accurately.

The two main assumptions of the method are

- the tracing of only a relatively small (compared to the number of molecules in the real flow) but representative number of computational particles N, with typically $N = 10^5 - 10^7$
- the decoupling of the translation and collision phase for these particles within a (small) time step.

As a result, the ratio F_{num} between the number of real molecules and the number of computational particles and the simulation time step Δt are important parameters. Another important parameter is the size of the cells that are used for the Monte Carlo collision routine (which is needed because of the first assumption) and the flow sampling. More details can be found in [1].

The computations for the current paper were performed using a parallelized multi-block DSMC code, with a 2D axi-symmetric computational domain that included the entire deposition chamber. The Variable Soft Sphere (VSS) [12] collision model was used for the intermolecular collisions. The VSS parameters for the species can be found in table 5.1. The DSMC time step Δt, the ratio between real and simulated molecules F_{num}, and the sampling cell size for the different simulations can be found in table 5.2. The simulations were assumed to have reached a steady state after t=0.2 s, during which time an average zinc atom (with a thermal velocity at 300 K of 312 m/s) travels approximately 1250 times the distance H between the two wafers.

	Zinc	Argon	Helium
molecular mass (kg)	$108.6{\cdot}10^{-27}$	$66.3{\cdot}10^{-27}$	$6.65{\cdot}10^{-27}$
reference diameter (m)	$4.05{\cdot}10^{-10}$	$3.50{\cdot}10^{-10}$	$2.13{\cdot}10^{-10}$
reference temperature (K)	700	700	700
viscosity temperature exponent	0.88	0.74	0.64
VSS parameter α	1.68	1.50	1.21

Table 5.1: Species parameters for VSS collision model.

pressure	Argon 0.031 Pa	Argon 0.088 Pa	Argon 0.25 Pa	Helium 0.088 Pa
Δt (s)	$5.0{\cdot}10^{-6}$	$5.0{\cdot}10^{-6}$	$1.5{\cdot}10^{-6}$	$5.0{\cdot}10^{-6}$
F_{num}	$1.0{\cdot}10^{11}$	$3.0{\cdot}10^{10}$	$8.0{\cdot}10^{9}$	$3.0{\cdot}10^{10}$
cell size far from orifice (m)	$5.0{\cdot}10^{-3}$	$2.5{\cdot}10^{-3}$	$1.25{\cdot}10^{-3}$	$2.5{\cdot}10^{-3}$
cell size near orifice (m)	$4.75{\cdot}10^{-3}$	$1.85{\cdot}10^{-3}$	$1.0{\cdot}10^{-3}$	$1.85{\cdot}10^{-3}$

Table 5.2: DSMC calculation settings.

The incoming zinc flux at the orifice was modeled using a mass flow boundary condition. The flux F of zinc atoms through the orifice can be calculated using the following equation for the zinc vapor pressure p_v [65, p. D-215]:

$$\log_{10}\left(\frac{p_v}{p_0}\right) = -22.56\frac{T_0}{T} + 5.233 \tag{5.1}$$

with the reference temperature T_0=273.15 K and the reference pressure p_0=10^5 Pa. The temperature T is taken to be the lowest temperature in the system surrounding the liquid zinc, in this case the temperature of the orifice (700 K). The flux F can now be calculated as $\frac{1}{4}n_v c$, with n_v the vapor number density (calculated from equation 5.1 and the ideal gas law), and $c = \sqrt{\frac{8k_bT}{\pi m}}$ the thermal velocity, leading to $F = 3.30 \cdot 10^{23}$ molecules/m^{2}s.

The computational particles are introduced in the domain with a velocity sampled from a Maxwellian with zero average. To enforce the mass flux, no computational particles were allowed to leave the computational domain through the orifice. If a particle crossed this surface, it was subjected to a diffuse reflection. At the top of the chamber, a stream boundary condition was used, with properties of the background gas in the large vessel.

The precise sticking coefficient of zinc atoms on the molybdenum coated wafer sides, the uncoated wafer sides, and the chamber walls is unknown. However, it is close to unity on molybdenum, and close to zero on silicon and the chamber walls, since these (unlike the

molybdenum surfaces) were not cleaned prior to the deposition experiment. The sticking coefficient of zinc atoms on the bottom (molybdenum coated) sides of the wafers was therefore estimated to be 0.9, whereas the sticking coefficient on all other cold surfaces (chamber walls and uncoated top sides of the wafers) was estimated to be 0.1. An accommodation coefficient of unity was used for all surfaces. With these estimated values, a good agreement between DSMC predictions and experimental data was obtained, as will be shown below. Also, we will show that the results are not very sensitive to the precise value of the sticking coefficients. Furthermore, it was found that the results are very insensitive to the value of the accommodation coefficient (results not shown).

The zinc layer thickness was determined from the steady state net number flux as found in the simulation, the zinc bulk density (7140 kg/m^3), and the duration of the experimental deposition (300 s).

5.5 Results

The results of the experiments and simulations can be found in figure 5.2. The position on the x-axis is measured radially from the edge of the hole in the wafer. The zinc layer thickness is presented as measured, i.e. this is the deposited layer thickness after 5 minutes. Each figure contains the experimental and numerical results for the deposition on both the bottom and top wafer (on the molybdenum coated side facing the zinc source). The experimental results consist of at most four measurements per wafer per location, as two trenches were etched in each wafer and two measurements are possible per trench. At some locations, mostly near the centers of the bottom wafers, less than four measurements are available. In these cases, an accurate measurement was not possible, e.g. because the zinc layer was damaged.

The top wafer experimental data in figure 5.2(c) show an unexpected and probably erroneous result near the center. The measured thickness decreases steeply toward the center, where a slight increase is expected (as in the other three figures). This is most likely due to a slightly damaged zinc layer.

In general, the measurements and simulations compare very well, with both showing very similar trends. The expected step in the profile on the top wafer can be seen very clearly for the case with the lowest background pressure (figure 5.2(c)). The cases with an intermediate background pressure (figures 5.2(b) for argon and 5.2(d) for helium) also show a step, but less pronounced, while a smooth thickness profile is found in the case with the highest background pressure (figure 5.2(a)). This corresponds to the prediction of the background gas pressure influence as discussed in section 5.3.1. On the bottom wafer, the same effect can be seen due to the shadowing effect of the shutter plate. It is easily seen that the simulations predict these steps and their pressure dependence quite accurately.

As to the background gas species dependence, a clear difference between the deposited layer profile can be observed for the two cases with a background pressure of 0.088 Pa. In the simulated results, the top wafer profile with helium gas (figure 5.2(d)) has a much smoother step than for the case with argon gas (figure 5.2(b)). In the experimental results, this effect

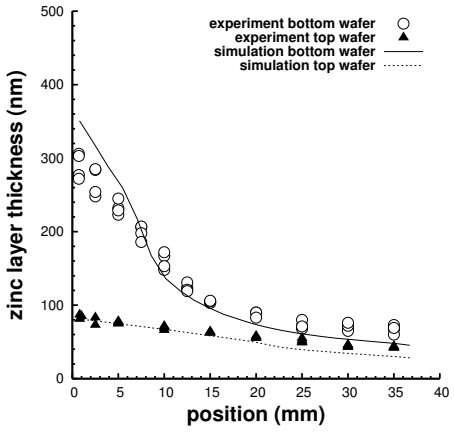

(a) Argon pressure of 0.25 Pa.

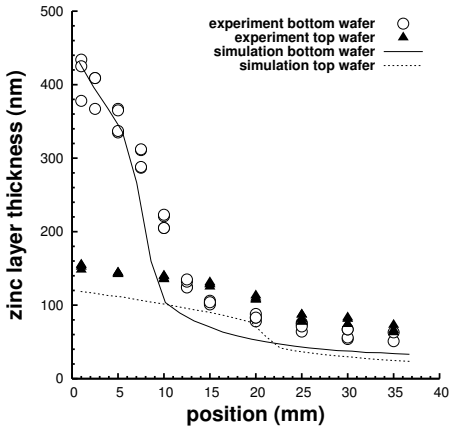

(b) Argon pressure of 0.088 Pa.

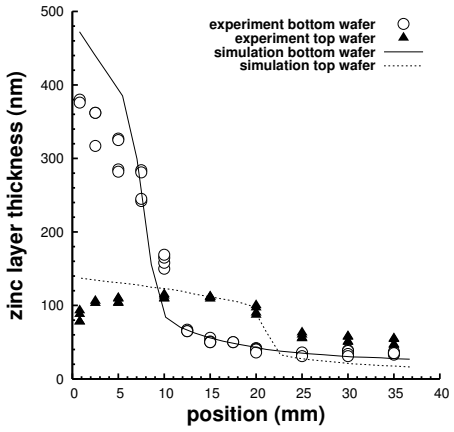

(c) Argon pressure of 0.031 Pa.

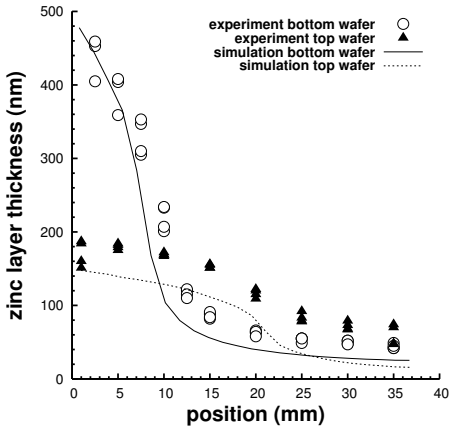

(d) Helium pressure of 0.088 Pa.

Figure 5.2: The experimental and numerical results for the four different experiments.

also seems to be present, although the slightly too large spacing between the measurement locations prevents a definite conclusion.

The most important difference between the simulations and experiments is the tendency of the simulations to under predict the layer thickness when this thickness is small. The 'tail' of the simulated bottom wafer thickness profiles and the entire simulated thickness profiles for the top wafers almost always lie 25 to 50 nm lower than the experimental results.

A possible (partial) explanation for this is the formation of a zinc oxide layer in the period between the opening of the vacuum vessel and the actual thickness measurement. The main oxide formed is zinc hydroxide ($Zn(OH)_2$)[66] and the thickness of this oxide is 3.555 times the thickness of the unoxidized layer. The zinc corrosion rate (measured for one week and linearly [67] extrapolated to one year) is reported as 3 mg/cm^2/year in an unpolluted laboratory atmosphere [66], which can be converted to a measured corrosion layer thickness of 80 nm after one week. In the present study, the corrosion time is approximately 2 hours and no oxide is removed or washed away (as assumed in [67]). In this case, it is reasonable to assume diffusion limited corrosion, i.e. the corrosion rate decreases when the oxidation layer becomes thicker and the layer thickness is proportional to the square root of time. The corrosion in 2 hours then becomes 9 nm. The measured layer will be 22 nm thicker than the layer formed during the experiment.

Another possible explanation for the differences is the used values of the sticking coefficients. The simulations were performed using a fixed value for the sticking coefficient of 0.9 on the treated lower sides of the wafers and a single fixed value of 0.1 on all other surfaces: the cold chamber walls (chrome coated copper), the shutter plate (aluminum), and the top side of the wafers (silicon). The results of the simulations were found to depend slightly on the precise value of the assumed sticking coefficients. For one experimental case, the effect of small variations in the sticking coefficients (0.8-1.0 for the treated wafer sides, 0.05-0.2 for the other surfaces) on the simulation results is plotted in figure 5.3. As can be seen, the effect is rather small and the main trends remain unchanged. For individual experiments, a slightly better agreement between experiments and simulations could be obtained by using the sticking coefficients as fitting parameters, but it was decided to use the same values for all experiments.

Furthermore, the sticking coefficients were assumed to be constant, and thus independent of e.g. zinc atom velocity. It is clear that the ratio between simulated and experimental deposited layer thickness is highest near the center of the bottom wafer, indicating the possibility that the sticking coefficient is lower in this area, where the zinc atoms impact the surface with the highest average velocity. Also, the sticking coefficients need not be constant between consecutive experiments, e.g. due to changes in the surface composition of the chamber walls caused by the thin zinc layer deposited in the previous experiment.

Finally, the uncertainty in the source temperature measurement also influences the results, as can be seen in figure 5.4, in which the simulated source temperature was varied by ±10 K. Again, the effect of the changes does not significantly improve the comparison between simulation and experiment, nor does it affect the main trends.

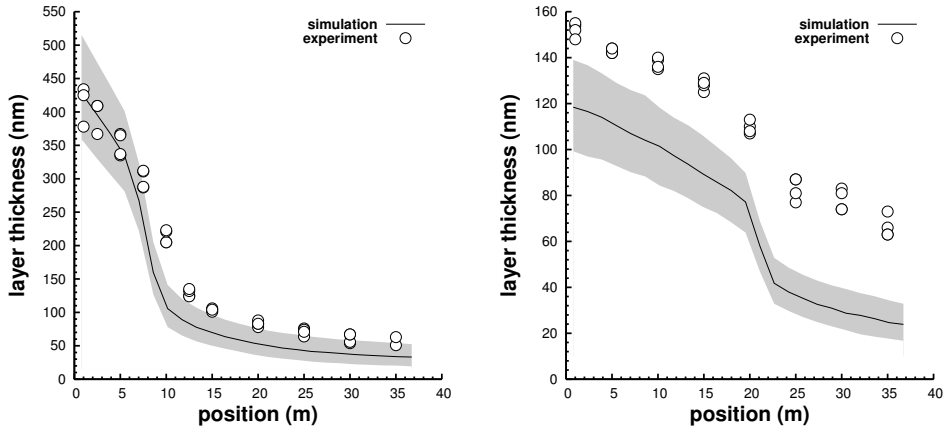

(a) Bottom wafer.

(b) Top wafer.

Figure 5.3: Effect of variation of the sticking coefficients for the case with argon at 0.088 Pa. The solid line is the standard simulation result as shown in figure 5.2 with a sticking coefficient γ of 0.9 on the wafers and 0.1 on the other surfaces. The gray area shows the variation in the results for varying γ, with γ_{wafer} varying from 0.8 to 1.0 and γ_{wall} varying from 0.05 to 0.2.

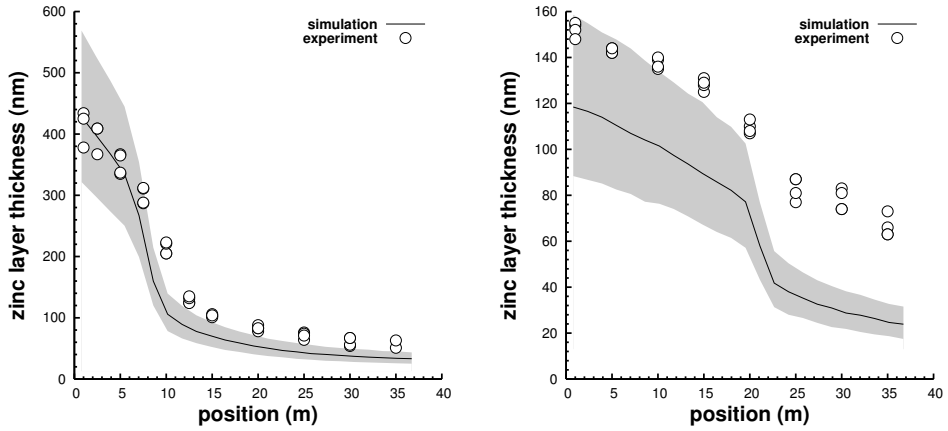

(a) Bottom wafer.

(b) Top wafer.

Figure 5.4: Effect of variation of the source temperature for the case with argon at 0.088 Pa. The solid line is the standard simulation result as shown in figure 5.2 with a source temperature of 700 K. The gray area denotes the variation in the results for temperatures varying from 690 to 710 K.

5.6 Discussion and conclusion

Very little experimental data available in literature is suitable for validation of numerical simulations of rarefied gas flows in low pressure thin film deposition systems. The reason is that to perform accurate validation of a numerical simulation, a very well controlled experiment specifically tailored for the cause is required. All relevant process parameters should be precisely known and well controlled for a validation to be successful.

In practice, this is not easy, as is demonstrated by the current experiment. It was shown that the uncertainties in the sticking coefficients and zinc source temperature directly result in a clearly visible uncertainty in the results. Nevertheless, a reasonable agreement between experimental and simulated results was obtained. Important similarities in deposition layer trends were pointed out and several possible causes for the differences in the absolute values were discussed.

To summarize, the experimental and numerical results show good comparison in trends and reasonable comparison in terms of absolute values, allowing for the conclusion that the Direct Simulation Monte Carlo method in general, and the code that was used for the current research specifically, are suitable for modeling very low pressure deposition processes.

5.7 Acknowledgments

This work is supported by the Netherlands Organization for Applied Scientific Research TNO. The authors wish to thank L. Toonen for his excellent support during all stages of the experimental work.

6. Application of the developed codes to non-continuum internal gas flow processes

This chapter describes two applications of the developed DSMC simulation codes to practical non-continuum internal gas flow problems in science and industry. In section 6.1, the heat flow in a stagnation flow reactor under rarefied conditions is studied, and section 6.2 shows an application of DSMC to thin layer deposition through shadow masks.

6.1 Heat Transfer in Very Low Pressure Stagnation Flow CVD Reactors

This section describes the application of the STARS code to heat transfer problems in a stagnation flow CVD reactor.

The entire section has been published in the Proceedings of Chemical Vapor Deposition XVI and EUROCVD 14 [61] with the title 'Heat Transfer in Very Low Pressure Stagnation Flow CVD Reactors.' The authors are R. Dorsman and C.R. Kleijn. As a result, parts of this section show overlap with other sections in this thesis.

Keywords: DSMC, Rarefied, Heat Transfer, Temperature Jump, Stagnation Flow

6.1.1 Abstract

The heat transfer from the hot susceptor to the flowing gas in a stagnation flow very low pressure CVD reactor is investigated with the DSMC method [1] as a function of Péclet and Knudsen. For simulations with a very low mass flow rate at a pressure of 0.12 Pa, the heat flux at the center of the hot susceptor was found to be 80% lower than the heat flux at a pressure of 1.2 Pa, and 85% lower than the continuum flow predictions by SPIN [68] and FLUENT [69]. For higher mass flow rates, reductions of the heat flux of the same order were found.

Furthermore, large differences were found in the non-uniformity of the heat flux across the susceptor surface. At Kn=0.1, the maximum variation of the heat flux was 100%, while for Kn=1.0, the maximum difference was only 10%. Also a significant temperature jump at the susceptor of up to 40% of the total temperature difference was found.

6.1.2 Introduction

Stagnation flow configurations are frequently used in Chemical Vapor Deposition in order to obtain uniform films on large surface areas. For sufficiently high pressures, the continuum regime equations that describe heat and mass transfer in this geometry are well known, and for simplified one-dimensional problems, analytical solutions exist for mass [18, 70] and heat transfer [70] to the susceptor as a function of the Péclet (Pe) number. To obtain more accurate results, including e.g. non-constant gas properties and multi-component effects, a computational package (e.g. SPIN [68] or FLUENT [69]) can be used.

However, many CVD processes, and especially plasma (enhanced) CVD processes, are run at very low pressures of ~0.1 - 10 Pa. For these low pressures the continuum equations are no longer valid, and other techniques must be used to obtain solutions of heat and mass transfer. This regime, which is called the rarefied regime, is defined using the Knudsen (Kn) number as:

$$\mathrm{Kn} = \frac{\lambda}{D} > 0.01 \tag{6.1}$$

In this equation, λ is the mean free path of the gas molecules, and D is a characteristic length scale of the flow. Conventional CFD solvers, which are based on the continuum Navier Stokes equations, will not be able to solve the flow accurately for this Kn range. Mathematically, this is due to the approximations in the Chapman-Enskog analytical equations for the viscous stress tensor and the heat flux vector, which are used to close the Navier Stokes equations and are only valid in the limit of small Kn. The physical background of this breakdown of the continuum equations stems from the decreased importance of gas phase inter-molecular collisions compared to collisions of gas molecules with solid walls. For small Kn, inter-molecular collisions dominate due to the relatively small mean free path and the gas can be considered a continuum. For larger Kn, the wall collisions start to dominate and the particulate nature of the gas has to be taken into account. One of the simulation methods capable of capturing the particulate nature of a gas is the Direct Simulation Monte Carlo (DSMC) method [1]. This method performs simulations of the flow by calculating molecular movements and collisions using molecular models. DSMC was initially developed for rarefied hypersonic flows, but has also been applied successfully to vacuum systems [71].

In this paper, we present a numerical DSMC study of the heat transfer from the hot susceptor in a low pressure ($\mathrm{Kn} = 0.1 - 1$) stagnation flow CVD reactor, schematically illustrated in figure 6.1. Variation of the heat transfer from the hot susceptor to the cold gas with changing Pe and Kn numbers will be presented.

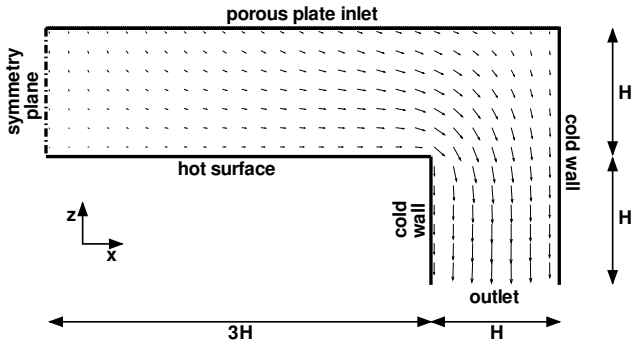

Figure 6.1: The stagnation flow geometry used in the calculations. The geometry is 2D, and H is 0.05m.

6.1.3 Continuum regime solutions

For the continuum regime, models exist for the one-dimensional heat transfer from the center of the impingement surface. Often, the following equations are used:

$$a\frac{d^2T}{dz^2} = v_z\frac{dT}{dz} \tag{6.2}$$

$$\Phi = -k\frac{dT}{dz} \tag{6.3}$$

where a is the thermal diffusivity, T the temperature, z the height above the surface, v_z the velocity in the z direction, Φ the heat flux and k the thermal conductivity. If the boundary conditions are $T(z=0) = T_s$ and $T(z=H) = T_H$, then a solution of 6.2 can be found using $v_z(z) = v_z(z=H)z/H$ as an approximation for the velocity (which is valid close to $z=0$), the assumption that the density is constant, and the following definitions for dimensionless variables: $\mathrm{Pe} = Hv_z(z=H)/a$, $z' = z/H$ and $T' = (T-T_s)/(T_H-T_s)$. The solution is then [70]:

$$T' = \frac{\mathrm{erf}\left(\sqrt{\frac{\mathrm{Pe}}{2}}z'\right)}{\mathrm{erf}\left(\sqrt{\frac{\mathrm{Pe}}{2}}\right)} \tag{6.4}$$

Is this equation, erf denotes the error function. From this equation, the dimensionless heat flux Φ', defined as $\Phi' = \Phi H/(-k(T_H - T_s))$, can be written as:

$$\Phi' = \sqrt{\frac{2}{\pi}} \frac{\sqrt{\mathrm{Pe}}}{\mathrm{erf}\left(\sqrt{\frac{\mathrm{Pe}}{2}}\right)} \tag{6.5}$$

Note that the dimensionless temperature and heat flux at $z = 0$, only depend on the Pe number.

In the derivation of equation 6.2, it is assumed that the thermal conductivity and the specific heat for constant pressure are constant. Equation 6.3 is only valid in the limit of small Kn. The assumption of constant specific heat is accurate for most CVD process conditions, but when the temperature varies between ~300 K in the inlet and 400-600 K at the susceptor, as common in CVD reactors, the thermal conductivity can no longer be assumed constant. The assumption that the density is constant, which is used to obtain 6.4, is also not accurate. To be able to obtain accurate results for the continuum regime including variable gas properties as predicted by the kinetic gas theory, the SPIN [68] and FLUENT [69] programs were used. These programs use finite difference approximations to solve the basic equations of this problem. SPIN solves the 1-dimensional equations at the center of the susceptor, while FLUENT can solve the entire 2-dimensional problem.

6.1.4 DSMC

The DSMC method

The DSMC method is based on the uncoupling of molecular motion and intermolecular collisions. Using this approximation, which is only valid for very small time steps and depends on Kn and the local temperature, a flow is simulated by calculating molecular paths. Because the number of molecules in a realistic flow is too large to be simulated by any computer (e.g. 1 liter of gas at 1 Pa contains $\sim 10^{17}$ molecules), the number of particles in a simulation is only a fraction of the actual number, such that every simulation particle represents F real molecules, with $F \gg 1$. The resulting number of simulation particles is too small for any real collisions to occur in the simulation, and therefore collisions are allowed between nearby (and not necessarily touching) particles. These collisions are calculated in a Monte Carlo fashion with a probability chosen in such a way that the correct statistics are obtained for the entire flow. Due to the relatively small number of particles, results for the gas velocity, density, temperature, etc. can only be obtained by sampling over long times in steady flows, or over many ensembles for unsteady flows.

The most used boundary conditions that are applied in DSMC codes are stream, vacuum and wall (diffuse or specular) boundary conditions. At both a stream and vacuum boundary, molecules that cross the boundary are removed from the flow. The difference between stream and vacuum is the inward flux of molecules. At a vacuum, no molecules are entered in the flow, but at a stream boundary, molecules are entered into the flow according to the specified values of the number density n, temperature T, and stream velocity v_s. At a wall, molecules

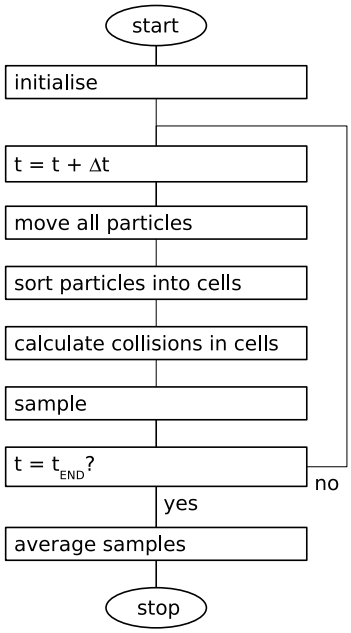

Figure 6.2: Simplified DSMC flowchart.

are reflected back into the flow with specular or (partially) diffusely reflecting conditions. Other possible boundary conditions are symmetry planes, periodic boundaries and porous walls.

DSMC code

A DSMC flow chart is shown in figure 6.2. The main loop of this code can be divided into four sections. First, all simulation particles are displaced by an amount according to their velocity and the size of the time step. During this step, molecule-boundary interactions are also calculated (e.g. collisions with walls, removal of molecules at domain exits, and adding of molecules at inlets).

The next step is the sorting of molecules into cells. This is done for two purposes. First, the collision step needs pairs of nearby molecules for each collision. Due to the sorting, two molecules in a cell are always close enough if the cells are small enough, enabling the selection of pairs of molecules for a collision to occur efficiently. Secondly, the sampling step samples average velocities and energies of the molecules in a cell. Due to the sorting step, this can also be done very efficiently.

The third step is the collision step. In each cell containing N particles, all particle pairs have a certain probability P to collide, depending on the factor F, the collision cross section σ, the relative speed c_r of the two particles, the time step Δt and the cell volume V:

$$P = F\frac{(\sigma c_r)\Delta t}{V} \tag{6.6}$$

The collision step could then consist of calculating, for all $N(N-1)/2$ particle pairs, collisions with probability P, but as P is generally very small, this is very inefficient. The procedure is made more efficient by reducing the number of pair selections and increasing the collision probability such that the maximum probability is 1. In this scheme, the number of potential collision pairs is determined using a maximum value for the product of the collision cross-section and the relative speed $(\sigma c_r)_{max}$, and the time average number of molecules in a cell $\bar{N}$. The number of pair selections is now:

$$\frac{1}{2}N\bar{N}F\frac{(\sigma c_r)_{max}\Delta t}{V} \tag{6.7}$$

and the collision probability of a pair becomes:

$$P = \frac{(\sigma c_r)}{(\sigma c_r)_{max}} \tag{6.8}$$

resulting in the correct average number of collisions. Note that the maximum probability is 1. The calculation starts with a reasonable value for $(\sigma c_r)_{max}$, and if a collision pair is found with a value of (σc_r) greater than the maximum, the maximum is updated. If a collision occurs, the new velocities of the particles are sampled from a post-collision velocity probability distribution which is derived from a molecular model.

The last step is the sampling step, in which the average velocity and energy of the molecules in a cell is sampled. To obtain final results, many of these samples have to be averaged. Note that computational cells in DSMC are used only for efficient selection of nearby molecules in the collision step, and for sampling gas properties in the sampling step, and not for discretization of transport equations as in e.g. finite difference methods.

6.1.5 DSMC numerical setup

The DSMC code used for the simulations is based on the description of the DSMC method in the book by G.A. Bird [1], who first described and applied DSMC. The geometry used for the simulations in this paper is shown in figure 6.1. The distance H between the hot susceptor and the inlet is used as the characteristic length scale for determination of the Kn number. The gas used in the simulations is pure Argon. The inlet is modeled as a porous plate, which behaves as a diffusely reflecting wall for molecules that come from the gas, and as a stream inlet for the gas flowing through the plate into the domain. The impingement surface is a diffusely reflecting wall with a higher temperature than the other boundaries. The outer wall and the

Pe	n (m^{-3})	v_s (ms^{-1})	T (K)	# flux ($m^{-2}s^{-1}$)
10^{-4}	$5.91 \cdot 10^{15}$	100	300	$1 \cdot 10^{18}$
10^{-3}	$5.91 \cdot 10^{16}$	100	300	$1 \cdot 10^{19}$
10^{-2}	$5.91 \cdot 10^{17}$	100	300	$1 \cdot 10^{20}$
10^{-1}	$5.91 \cdot 10^{18}$	100	300	$1 \cdot 10^{21}$

Table 6.1: Settings of the porous inlet in the simulations for different Pe numbers.

Kn	n (m^{-3})	v_s (ms^{-1})	T (K)	p (Pa)
0.1	$2.74 \cdot 10^{20}$	0.0	300	1.2
0.3	$9.15 \cdot 10^{19}$	0.0	300	0.40
1.0	$2.74 \cdot 10^{19}$	0.0	300	0.12

Table 6.2: Settings of the stream outlet in the simulations for different Kn numbers.

wall between the impingement surface and the outlet are both diffusely reflecting walls. For all three diffusely reflecting surfaces it is assumed that the thermal accommodation coefficient is 1, which means that there is a perfect energetic equilibrium between the wall and molecules that leave the wall after a collision. The left most boundary is a symmetry plane, which is implemented as a specularly reflecting surface, the outlet is defined as a stream boundary. The hot plate is kept at 400 K, and the cold walls and porous inlet are kept at 300 K.

The flow rate at the inlet was varied to obtain a range of Pe numbers from 10^{-4} to 10^{-1}, which corresponds to flow rates of ∼1 - 1000 sccm. The Kn numbers for the background pressure were varied from 0.1 to 1. The settings used to create the molecular fluxes through the porous plate, which determine the Pe number, are listed in table 6.1, and the setting of the outlet parameters, which determine the Kn number, are listed in table 6.2.

6.1.6 Results and discussion

Simulations

All combinations of Pe and Kn from tables 6.1 and 6.2 were calculated with DSMC, except the case with Pe = 10^{-1} and Kn = 1.0. This last exception is due to the fact that the pressure above the hot susceptor increased significantly due to the large influx of molecules with these settings, which made the definition of 'the' reactor pressure and Kn ambiguous. This is also the reason why no Pe numbers higher than 10^{-1} were calculated. The calculations were done on a single AMD Athlon 1800+ processor, and calculation times varied from a day (Kn = 1.0)

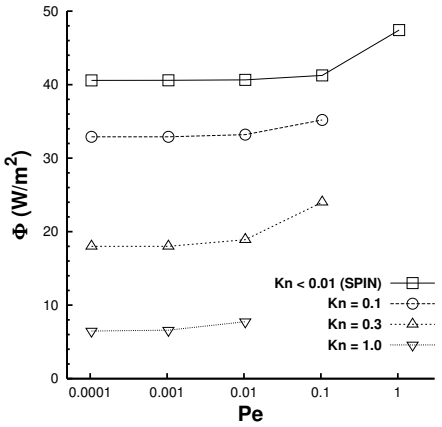

Figure 6.3: Results for the heat flux as a function of Pe for the DSMC simulations and the SPIN calculations.

up to one week (Kn = 0.1). The memory required for the calculations was always below 50 MB.

The results of the SPIN calculations in the continuum limit (Kn $\ll$ 1) were, as predicted by equation 6.5, only dependent on Pe, and therefore only 4 SPIN simulations were done. To be able to compare the heat flux profile across the susceptor as found by the DSMC code, FLUENT was used to solve the Pe = 10^{-2} case.

Heat Transfer

The results for the heat flux from the hot susceptor to the flow at $x = 0$, as a function of Pe and Kn are shown in figure 6.3. It can be seen clearly that the heat flux drops significantly with increasing Kn number. This was expected because it is known that the thermal conductivity of a gas decreases for increasing Kn in the rarefied regime. In the continuum regime, the thermal conductivity of a gas is a constant, and independent of the pressure. In the free molecular regime (Kn > 10), the thermal conductivity can be derived from the kinetic gas theory, and decreases with increasing Kn number.

It can also be observed that the DSMC simulations show the same trend as the SPIN calculations, namely a constant heat flux for very low Pe numbers, and an increasing heat flux for higher Pe. For high Kn, this increasing trend starts at lower Pe than for low Kn, due to the fact that, for equal Pe, the ratio of the number flux of molecules that is entered per second (which is constant for constant Pe) and the (average) total number of molecules in the space between the inlet and the hot susceptor (which depends mostly on Kn) is higher for higher

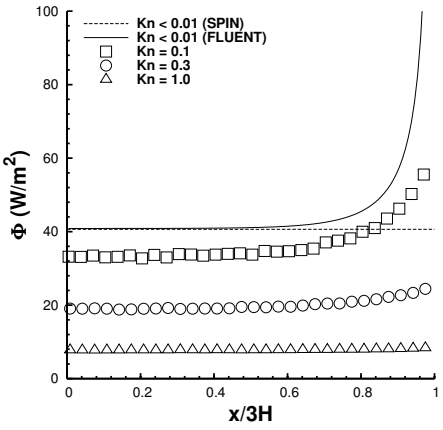

Figure 6.4: Heat flux profiles across the susceptor surface for Pe = 10^{-2} with DSMC, SPIN and FLUENT.

Kn. This means that for higher Kn, the heat flux will change more when Pe is increased. Note that the Kn number of the simulations was determined by the settings of the outlet, and that the actual Kn number in the space between the inlet and the hot susceptor is actually somewhat different, due to the increased pressure in the stagnation region (which lowers Kn) and an increased gas temperature above the hot susceptor (which increases Kn). This means that the simulations with low Pe have a higher Kn in this region, and the simulations with high Pe have a lower Kn. Care was taken to let these effects on Kn remain small, but it cannot be prevented that slight effects occur.

The heat transfer across the hot susceptor is shown in figure 6.4 for Pe = 10^{-2} and several Kn. The SPIN program only gives results for the heat flux at $x = 0$, and therefore the heat flux at Kn < 0.01 was assumed to be this value across the entire surface. It can be seen that, for Kn = 0.1, the profile is far from flat for large x, while at Kn = 1.0, the heat flux profile is relatively flat. The ratios of the heat flux at $x = 3H$ and at $x = 0$ are 2.0 for Kn = 0.1, 1.3 for Kn = 0.3 and 1.1 for Kn = 1.0. The FLUENT simulation clearly shows the same trend of an increasing heat flux close to the edge of the susceptor. It is also clear that the profiles found by the DSMC code approach the continuum solution for decreasing Kn. For the DSMC simulations for the other Pe numbers, results very similar to those shown were found.

Temperature Jump

Figure 6.5 shows the temperature profile at $x = 0$ as a function of z'. It is clear that there is a significant temperature jump, both at the hot susceptor (which is at $z' = 0$) and at the porous

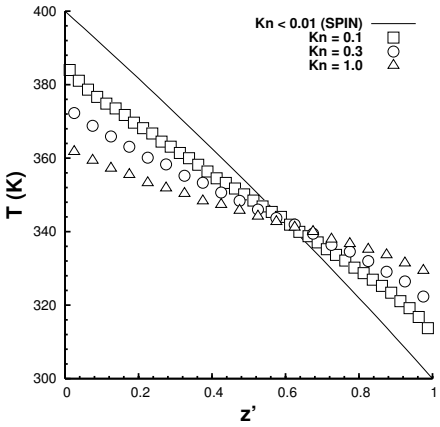

Figure 6.5: Temperature profiles for the Pe = 10^{-4} calculations with DSMC and SPIN. The z' coordinate is a dimensionless height as defined in 6.4.

inlet plate (at $z' = 1$). This is a well known effect in the rarefied regime. It is clear that the size of the temperature jump increases for increasing Kn number, as was to be expected. The temperature jump at the hot susceptor ranges from approximately 15 to 40 K for Kn from 0.1-1. At the porous inlet, the temperature jump ranges from 10 to 30 K. The results for higher Pe numbers are very similar to those presented in figure 6.5.

Effects on CVD reactors

The effects of the decreased heat transfer at low pressures can have a significant effect on the operation of CVD reactors, especially since it can be expected that the mass transfer will also decrease at lower pressures. The temperature jump at the hot susceptor surface may have a significant effect on activated surface reactions [72]: impinging molecules have a significantly lower energy than could be expected from the continuum theory. As these processes are essential to a successful CVD process, it is important that these effects are studied carefully. The DSMC code that was used for this research will be expanded in the coming years, to enable full 3D simulations with all chemical species and reaction mechanisms needed for accurate simulation of CVD reactors.

6.1.7 Conclusions

The heat transfer from a hot susceptor to the gas was studied for a stagnation flow CVD reactor with varying Pe an Kn numbers using the DSMC method. A significant decrease

of heat transfer was found for increasing Kn. At a Kn number of 1.0, the heat flux at the center of the susceptor for very low Pe was found to be about 80% less than the heat flux at Kn=0.1 and almost 85% lower than the heat flux predicted by the continuum SPIN and FLUENT models. Also, large differences in the variation of the heat flux profile across the susceptor surface were found, with differences between the heat flux in the center and at the edge of the surface of 100% for Kn=0.1 and only 10% for Kn=1.0. The heat flux profiles found by the DSMC code approached the continuum FLUENT solution for decreasing Kn. In addition, significant temperature jumps of up to 40% of the total temperature difference were predicted in all DSMC simulations. It can be concluded that, for very low pressure reactors, the widely used continuum models can over predict heat transfer rates significantly, and a simulation model must be used that is based not on continuum assumptions, but on the molecular properties of a gas. The large advantage of DSMC is that temperature jumps and other rarefied gas phenomena are predicted by the code, instead of being supplied to the code as a special boundary condition.

6.1.8 Acknowledgment

This work is supported by TNO.

6.2 Thin film deposition through a shadow mask

This section describes the application of the STARS code to the deposition of a thin metal patch on the surface of a silicon wafer using a shadow mask technology.

This research has been performed in collaboration with R.M. Tiggelaar of the Biosensors/ Lab-on-a-Chip group of the University of Twente (faculty of Electrical Engineering, Information Technology and Mathematics department). The text in this section is based on an article entitled 'Widening of deposited thin-film metal patterns on non-planar surfaces using a shadow mask micromachined in Si(110)' that was submitted to the Journal of Vacuum Science and Technology A [73]. The authors are R.M. Tiggelaar, R. Dorsman, J.W. Berenschot, C.R. Kleijn, M.C. Elwenspoek and J.G.E. Gardeniers.

6.2.1 Introduction

An important trend in microelectromechanical systems (MEMS) is the development of increasingly complex 3D micro structures with integrated functionality. An example of this trend is the work by Tiggelaar et al. [74, 75] on the fabrication and application of a microreactor designed for catalytic reactions at high temperatures (> 600 °C), e.g. the catalytic partial oxidation of methane into synthesis gas. A schematic overview of the microreactor flow channel is given in figure 6.6.

During reactor operation, the metal catalyst patch inside the reactor is heated by a heater outside the flow channel. A reactive gas flow is then introduced in the reactor, and conse-

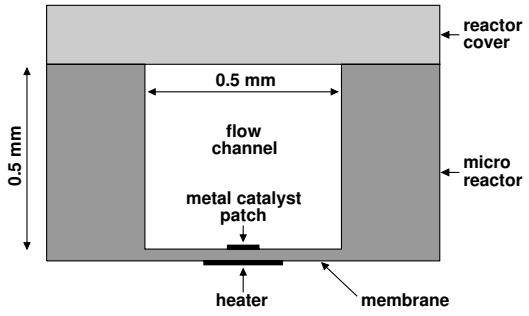

Figure 6.6: Cross-section of the microreactor flow channel. The flow direction is perpendicular to the page. Dimensions are approximate.

quently, a reaction occurs at the catalytic surface. A microreactor has many advantages for studying chemical reactions. The high surface-to-volume ratio leads to increased heat and mass transfer rates, which allows very fast reaction control (e.g. fast heat up of reactants). The use of microreactors also allows excellent control of exothermic reactions, as well as the possibility to create experimental conditions that cannot be achieved in conventional reactors (e.g. temperature window). From the environmental and safety point of view, these small reactors produce only small amounts of waste products, and (for exothermic reactions) only a small, well controllable amount of energy is released during the reaction.

For the fabrication of this reactor, the metal catalyst must be deposited on a thin, and thus fragile membrane. Besides, deposition of the catalyst on the sidewalls of the flow channel has to be avoided to have a well defined system for a kinetic study of the catalytic reactions. The catalytic material should be deposited only on the hottest part of the membrane (the heated center part) in order to prevent formation of secondary products, and the area and thickness of the catalyst layer should be well defined and uniform.

To meet these demands, deposition of the catalyst was performed using a shadow mask process schematically depicted in figure 6.7. The ridges of the mask (note that these ridges are 30 mm long in the x direction) serve as alignment ridges during the positioning of the mask in the flow channel of the microreactor. Note that the gap size must be non-zero to prevent any damage to the membrane. The metal flux is generated by argon sputtering of a metal target, e.g. rhodium or platinum. The combination of the non zero gap size and the non zero y-velocity of the metal atoms leads to a deviation of the deposited metal patch from the ideal top-hat shape with a width equal to the width of the mask window. The result is a patch which is broader than the mask window size, as shown in figure 6.7(b).

As noted above, it is important that this broadening of the metal patch is small and known.

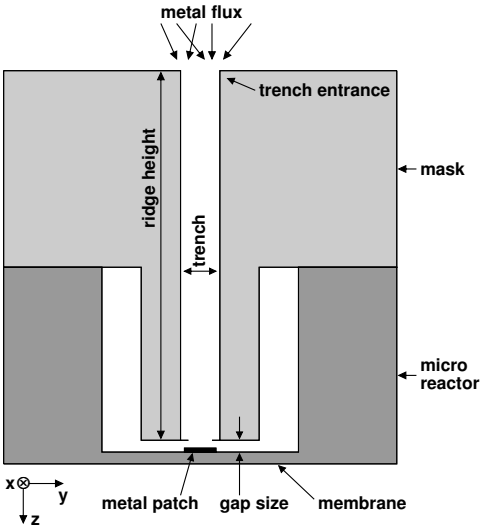

(a) Complete overview.

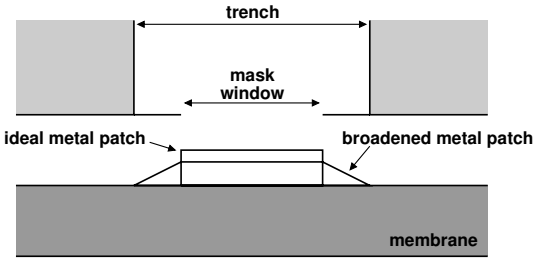

(b) Zoom in.

Figure 6.7: Cross-section of the bottom half of the microreactor and the shadow mask during deposition of the metal catalyst. Shown are a complete overview (figure a) and a zoom in on the metal patch region (figure b). The mask ridges are 1 mm high and ~100 μm wide, the trench is ~125 μm wide, the mask window is 120 μm wide and the gap size varies between 0 and ~150 μm. The zoom in shows the ideal shape of the metal patch and the broadened shape that is obtained experimentally.

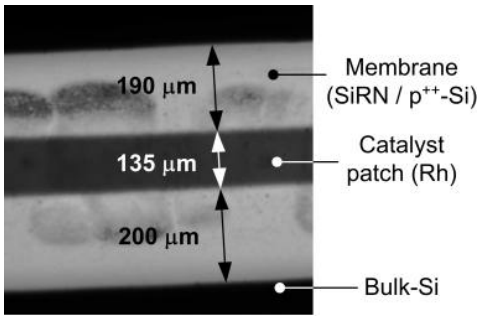

Figure 6.8: Optical microscope picture of a Rh catalyst patch viewed through the thin bottom membrane of the microreactor; the width of the mask window is 120 μm.

Therefore, Tiggelaar studied the broadening experimentally as a function of the gap size [73]. DSMC simulations were performed to find an explanation of the experimentally determined broadening behavior.

6.2.2 Experimental results

In a first experiment, sputter deposition of rhodium was performed in the flow channel of the microreactor, using the described shadow mask. Figure 6.8 shows a typical result for a rhodium catalyst track, viewed through the bottom membrane of the microreactor. It can be seen that the Rh patch was misaligned ca. 5 μm with respect to the center of the membrane, which is mainly due to manual lowering of the 3D shadow mask in the flow channel of the microreactor. No deposit was found on the sidewalls of the flow channel. Broadening of the patch can be seen (patch width is 135 μm, compared to the 120 μm width of the mask window), which is due to a small but non-zero gap (25-35 μm) between mask ridges and membrane.

In a second experiment, the profile of a patch deposited through the shadow mask with a gap size of 25 μm was studied. Figure 6.9 shows the resulting thickness profile (measured with a surface profiler) in the y direction for a Rh deposit through an opening with a size of L_y=120 μm and L_x=4.1 mm. As was already clear from figure 6.8, the patch becomes spread out if the gap between mask and membrane is not zero. Please note that this profile was measured with a surface profiler. A major disadvantage of this type of measurement is the absence of a calibrated baseline, i.e. it cannot be deducted directly from the measurement data which part of the measured film profile is flat (i.e. compared to the substrate surface). Therefore, the measured data are usually corrected by leveling (i.e. by changing the baseline slope) in such a way that the part of the profile that is *assumed* flat is indeed horizontal.

As will be shown below, this has some consequences for the current investigation. The

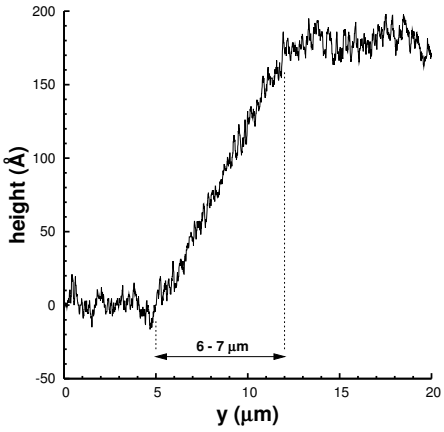

Figure 6.9: Surface profile of the sputtered rhodium patch (window opening 120 μm x 4.1 mm) when the gap is ~25 μm. The y direction in which the measurement was taken is normal to the alignment ridges.

data in figure 6.9 were leveled to obtain a zero slope on the left side of the profile, which was assumed to be the substrate surface. Numerical simulations (that will be discussed below) suggest that this part of the profile is not the substrate surface, but a thin deposited layer which has a small slope in the y direction. The leveled data as shown in figure 6.9 are thus somewhat arbitrary. To illustrate other possibilities, figure 6.10 shows the same experimental data three times with three different baseline slopes. In principle, these three representations of the experimental data are equivalent as the true horizontal baseline is not known. As a consequence, it can not be determined beforehand to which representation (i.e. which baseline slope) the numerical data should be compared. Note that the patch broadening (as indicated by the dashed lines) does not change when a different slope is chosen.

In a final series of experiments, gaps of 0, 25 and 150 μm between the shadow mask and a flat substrate surface were created using spacers. The gap accuracy in all cases was ~15 μm, due to small variations in spacer thickness, as well as a slight curvature of the substrate on which the metal was sputtered. In these experiments, the broadening of the deposited patches in the y direction was measured with an optical microscope (as in figure 6.8). Measurements on the deposited patches were repeated 5 times. For gaps of 25 μm and larger only data for catalyst windows with L_y=120 μm and L_x=4.1 mm and test patterns with L_y=50 μm and L_x=40 μm or 20 μm were found to be useful; smaller test structures were blurred and ill-defined.

In figure 6.11 the broadening of 4 different structures (2 with the same size but at different locations on the mask) of rhodium and platinum is shown as a function of the gap size between

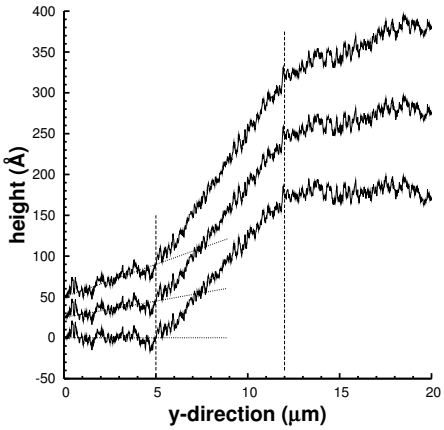

Figure 6.10: The experimental data from figure 6.9 shown three times with different baseline slopes of 0, 4 and 8 Å/μm (dotted lines). The data were shifted vertically by a small amount to prevent overlap at small y. The patch broadening is indicated with dashed lines.

mask and substrate. The broadening is defined as the total width of the sputtered metal patch minus the width of the window in the shadow mask, divided by 2 to obtain the patch broadening on one side. Clearly, for both metals the broadening of the deposited structures increases with increasing gap, the data points suggest a square root (or similar) dependence. Moreover, the broadening increases almost linearly with the width of the window in the y direction, whereas the change in broadening due to a change in the width in the x direction is negligible. The latter was expected because of the large length to width ratio of the trench in the shadow mask (30 mm vs. 125 μm). Due to this ratio, the patch broadening in the y direction can be treated as a 2D problem. Finally, no significant difference in broadening between the two metals is observed.

In order to be able to understand these observations, it is important to establish the properties of the metal atoms when they reach the trench entrance (see figure 6.7(a)). For the used experimental conditions, with a background argon pressure of $6.6{\cdot}10^{-3}$ mbar, the mean free path between collisions is in the range of 7 to 10 mm. With a distance between the sputtering target and the substrate of ~18.5 cm, this means that atoms have undergone more than 20 collisions before reaching the trench entrance. Therefore, hardly any angular preference of atomic movement can be expected at the position of the trench entrance, i.e. there is complete random movement of the atoms.

In the following we will concentrate on the transport inside the trench. The z and y dimensions of the 1 mm deep and 125 μm wide trench are smaller than the mean free path of the atoms in the gas. This implies that atoms that enter the trench will collide (much) more

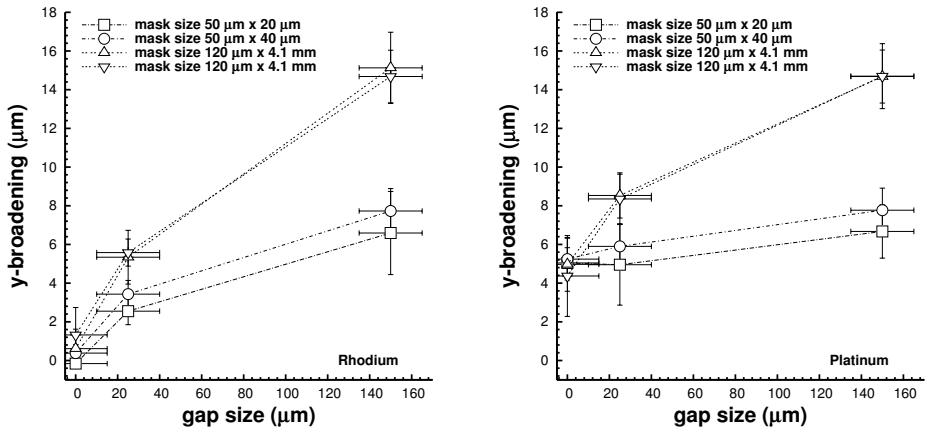

(a) Rhodium.

(b) Platinum.

Figure 6.11: Broadening of sputtered patches of rhodium and platinum as a function of the gap size between the substrate and the mask. The patch broadening was measured (optically) in *y* direction. The sizes of the mask window openings are shown in the legends.

Gap size	Broadening for opening of 50 μm (in y direction)	Broadening for opening of 120 μm (in y direction)
25 μm	2.2 μm	3.1 μm
150 μm	13.1 μm	18.4 μm

Table 6.3: Maximum broadening (as a function of the gap size and the size of the mask opening) in the y direction for a simple line-of-sight model without inter-atom and sidewall collisions, and with a sticking coefficient of unity on all surfaces.

frequently with the sidewalls of the trench than with other atoms. Now, if we assume that atoms which collide with a surface will stick to that surface with unit probability (sticking coefficient γ=1), only those atoms that have traveled from the top opening to the substrate directly (without colliding with the trench surfaces) will lead to growth of the metal patch. This so called line-of-sight model leads to maximum broadening values as shown in table 6.3.

Comparison of these values with the measured values in figure 6.11 shows that for a small gap the measured values are higher than the calculated ones, while for a large gap the measured values are significantly lower. Moreover, for a line-of-sight model with γ=1, the patch broadening increases linearly with the gap size, which is clearly not the case for the experimental data. It can thus be concluded that this simple line-of-sight model cannot be used to describe the spreading in the deposited patches. This seems to indicate that the sticking coefficient γ is not unity in the experiments.

It is known that a γ smaller than unity can occur on smooth and outgassed surfaces [1]. This is the case for the mask and membrane surfaces, both are microscopically smooth and extensively outgassed. Therefore, it is reasonable to assume that for this deposition process, γ can be smaller than unity, although the exact value is unknown. Since analytical solutions for line-of-sight models with $\gamma < 1$ are complicated, the experimental broadening results will be compared to numerical simulations in the next section.

6.2.3 Numerical results

Since the mean free path of atoms ranges from 7-10 mm, inter-molecular collisions inside the trench are relatively infrequent, and the gas flow is almost in the free molecular regime. Therefore, the DSMC method is more or less reduced to a ray tracing method, using straight atomic paths from one surface interaction to the next. The 2D STARS code was used for the simulations.

The DSMC method allows for a wide range of physical phenomena to be included in the interaction of an atom with a surface. The main surface properties relevant for this work are the sticking (γ) and accommodation (α) coefficients.

The accommodation coefficient ($0 \leq \alpha \leq 1$) is the fraction of reflected atoms that undergo diffuse reflection on a surface, i.e. that have a post-collision velocity that is unrelated to the pre-collision velocity. For a fraction $1 - \alpha$ of the reflected atoms, only the normal velocity component is reversed (specular reflection). The use of an accommodation coefficient is a first approximation of the physical phenomena that actually occur during surface interaction. Actually, a single atom is influenced by its interaction with a wall in a way that is neither fully captured by specular reflection, nor by diffuse reflection, i.e. its velocity changes but to some extent remains related to the original velocity. Since the silicon sidewalls of the trench and the membrane are smooth and clean, it is reasonable to assume values for accommodation coefficients below unity [1].

Simulations were performed in a 2D simplification of the geometry (see figure 6.7(b)), including the entire trench and the mask-to-substrate gap. The size of this gap, the sticking and the accommodation coefficients were varied, although each simulation used a single value for γ and a single value for α on both the mask and membrane surfaces. The result of each simulation is a profile of the deposited metal film on the membrane. The height of the profile cannot be compared directly to the height of the experimental profile because the experimental mass flux at the entrance of the trench is not known. However, due to the very nearly free molecular nature of the flow, the shape of the simulated profile can be compared directly to the experimentally observed profile after scaling. In all simulations, a mask opening of 120 μm was used.

In figure 6.12, simulation results for the patch profiles are shown for different values of γ (0.1, 0.5 and 1) and α (0.1, 0.5 and 1) for a gap of 25 μm, as obtained with the DSMC method. The layer thickness in the middle of the trench ($y = 60$ μm) increases with increasing γ and/or decreasing α. Moreover, it is clear that for all cases with $\gamma < 1$, metal is found on the membrane area outside the edge of the shadow mask: the lower the values of γ and α, the larger the patch broadening. Furthermore, from the zoom-in (figure 6.12(b)) near the edge of the mask, it follows that for $\gamma < 1$ the layer thickness already starts to decrease in the area not covered by the mask (at $y > 0$ μm). Simulations for $\gamma = 0.1$ show a very gradual transition in the profile near the edge of the mask, whereas for $\gamma = 0.5$ and $\alpha < 1$ a more pronounced transition is observed. For $\gamma \geq 0.5$ and $\alpha = 1$ there is an abrupt change in film thickness. Please note that, for a sticking coefficient of unity, the value of the accommodation coefficient is not relevant, since there is no reflection of atoms.

Based on these DSMC results and the pronounced but smooth transition measured in the layer thickness at the edge of catalyst patch (figure 6.9), attention is focused on simulations with $\gamma = 0.5$ (figure 6.13). Simulated results were compared to experiments after scaling and correction with a constant offset to match the origins of the measurement and simulation. The baseline slope of the experimental results (see figure 6.10) was chosen such that the beginning and end of both the experimental and numerical profile have an identical slope.

It is found that the simulated patch broadening for the case with $\gamma = 0.5$ and $\alpha = 1$ is significantly smaller than the measured broadening (figure 6.13(a)). Simulations performed with $\alpha = 0.5$ and $\alpha = 0.1$ lead to a patch broadening in much closer agreement with exper-

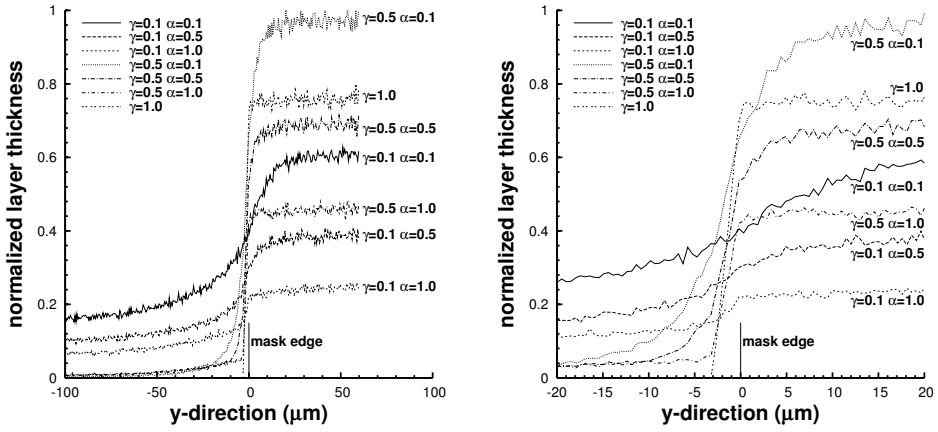

(a) Entire profile.

(b) Zoom-in around mask edge.

Figure 6.12: Simulation results for the deposition profiles at varying sticking (γ) and accommodation (α) coefficients.

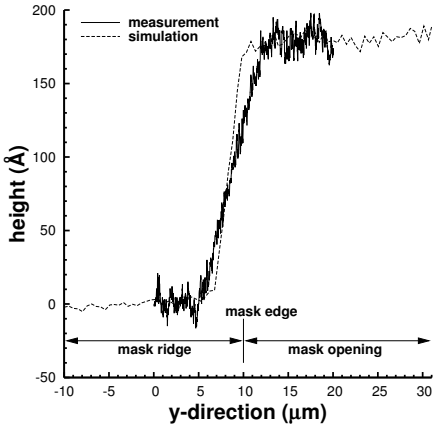

(a) Simulation with $\gamma = 0.5$ and $\alpha = 1.0$. The baseline slope is 0 Å/μm.

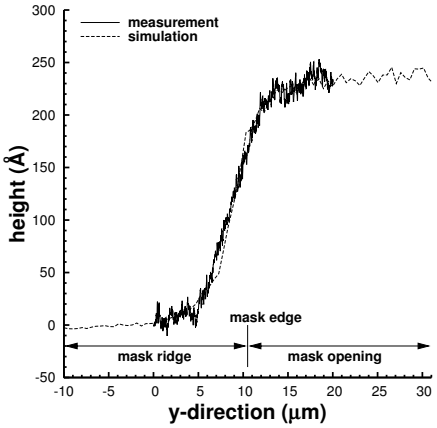

(b) Simulation with $\gamma = 0.5$ and $\alpha = 0.5$. The baseline slope is 3 Å/μm.

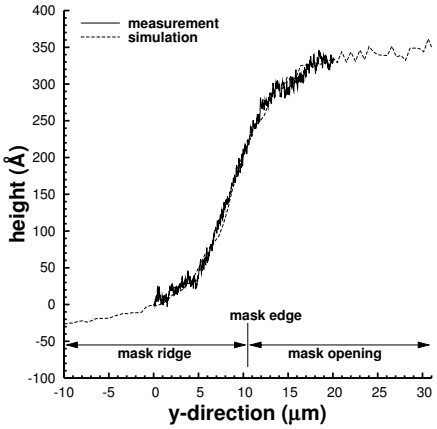

(c) Simulation with $\gamma = 0.5$ and $\alpha = 0.1$. The baseline slope is 8 Å/μm.

Figure 6.13: Comparison of deposition profiles from simulation and experiment. In the simulation results, the origin was shifted and the y axis scale was adjusted to let the results coincide. Different baseline slopes are used for the experimental data (see figure 6.10).

imental data (figures 6.13(b) and 6.13(c)), with the $\alpha = 0.1$ results showing a slightly better comparison to the experimental profile. The almost perfect agreement between experiment and simulation in figure 6.13(c) provides clear evidence that the leftmost part of the experimental profile does not represent the substrate surface but a thin metal layer. This justifies the current procedure in which the baseline slope of the experimental data is treated as a variable.

Summarizing, the experimental film profile for a gap of 25 μm could be most accurately reproduced by the simulations by using a sticking coefficient γ of 0.5 and an accommodation coefficient α of 0.1. The choice for this value of γ was based on the results in figure 6.12, the value of α was based on the data in figure 6.13. It must be noted, however, that only three values for γ and three values for α were considered. Is is very likely that an even better agreement in profile shape can be obtained by minor changes in γ and α. As for the baseline slope of the experimental data, it was found that it's exact value was fixed by the choice of γ and α in the simulations i.e. for a given simulation result, only a single value of the slope was found to be appropriate.

For further simulations, these values of $\gamma = 0.5$ and $\alpha = 0.1$ were used to study the patch broadening as function of the size of the gap between shadow mask and membrane. To be able to compare these simulations to the experimental data in figure 6.11, the numerical broadening was determined using the inflection points of the deposited profile. Note that the experimental data in figure 6.11 were not measured with a surface profiler, but with an optical microscope. With this optical method, it is very difficult to observe ultra thin layers, and the most visible transition is due to the largest gradient in film thickness, which is found between the inflection points. Consequently, the transition from metal patch to membrane surface will be located at the inflection point with the lowest y-coordinate (which is furthest from the center of the mask window).

The method which was used to locate this inflection point is explained in figure 6.14. Two straight lines (dashed lines in the figure) are constructed as a best fit for the two sections of the profile located on the left of the mask edge. The intersection point of these lines is taken as the (outer) inflection point of the deposition profile. The broadening in the deposited patch was then determined as the distance between the mask edge and this inflection point (as indicated in the figure).

This procedure is performed for gaps in the range 5-200 μm, and the resulting values for the broadening in the metal patches are shown in figure 6.15(a). The best fit is a relation in which the broadening scales with the gap size to the power 0.63, closely resembling the relation which was found experimentally in figure 6.11.

Figure 6.15(b) shows the broadening which was determined from the simulations in a different way. The total width of the metal patch was simply determined by a fixed cut-off value. The location where the layer thickness drops below this cut-off is assumed to be the edge of the patch. Different percentages of the maximum layer thickness for a zero gap were used as a cut-off. As can be seen in the figure, the broadening for each cut-off can be approximated to a high accuracy by a linear dependency on the gap size. The line-of-sight model also predicts this linear behavior, although the absolute predictions for the broadening

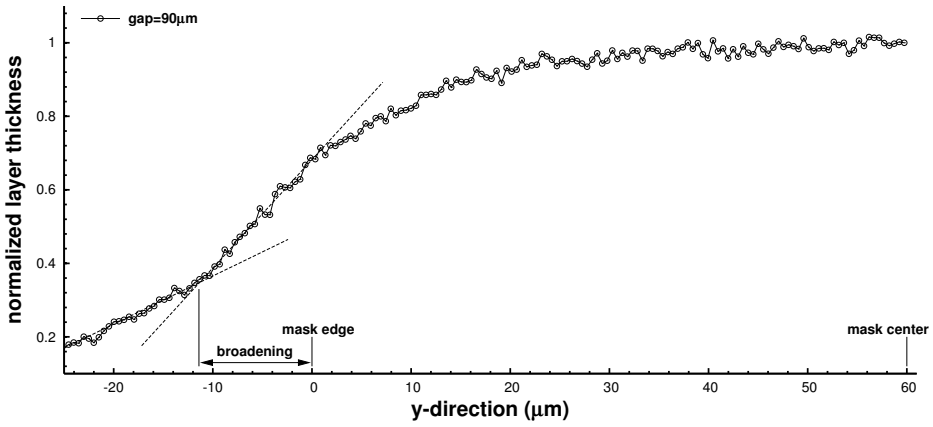

Figure 6.14: Determination of the broadening in the simulated profiles using the inflection point which is located furthest from the mask center.

are smaller that those found in the simulations.

6.2.4 Conclusions

In this section, the application of a 3D self-aligning shadow mask for depositing thin film structures in MEMS technology is discussed. This shadow mask is used for the deposition of metal patches on the bottom membrane of the deep flow channel of a microreactor. The broadening of this patch was investigated experimentally by Tiggelaar [73] as a function of the mask-to-substrate distance, and DSMC simulations were used to explain the experimental results.

The optically determined experimental patch broadening (figure 6.11) shows an approximately square root dependency on the gap size, and the modeled broadening (figure 6.15) matches well with these data, both in terms of the trend and the absolute value. To obtain this excellent agreement, the simulations employed a sticking coefficient of 0.5 and an accommodation coefficient of 0.1, both on the trench walls and on the membrane surface. Furthermore, the numerical broadening was determined using the outer inflection point of the deposited profile. This procedure closely resembles the optical experiments, in which this most visible transition was used to measure the patch broadening.

The numerical results also show a linear relation between the gap size and the broadening, if a fixed cut-off is used to measure the patch width. This behavior corresponds to the linear dependency which is predicted by the simple line-of-sight theory.

In conclusion, it is shown that the observed experimental data can be modeled with a

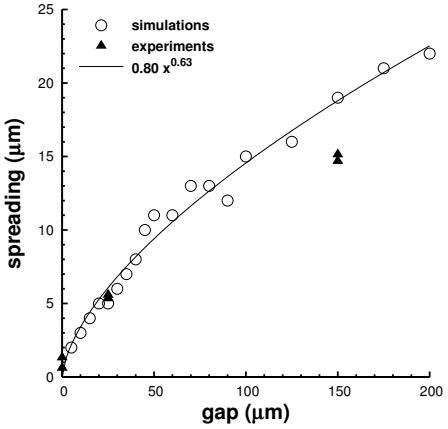

(a) Patch broadening determined using the outer inflection point. The experimental results with Rhodium for a mask window of 120 μm (see figure 6.11(a)) are also shown.

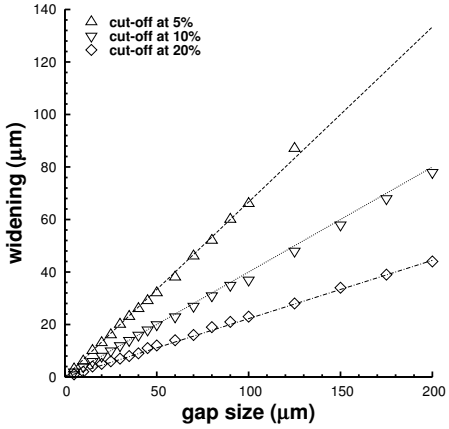

(b) Patch broadening determined using a fixed cut-off.

Figure 6.15: Simulation results for patch broadening in the y direction. Shown are the results obtained using the outer inflection point of the data (on the left, data obtained following the method as shown in figure 6.14) and results obtained using a fraction of the maximum deposition for zero gap size as a fixed cutoff height (right).

molecular gas flow model taking into account values for the sticking and accommodation coefficients below unity.

6.2.5 Acknowledgments

This work was supported by the Dutch Technology Foundation (STW - project 'FORSiM', no. EFC.5134) and by the Netherlands Organization for Applied Scientific Research (TNO). J.W. Mertens is thanked for his assistance in the cleanroom activities.

7. A general correction to surface reaction models based on reactive sticking coefficients

This chapter describes the research that was performed on existing theory for applying a reactive sticking coefficient at a surface.

The entire chapter has been published in Chemical Vapor Deposition [76] with the title: 'A general correction to surface reaction models based on reactive sticking coefficients'. The authors are R. Dorsman and C.R. Kleijn. As a result, some parts of this chapter show overlap with other sections in this thesis. The STARS code was used for the DSMC simulations.

Keywords: DSMC, reactive sticking coefficient, simulation, surface reaction models

7.1 Abstract

Following the work of Coltrin et al., many CVD models express the rate of surface reactions as the molecular flux into the surface, multiplied by a reactive sticking coefficient and a correction factor that was derived by Motz and Wise. According to Motz and Wise, this factor is only valid for small reactive species concentrations, a condition that is not generally fulfilled in CVD processes. Nevertheless, it is widely used in CVD modeling.

In the present study, the Direct Simulation Monte Carlo (DSMC) method was used to determine the deviation from this theory for more general CVD process conditions. The results show that the deviation increases with increasing reactive sticking coefficient and reactant mass fraction, and a significant deviation from the theory of up to 45% was found. A fitted correlation is presented to predict this deviation using the sticking coefficient and the reactant mass fraction for cases with a reactant mass fraction near the surface up to (approximately) 99%.

7.2 Introduction

In CVD process modeling, models have to be used to describe surface reactions. Often surface reactions are described in terms of a reactive sticking coefficient [77, 78, 79, 80, 81, 82, 83], as e.g. presented in the description of Surface Chemkin III by Coltrin et al. [83], which is often used in numerical simulation of CVD systems. Coltrin et al. present two expressions. The first one is an expression that is only valid for very small sticking coefficients. It calculates the reaction rate as the product of the sticking coefficient and the incoming molecule flux equation for an equilibrium gas. The second expression is equal to the first one, but multiplied with a correction factor to account for non-equilibrium effects in the gas in the case of larger sticking coefficients. The correction factor used by Coltrin et al. was taken from an article by Motz and Wise [77], who derived it in the 1960's.

The derivation of the correction factor depends on several assumptions that are not generally satisfied in CVD processes. The purpose of the present work is to study the deviation from the theory in cases where the model assumptions are no longer valid. It is a more elaborate version of the work that was presented earlier [84]. First, the theory as derived by Motz and Wise will be discussed, followed by a description of the method used to solve the problem. Next, the results will be presented and discussed, and finally some conclusions will be drawn.

7.3 Theory

The derivation of a model for surface reactions as performed by Motz and Wise [77] is repeated below in a slightly different form. The starting point is an equation for the number flux of particles of species i at a certain position z in a 1D steady state situation with a concentration gradient, as can be found in the book by Jeans [85]:

$$J_i^{\pm} = \frac{1}{2} n_i \left(\frac{1}{2} c_i \pm w \right) \mp \frac{1}{2} D_i \frac{dn_i}{dz} \tag{7.1}$$

In this equation, $J_i^{\pm}$ is the number flux of species i molecules in the positive (+) and negative (−) z direction. The number density of species i at position z is denoted by n_i, c_i is the mean thermal velocity of species i molecules, w is the mass velocity of the gas mixture and D_i is the diffusion coefficient. To arrive at this equation, Jeans assumes that $w \ll c_i$, that the velocity distribution at each point is Maxwellian and that the length scale associated with the concentration gradient is large in comparison to the mean free path. The net particle flux J_i in the positive z direction can now be defined as:

$$J_i = J_i^{+} - J_i^{-} = n_i w - D_i \frac{dn_i}{dz} \tag{7.2}$$

At a surface, located at position z_0 with the gas located at $z < z_0$, two equations can be used for the net particle flux. The first one follows from equation 7.2:

$$J_i^s = n_i^s w - D_i \left(\frac{dn_i}{dz}\right)^s \tag{7.3}$$

The superscript s indicates that the variable should be evaluated at the surface. The second equation for J_i^s follows from the fact that the number of molecules J_i^{s-} traveling away from the surface is equal to the number J_i^{s+} traveling towards the surface minus the number that react at the surface, so consequently

$$J_i^s = J_i^{s+} - J_i^{s-} = J_i^{s+} - (1-\gamma)J_i^{s+} = \gamma J_i^{s+} \tag{7.4}$$

In this equation, γ is the reactive sticking coefficient, indicating that a fraction γ of the incident species i molecules will react on the surface. Note that in both equations, J_i^s is in fact the net flux of particles towards the surface, which is exactly equal to the surface reaction rate R_i. By combining equations 7.1, 7.3 and 7.4 the following can be obtained:

$$R_i = J_i^s = \gamma J_i^{s+} = \gamma \left[\frac{1}{2} n_i^s \left(\frac{1}{2} c_i + w\right) - \frac{1}{2} D_i \left(\frac{dn_i}{dz}\right)^s\right]$$

$$R_i = \frac{1}{4} n_i^s c_i \gamma + \frac{1}{2}\gamma \left[n_i^s w - D_i \left(\frac{dn_i}{dz}\right)^s\right] = \frac{1}{4} n_i^s c_i \gamma + \frac{1}{2}\gamma R_i$$

$$R_i = \frac{1}{4} n_i^s c_i \gamma \frac{1}{1-\gamma/2} \tag{7.5}$$

The above equation states that the reaction rate R_i is equal to the number of species i molecules that reach the surface in case of a stationary gas ($n_i^s c_i/4$), multiplied by the reactive sticking coefficient and the Motz and Wise correction factor $1/(1-\gamma/2)$. This correction factor is applied to correct for the fact that the gas is not stationary, but has a non-zero gas velocity w in the direction of the surface and a varying number density of the reacting species. Note that equation 7.1 is only valid for $w \ll c_i$, and Motz and Wise state that this means that either the number density n_i of the reacting species must be small compared to the total number density n or that the sticking coefficient must be close to zero. In many actual CVD processes, neither of these conditions is fulfilled.

7.4 Numerical method

To be able to study surface reaction rates described by a reactive sticking coefficient for high reactive species concentrations and high sticking coefficients, a simulation method must be chosen such that the assumptions of the above theory are no longer limiting. This means that the method should:

- not assume an equilibrium Maxwellian velocity distribution,
- not assume a small mass velocity of the gas, and
- not assume that gradients only play a role at length scales much larger than the mean free path.

If these assumptions do not need to be made, accurate solutions of the reaction rate at high reactive species fractions and large reactive sticking coefficients can be obtained. The method chosen for this study is the Direct Simulation Monte Carlo (DSMC) [1] method for simulation of rarefied gas flows.

The DSMC method was designed to numerically calculate rarefied gas flows with a relatively large mean free path, and was first used over 40 years ago for calculations of gas flows around space vehicles. The method is not based on solving partial differential equations, but calculates the flow by calculating the paths and inter-molecular collisions of the molecules in the real flow. The two main assumptions of the method are:

- decoupling of the translation of a computational particle (which represents a molecule in the real flow) and the collision with other computational particles, and
- using only a (very) small number of computational particles compared to the number of molecules in the real flow.

The first assumption means that each simulation time step can be split into two separate steps: a translation step (in which all computational particles are displaced) and a collision step (in which intermolecular collisions take place). This assumption is only accurate for very small time steps, and a general rule of thumb [1] is that the time step should not be larger that one tenth of the mean collision time (the average time between collisions for a molecule in the real flow).

The second assumption means that the simulation does not have to calculate the path of every molecule in the real flow, but can do with only a (very) small statistical sample. A consequence of this assumption is that the collision routines cannot be based on deterministic logic as the collision probability must be artificially increased to let the computational particles have the same collision frequency as the molecules in the real flow. The movement step does not have to be adjusted, and can be kept purely deterministic.

The collisions are calculated using a Monte Carlo type scheme, hence the name Direct Simulation Monte Carlo. The simulation domain is divided into cells with dimension (approximately) $\lambda/3$, where λ is the mean free path. In each time step, the number of collisions in the real flow in this cell is calculated (using the simulated number density) and translated to a number of collisions in the simulation cell (using the ratio of the number of real molecules and simulation particles). When this number is known, a random pair of molecules is selected from the cell (this means their paths do not need to intersect, nor do they have to be close in physical space), for which a collision is calculated. The cell size should be small with respect to the local mean free path to minimize unphysical effects caused by the non-zero distance

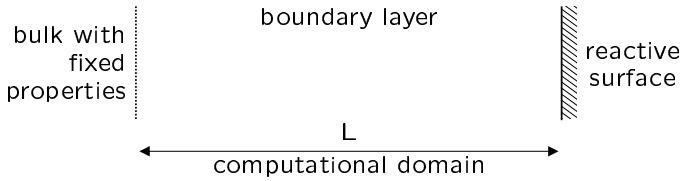

Figure 7.1: The 1D geometry as used in the simulations.

between colliding particles. Also, enough particles should be present in a cell to minimize the occurrence of unphysical repeated collisions between the same two particles. A general rule of thumb [1] in this case is to have at least 15-20 computational particles in a computational cell of size $\lambda/3$ (or smaller).

Due to the very low number of computational particles, accurate results can not be obtained easily, but must be determined by sampling the molecular properties during many time steps (for a steady problem) or many ensembles (for an unsteady problem). The division of the flow domain into cells is used for this sampling as well, meaning that all properties of all molecules within one cell are included in the sampling properties of that cell. One of the drawbacks of the method is that a very large number of time steps is needed to obtain accurate results as the noise associated with DSMC reduces only with the square root of the number of samples. A trade-off has to be made between scatter in the results and computational time.

The method has been applied very successfully in space applications, where (due to the low pressures and long mean free paths) requirements similar to those described above are also relevant. An example is the calculation of the flow field around and the heat transfer to space vehicles during reentry [57, 86]. In more recent years, the DSMC method has also been applied to internal flows, such as CVD reactor-feature scale flows [59], physical vapor deposition [87], and stagnation flows [61].

For the research in the current paper, it is important to note that individual particles are traced in the simulations. This means that the particle velocity distribution is allowed to deviate from the Maxwellian and changes in flow properties on length scales that are small compared to the mean free path can be solved accurately.

7.5 Simulations

The simulations were performed in a 1D boundary layer with a reactive surface on one side and a bulk, with fixed concentrations, temperature and pressure, on the other side as shown in figure 7.1. The bulk gas consists of a non reacting carrier gas and a reactant which reacts at the surface. Note that this reaction is *not* modeled to resemble any existing deposition reaction 'in the real world'. The species used in the simulations have realistic masses and diameters

Variable	H_2	Al	N_2	Xe
Molecular mass (kg)	$3.35 \cdot 10^{-27}$	$44.8 \cdot 10^{-27}$	$46.5 \cdot 10^{-27}$	$218 \cdot 10^{-27}$
Reference diameter (m)	$2.88 \cdot 10^{-10}$	$5.08 \cdot 10^{-10}$	$4.08 \cdot 10^{-10}$	$5.78 \cdot 10^{-10}$
Reference temperature (K)	300	300	300	300
VSS parameter α	1.03	1.18	1.49	1.81
Viscosity temperature index	0.660	0.614	0.769	0.952

Table 7.1: DSMC species data.

(those of H_2, atomic Al, N_2 and Xe), but the simulated reactions can not be related to a 'real life' reaction for any of these species. In the simulations, any reactant computational particle may react when it collides with the surface. At that point, a random number is compared to the reactive sticking coefficient to determine whether a reaction occurs or not. Depending on this, the computational particle is either removed (and counted in the reaction rate) or allowed to go back into the computational domain. No products are formed in the reaction. This modeling of the surface reaction allows investigation of a wide range of reactant-carrier combinations.

To ensure the accuracy of the DSMC simulations, the cell size was set to at most one third of the mean free path, and the time step was chosen such that it was always less than one tenth of the mean collision time. Each cell contained on average at least 20 computational particles of each species. The pressure boundary at the bulk was set as an adaptive inlet boundary using the procedure outlined by Piekos and Breuer [9]. At this inlet boundary, the total pressure, temperature and species concentrations are fixed, while the gas velocity is changed during the simulation to adapt to the velocity inside the domain. The total physical time calculated was 80 ms, of which a quarter was used to reach a steady state. Steady-state properties and fluxes were averaged over the last 60 ms of the simulation. The temperature of the entire system (bulk and surface) is 300 K. For molecular collisions, the Variable Soft Sphere (VSS) [1, 12] model, which is capable of accurately reproducing both viscosity and diffusivity, was used.

A large number of simulations were performed by varying the reactant and carrier molecular properties (see table 7.1), the reactive sticking coefficient γ, the reactant bulk number fraction $x_i^b = n_i^b/n^b$, domain length L, and total pressure p. See table 7.2 for an overview of these variations. Most simulation series were performed using L=25 cm, p=1 Pa and x_i^b=0.5, varying between all three carriers and different values of γ, unless mentioned otherwise. The main series consists of simulations of almost all possible combinations of reactant and carrier species for varying γ. The influence of L and p was independently investigated by simulating Al reactant in N_2 carrier. The influence of moderate bulk fractions (< 0.9) was studied for Al reactant, while the influence of high bulk fractions (> 0.9) was investigated using Xe reactant with γ=0.9.

The calculations were performed using AMD 1533 MHz and 2133 MHz processors, with

Variable	Values
Reactant molecular properties	H_2 Al N_2 Xe
Carrier molecular properties	H_2 N_2 Xe
Sticking coefficient γ	0.1 – 1.0 (in steps of 0.1)
Reactant bulk number fraction x_i^b	0.1 0.5 0.9 0.99 1.0
Domain length L (cm)	5 25 125
Total pressure p (Pa)	0.2 1.0 5.0

Table 7.2: Variables for the simulations.

calculation times ranging from several hours to almost a week. Due to the scatter that is inherent to the DSMC method, scatter is present in the computational results. The results will therefore be treated in a way similar to the treatment of experimental results.

7.6 Numerical results

The dimensionless reaction rate, defined as:

$$R' = \frac{4R_i(1-\gamma/2)}{n_i^s c_i \gamma} \tag{7.6}$$

is calculated for each of the simulations. R' is the ratio between the deposition rate as calculated from the DSMC simulations and the deposition rate according to equation 7.5. The number density n_i^s at the surface is calculated by extrapolating the number densities in the first two cells to the surface. Figure 7.2 shows the dimensionless reaction rate for all simulations. The Motz and Wise theory (equation 7.5) predicts a value of unity for R' for all values of γ. It can be clearly seen that the reaction rates in the simulations significantly exceed this theory. The difference is very small for small γ, and starts to be significant ($> 5\%$) at a value of γ of approximately 0.5. The maximum difference is 45% in a case with undiluted Xe reactant at γ=0.9, L=25 cm and p=1 Pa. It is also clear that the deviation increases for increasing values of γ.

From the simulation results, it was found that the average velocity v_i of the reactant molecules near the surface is not small compared to the average thermal velocity c_i for high values of γ, see figure 7.3. The figure shows that at least one of the assumptions that were needed to arrive at equation 7.5 is no longer valid, which explains the deviations from theory. The observation from figure 7.2 that the deviation from theory is larger for higher values of γ is supported by the trend in figure 7.3 that the average reactant velocity is larger for higher values of γ, indicating a more serious violation of the assumptions underlying equation 7.5.

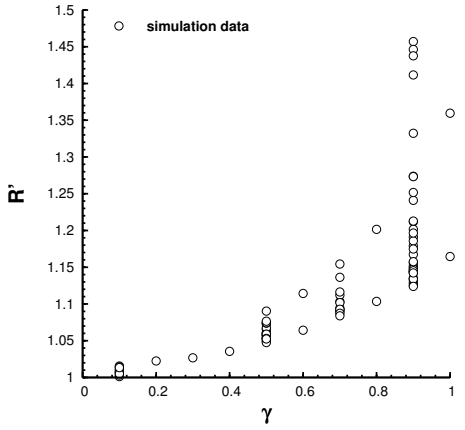

Figure 7.2: Dimensionless reaction rate R' for varying γ. Presented are the results for all simulations, performed at varying p, L, x_i^b, γ and reactant-carrier combinations.

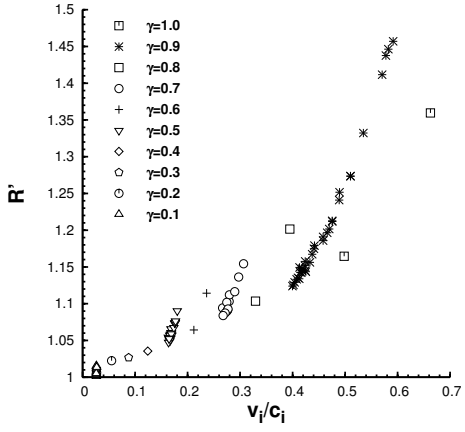

Figure 7.3: Deviation from the Motz and Wise theory as a function of the ratio between the average molecular velocity v_i of the reactant, and its average thermal velocity c_i.

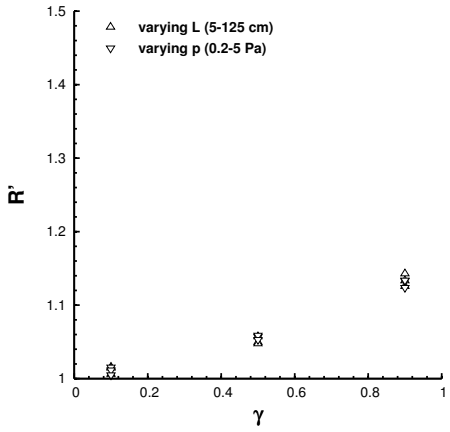

Figure 7.4: Variations in the dimensionless reaction rate R' for varying domain length L and total pressure p. Shown are cases with Al reactant in N_2 carrier and a reactant bulk number fraction of 0.5.

7.7 Parameter study

Figure 7.4 contains the data for Al reactant in N_2 carrier for varying absolute pressure and domain lengths. This figure clearly shows that these variations do not influence the result to the extent as was seen in figure 7.2. The small differences that can be observed are most likely caused by the statistical scatter inherent to DSMC.

The influence of variations in carrier gas species and reactant bulk number fractions x_i^b are shown in figure 7.5. The change from heavy (N_2 or Xe) to the light H_2 carrier gas causes a significant change in R'. The change in x_i^b also seems to have a small influence on the reaction rate at γ=0.9 in case of a light carrier (H_2). This can easily be understood, as the carrier resistance to the transport of reactant to the surface is smaller when the carrier mass is smaller. This results in a larger average velocity of the reactant, indicating a larger deviation from the assumption that $w \ll c$ and therefore a larger deviation from the theory.

To study the influence of extremely high reactant bulk number fractions, additional simulations with γ=0.9 were performed for the heaviest reactant (Xe) at reactant bulk number fractions of 0.5, 0.9, 0.99 and 1.0. In the latter limit, the carrier gas species should not influence the reaction rate. The results for the reaction rate in these simulations as a function of the reactant mass fraction ω_i^s near the deposition surface are shown in figure 7.6. Note that the number fraction differs from the mass fraction by definition (although they are uniquely related through the mass ratio of the reactant and carrier molecules) and that, for obvious reasons, the reactant fraction near the surface is lower than the reactant bulk fraction. Also

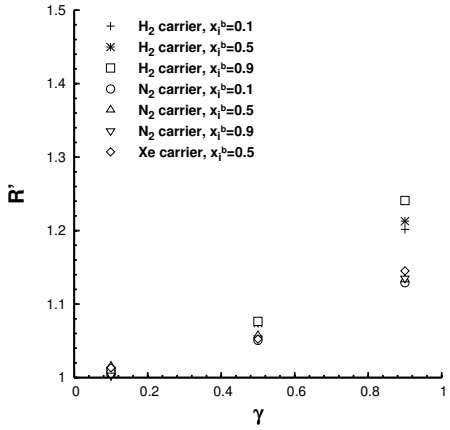

Figure 7.5: Variations in the dimensionless reaction rate R' for varying carrier gas species and reactant bulk number fractions x_i^b. Shown are cases with Al reactant, L=25 cm and p=1 Pa.

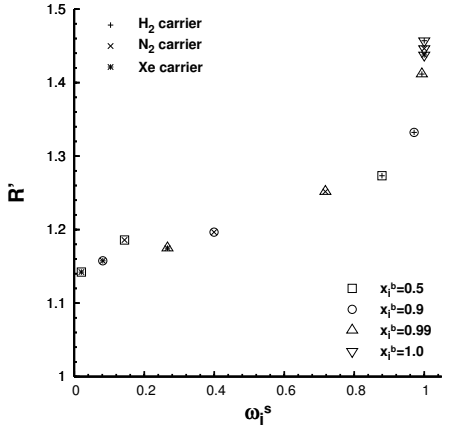

Figure 7.6: The dimensionless reaction rate as a function of the reactant mass fraction ω_i^s near the deposition surface for reactant Xe in various carriers (indicated by the inner part of the symbol) and reactant bulk number fractions x_i^b (marked by the outer part of the symbol). All cases have γ=0.9.

note that, because of a higher diffusion coefficient, the difference between bulk and surface concentration is smallest for the H_2 carrier gas.

It can be concluded that, apart from the sticking coefficient, the reactant-carrier species combination, or more specifically the reactant mass fraction near the surface, is the predominant factor determining the deviation from theory.

7.8 Correlation

The results indicate that the deviation from theory mainly depends on the value of the sticking coefficient γ and the reactant mass fraction ω_i^s near the surface. Theoretical considerations suggest that the mass ratio of reactant and carrier molecules and the Knudsen number play an important role. The mass ratio determines how much the carrier can slow down a reactant molecule in a single collision, while the Knudsen number is a measure for the number of collisions that the reactant molecule will encounter on its way from the bulk to the surface. Also, the Knudsen number is well known as the dimensionless parameter that describes the rarefaction of a flow, and as such it is also an indication of the deviation from the Maxwellian velocity distribution and of the gradient length scales compared to the mean free path. The mass ratio μ and the Knudsen number Kn are defined as:

$$\mu = \frac{m_i}{m_c} \tag{7.7}$$

$$\mathrm{Kn} = \frac{\lambda_i}{n_i^s} \left| \frac{dn_i}{dz} \right|^s \tag{7.8}$$

In these equations, m_i and m_c are the molecular masses of the reactant and carrier, respectively, and λ_i is the reactant mean free path. Kn is based on the dimensionless length of the derivative of the reactant number density n_i. The mean free path of the reactants in our simulations varied from $5.2 \cdot 10^{-4}$ to $1.6 \cdot 10^{-2}$ m, resulting in Knudsen numbers in the range from 0.039 to 1.8. Earlier [84] we proposed an empirical correlation to describe the results in terms of μ and Kn:

$$R' = 1 + 0.047 \cdot \mathrm{Kn} \cdot (\mu + 2.3) \tag{7.9}$$

This correlation is shown in figure 7.7. Clearly, the correlation qualitatively describes the general trend in the simulations, but it fails for high reactant mass fractions. Moreover, in the case of a pure reactant (i.e. no carrier) the meaning of the parameter μ is not clear, which limits the applicability of this equation. Another disadvantage is the inclusion of the Knudsen number. To be able to evaluate this accurately, the reactant mean free path at the surface has to be known, which is not routinely available in CVD simulations.

Therefore, another correlation was constructed which can describe the deviation from the Motz and Wise theory in equation 7.5 much more accurately. Concluding from figures 7.2 and 7.6 that the deviation from the Motz and Wise theory mainly depends on the sticking

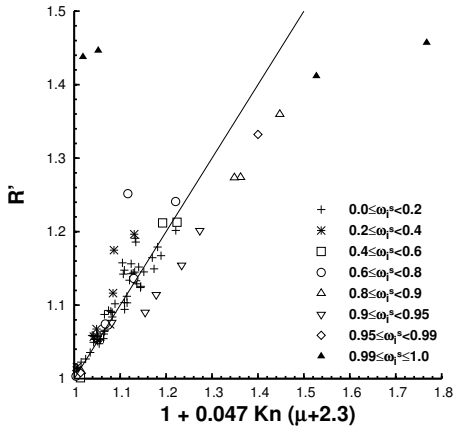

Figure 7.7: Comparison of the simulation data to the correlation in equation 7.9, which is depicted by the solid line. The data points are marked for various ranges of the reactant mass fraction near the surface.

coefficient γ and the reactant mass fraction ω_i^s near the surface, we constructed the following correlation:

$$R' = 1 + 0.19 \cdot \gamma^2 \cdot \left(1 + 0.84\omega_i^s\right) \tag{7.10}$$

The numerical values 0.19 and 0.84 were obtained using a least squares fit on the data. This equation should be seen as an empirical correlation. It was derived from a large number of numerical simulations under strongly varying conditions. Apart from the fact that it should depend on both γ and ω_i^s, we do not propose a theoretical explanation for equation 7.10. Figure 7.8 shows the performance of this equation for all simulation data. It is clear that this correlation performs very well, except for very high (> 99%) reactant mass fractions near the surface. This is in agreement with the results in figure 7.6. The data in that figure approximately lie on a straight line up to surface mass fractions of about 99%. For very small values of γ, the assumptions to the original theory of Motz and Wise are valid and their theory gives the correct result. Under these conditions, equation 7.10 leads to R'=1. Even for very small mass fractions of the reactant, however, equation 7.10 predicts a significant deviation from the Motz and Wise theory for very large values of γ. This is caused by the fact that the average reactant molecular velocity is not negligible (see figure 7.3), which is one of the assumptions to the original theory.

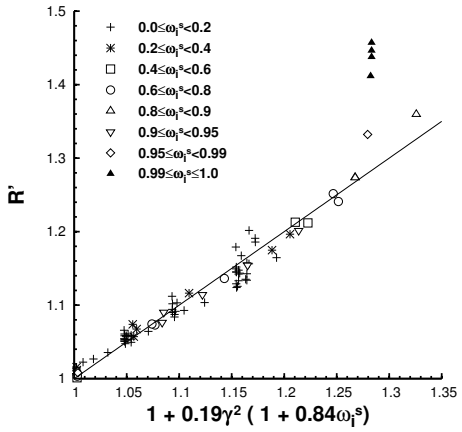

Figure 7.8: The performance of the correlation in equation 7.10, which is depicted by the solid line. The data points are marked for various ranges of the reactant mass fraction near the surface.

7.9 Conclusions and discussion

The results of the present study show very clearly that the model as proposed by Motz and Wise is not valid under all circumstances. A significant deviation from the Motz and Wise theory was found depending on the value of the reactive sticking coefficient γ and the reactant mass fraction ω_i^s near the surface. The cause of this deviation is the assumption used by Motz and Wise that the gas velocity should remain small compared to the thermal velocity. The simulations show that this is not the case under conditions that may readily be encountered in CVD processes. The reaction rate R for species i can be estimated using a newly developed correlation:

$$R = \frac{1}{4} n_i^s c_i \gamma \frac{1}{1-\gamma/2} \left[1 + 0.19 \cdot \gamma^2 \cdot \left(1 + 0.84 \omega_i^s \right) \right] \tag{7.11}$$

This correlation is valid for all values of γ, and near surface mass fractions up to approximately 0.99. It leads to a correction on the predicted deposition rate, which may be as high as 35%. It should be noted, however, that in practice, especially for large γ, deposition is not only determined by surface kinetics, but also by diffusion limitations. Therefore, the effect of the proposed correction may be (much) smaller in practice.

It should be noted that, in the present paper, a PVD process rather than a CVD process has been studied. As a result, no gas-phase reaction products were formed at the surface. While the Motz and Wise theory is applicable to surface reactions with any number of gas-phase reaction products, it is unclear whether the same holds for the proposed correlation. The

creation of one, two or even more gas-phase products, whose motion will oppose the reactant flux towards the surface, will certainly change the reaction rate for any fixed set of boundary conditions. However, equation 7.11 only depends on near-surface properties of the gas, and the effect of gas-phase products might be accounted for by a reduction of ω_i. Future work is needed to resolve this question.

7.10 Acknowledgments

This work is supported by the Netherlands Organization for Applied Scientific Research (TNO).

8. Conclusions

This thesis describes the development, validation and application of two general purpose simulation tools for rarefied reacting internal gas flows, the STARS and X-Stream codes. In section 1.2, the aims for this research were formulated in four questions. Each of these questions will be discussed separately in the next sections.

At the end of this chapter, some final remarks are given.

8.1 Suitability of DSMC to problems in thin film processing

The first research question focused on the suitability of the DSMC method for simulations of reacting rarefied gas flows as encountered in thin film process equipment. This question was divided into three areas, namely the incorporation of physical phenomena, the accuracy of the results and the computational requirements.

8.1.1 Physical phenomena

From the description in chapter 2, it has become clear that the DSMC method itself is very well suitable for simulations of reacting gas flows as found in thin film deposition applications. The method, being designed as a rarefied gas flow solver, is capable of calculating multi-species gas transport phenomena. Besides this, it also has capabilities to include (physical) models for e.g. gas phase chemistry, surface chemistry, trace species and a wide variety of inlet, outlet and surface boundary conditions. For many thin film deposition processes, all of these models are required to take into account all physical phenomena that occur in reality.

8.1.2 Accuracy

In chapter 4, seven different validation cases taken from literature were used to investigate the accuracy of the DSMC method in general, and our two implementations specifically. As the two developed codes (STARS and X-Stream) have a common code base, not all cases were calculated with both codes.

For all of the cases (that represent possible phenomena in thin film deposition equipment), the STARS and X-Stream simulation results matched well with eachother and/or with results of other DSMC codes. Also, a good agreement with experimental data or analytical equations was obtained in almost all cases. In cases where the agreement was not good, satisfactory explanations of the cause of the differences were given.

In chapter 5, an experiment was described that was designed especially for the validation of the DSMC implementations. This experiment, in which a thin metal film was deposited on wafers under varying background gas conditions (i.e. varying Kn), was performed by the author. It was shown that the STARS code can accurately predict the results of these experiments for the entire range of Kn.

Besides the validation from literature and the experiment, the implementations of the gas-phase chemistry (section 4.8) and species weighting factors were also tested (section 4.9). It was shown that the chemistry model functions as expected, i.e. in a steady simulation the reaction rates that were put into the simulation were accurately recovered in the simulation output.

Species weighting factors, which are very important in processes with trace species, were also shown to be accurate, at least up to a weighting factor of 350. In this extreme case, the computation time reduced from almost 880 hours for a simulation without weighting factors to a little less than 10 hours for a computation using weighting factors, while the simulation results remained exactly the same. For other cases with a different (lower) weighting factor, the same results were found, only the time gain was smaller.

Summarizing, it was shown that both the STARS and X-Stream codes, and thus the DSMC method itself, produce reliable and accurate results for a wide range of application areas that are typical for applications in thin film deposition.

8.1.3 Computational effort

In section 3.3.1, the CPU time per time step was shown to be dependent on the Knudsen number. For low Kn, this time varies as $Kn^{-2.4}$ for the 2D STARS code. For 2D X-Stream computations, the same dependency on Kn was found, while for 3D computations, an extra factor Kn^{-1} must be taken into account. The total number of time steps in a calculation depends on Kn^{-1}, leading to the observation that a decrease in Kn of a factor 2 leads to an increase in the total computation time of a factor 11 for 2D and a factor 21 for 3D calculations. This makes high Kn calculations much more feasible than low Kn calculations. Rough estimates of the total calculation time show that simulations of a 2D problem with Kn = 0.03 or a 3D problem with Kn = 0.08 will both last approximately 10 days when performed on 20 CPU's. However, a 2D problem with Kn = 0.1 and a 3D problem with Kn = 0.2 will only require a few days on a single CPU.

Comparing the codes, the calculation time per time step for the 2D STARS code was shown to be 5 times shorter than for the 3D X-Stream code (for an identical 2D problem). For this reason, it is preferable to use the STARS code whenever possible, and to use the X-

Stream code only for true 3D flow problems, or problems with curved surfaces (which cannot be used in STARS).

The parallel scalability of both codes was also investigated (section 3.3.2), and shown to be dependent on Kn. The scaling efficiency increases for decreasing Kn and was shown to reach perfect scalability for some cases. This scaling behavior is very fortunate in view of the calculation time behavior discussed above. For low Kn calculations, the computation time is longer, but at the same time, the parallel scalability improves, allowing very efficient speed up of the calculations through parallelization.

Summarizing, it was shown that the DSMC method is indeed suitable for thin film applications, and is very promising, especially for high Kn flows. For lower Kn, the method is still applicable but calculation times rapidly increase.

8.2 Integration of DSMC into a 3D CFD code

The second research question concerned the integration of the DSMC method into an existing CFD code called X-Stream.

Chapter 3 describes the steps that were taken to be able to convert the previously developed 2D STARS routines to 3D routines which were suitable for a non-orthogonal grid structure. The most fundamental issue in this conversion, which is the determination of the location of computational particles in a non-orthogonal grid, was discussed extensively.

It was concluded that no issues prevented the use of the DSMC method in X-Stream, and the integration was carried out. As described in the previous section, the resulting code has also been applied to several validation problems, and it was shown that the results of these simulations were accurate. Summarizing, the DSMC method was successfully incorporated into X-Stream.

8.3 Experimental input data requirements

The third research question is related to the coupling of simulations and experiments. It focussed on which experimental input data are required for a DSMC simulation of a thin film process, and how uncertainties in these data influence the accuracy of the calculation. Besides the obvious data such as the chamber geometry, inlet flow rates and pump speeds, two types of fundamental information are required.

First of all, it must be noted that the DSMC method is aimed at the calculation of *gas* flows, and is not capable of accurately calculating the interaction of gas molecules with a surface. Information about the gas-surface interaction must be supplied from another source. Possible sources are experimental data and/or numerical calculations based on methods that do have the ability to predict gas-surface interactions, e.g. Molecular Dynamics. It is clear that, in thin film deposition processes, the gas-surface interaction is essential for the growth of the thin film.

Usually, simplifications are made and the complicated interaction is summarized in a value for the sticking and/or accommodation coefficient. The experimental validation (chapter 5), the shadow mask deposition investigation (section 6.2) and the surface reaction rate investigation (chapter 7) all illustrate this approach. In the first two cases, the sticking and accommodation coefficients that were applied were not measured directly, but estimated or fitted by comparing numerical and experimental data. For problems with unknown sticking and/or accomodation parameters, the main consequences of this approach are that experimental results can not be predicted accurately beforehand, and that simulations can only be used to reproduce the experimental data afterwards by using one or both of the coefficients as fitting parameters.

The influence of the accuracy of these parameters on the simulation results can be illustrated using data from chapter 7. It was shown that the reaction rate at a surface is directly related to the sticking coefficient. An error of 10% in the sticking coefficient will lead to an error of at least 10% in the reaction rate (using equation 7.11 while assuming that all other variables remain equal).

Besides the surface interactions, gas molecules also interact with each other, and for this interaction, the molecular collision model (e.g. VHS or VSS) parameters are required. It was shown in section 2.4.2 that these parameters can be deduced from the viscosity and the diffusion coefficient, which can be measured experimentally or calculated using e.g. Lennard-Jones parameters. These data are readily available for a wide variety of gases, and therefore the availability of collision parameters usually does not impede the application of DSMC to thin film processes. The effects of uncertainties in the Lennard-Jones parameters (leading to uncertainties in the DSMC collision parameters) on simulation results have not been studied. However, the excellent agreement between experimental results and numerical simulations throughout this thesis seem to indicate that either the accuracy of the obtained collision parameters is sufficient, or that the uncertainty in these parameters leads to only minor deviations in the simulation results. Further research is required to investigate this matter.

Summarizing, the most crucial data that is required for proper simulations concerns the gas-surface interaction. It has been shown that the use of a sticking and accommodation coefficient is a good first approximation, but these parameters must be supplied to the calculation from an external source. Unfortunately, the simulation results can depend significantly on the exact values of these parameters.

8.4 Influence of rarefaction effects in thin film deposition

The fourth research question concerned the influence of rarefaction effects on gas-surface interactions in thin film deposition applications. To answer this question, two practical problems were investigated:

- the heat transfer in a very low pressure stagnation flow CVD reactor (section 6.1), and
- the reaction rates at surfaces described with a reactive sticking coefficient (chapter 7).

The heat flux to the susceptor in a stagnation flow CVD reactor was studied as a function of the Knudsen and Péclet (Pe) numbers. For very low Pe, it was found that the heat flux to the center of the susceptor decreases significantly for increasing Kn, with a decrease in the flux of 80% between Kn = 0.1 and Kn = 1.0. It was also shown that the heat flux profile becomes more uniform for increasing Kn. While at Kn = 0.1, the heat flux at the edge of the susceptor was 100% higher than in the center, the difference was only 10% for Kn = 1.0. The variation in Pe did not have a large effect on the heat flux in the range (Pe = $10^{-4} - 10^{-1}$) that was studied.

Comparing the results to continuum solutions, it was shown that the DSMC results approach the continuum results for low Kn. In addition, significant temperature jumps of up to 40% (for Kn = 1.0) were predicted, in contrast to the continuum results, which did not include any temperature jump model.

In chapter 7, a more fundamental study is presented on the reaction rate at a surface which is characterized by a reactive sticking coefficient γ. The scope was limited by only investigating surface reactions in which a single molecule sticks to the surface without formation of gas-phase reaction products. It was shown that, for low values of γ ($\gamma \lesssim 0.5$), the widely known and commonly used Motz and Wise theory can be used to accurately predict the reaction rate (with an error less than 5%). For large values of γ, deviations of up to 45% from this continuum theory were found. The cause of this deviation is the assumption in the theory that the gas velocity remains small compared to the thermal velocity. It was shown that the deviation depends on γ and on the mass fraction ω_i^s of the reactant near the surface, and that the reaction rate R can be predicted using this correlation:

$$R = \frac{1}{4} n_i^s c_i \gamma \frac{1}{1-\gamma/2} \left[1 + 0.19 \cdot \gamma^2 \cdot \left(1 + 0.84\omega_i^s\right)\right] \tag{8.1}$$

This correlation is valid for all values of γ, and values of ω_i^s up to approximately 0.99. The above equation is identical to the Motz and Wise theory, except for the term between square brackets. It can thus be concluded that the required correction can be as high as 35%.

Summarizing, it was shown that rarefaction effects can greatly influence heat fluxes and reaction rates in thin film deposition processes. Neglecting these effects in simulations may lead to errors of (at least) an order of magnitude, which is unacceptable in most cases.

8.5 Final Remarks

At the end of this thesis, it can be concluded that the DSMC method in general, and the developed STARS and X-Stream codes specifically, are potentially very valuable tools for the design and optimization of rarefied or free molecular flow devices by means of numerical calculations. Possible applications range from low pressure reactors (e.g. as used in Chemical Vapor Deposition) to microfluidics (e.g. micro thrusters and lab-on-a-chip applications). The accuracy and versatility of the DSMC method, combined with the extensively validated STARS and X-Stream implementations, make this research path a very promising one.

Bibliography

[1] G.A. Bird. *Molecular Gas Dynamics and the Direct Simulation of Gas Flows*. Clarendon Press, Oxford (1994).

[2] L. Boltzmann. Weitere studien uber das wärmegleichgewicht unter gasmolekulen. *Sitzungsberichte Akademie der Wissenschaften Wien*, **66**, pp. 275–370 (1872).

[3] W. Wagner. A convergence proof for Bird's Direct Simulation Monte Carlo method for the Boltzmann equation. *Journal of Statistical Physics*, **66**, pp. 1011–1044 (1992).

[4] P.L. Bhatnagar, E.P. Gross, and M. Krook. A model for collision processes in gases i: Small amplitude processes in charged and neutral one-component systems. *Physical Review*, **94**, pp. 511–525 (1954).

[5] J.C. Maxwell. On the dynamical theory of gases. *Philosophical Transactions of the Royal Society of London*, **157**, pp. 49–88 (1867).

[6] F. Bergemann and I.D. Boyd. New discrete vibrational energy model for the Direct Simulation Monte Carlo method. In B.D. Shizgal, editor, *Rarefied Gas Dynamics: experimental techniques and physical systems, proceedings of the 18th international symposium*, pp. 174–183 (1994).

[7] B.L. Haas, J.D. McDonald, and L. Dagum. Models of thermal relaxation mechanics for particle simulation methods. *Journal of Computational Physics*, **107**, pp. 348–358 (1993).

[8] J.C. Maxwell. On stresses in rarified gases arising from inequalities of temperature. *Philosophical Transactions of the Royal Society of London*, **170**, pp. 231–256 (1879).

[9] E.S. Piekos and K.S. Breuer. DSMC modeling of micromechanical devices. AIAA paper 95-2089, AIAA (1995). Published in the proceedings of the 30th AIAA Thermophysics Conference.

[10] A.L. Garcia. Estimating hydrodynamic quantities in the presence of microscopic fluctuations. *Communications in Applied Mathematics and Computational Science*, **1**, pp. 53–78 (2006).

[11] G.A. Bird. Monte-Carlo simulation in an engineering context. In S.S. Fischer, editor, *Rarefied Gas Dynamics, proceedings of the 12th international symposium - part 1*, pp. 239–255 (1981).

[12] K. Koura and H. Matsumoto. Variable soft sphere molecular model for inverse-power-law or Lennard-Jones potential. *Physics of Fluids*, **3**, pp. 2459–2465 (1991).

[13] K. Koura and H. Matsumoto. Variable soft sphere molecular model for air species. *Physics of Fluids*, **4**, pp. 1083–1085 (1992).

[14] P.S. Larsen and C. Borgnakke. Statistical collision model for simulating polyatomic gas with restricted energy exchange. In M. Becker and M. Fiebig, editors, *Rarefied Gas Dynamics, proceedings of the 9th international symposium - volume 1*, pp. A.7 (1974).

[15] C. Borgnakke and P.S. Larsen. Statistical collision model for Monte Carlo simulation of polyatomic gas mixture. *Journal of Computational Physics*, **18**, pp. 405–420 (1975).

[16] J.O. Hirschfelder, C.F. Curtiss, and R.B. Bird. *Molecular Theory of Gases and Liquids*. Wiley, New York, 4th edition (1967).

[17] R.C. Reid and T.K. Sherwood. *The Properties of Gases and Liquids*. McGraw-Hill, New York, 2nd edition (1966).

[18] K.J. Kuijlaars. *Detailed Modeling of Chemistry and Transport Phenomena in CVD Reactors*. PhD thesis, Delft University of Technology, The Netherlands (1996).

[19] C.R. Wilke and C.Y. Lee. Estimation of diffusion coefficients for gases and vapors. *Industrial and Engineering Chemistry*, **47**, pp. 1253–1257 (1955).

[20] G.A. Bird. Definition of mean free path for real gases. *Physics of Fluids*, **26**, pp. 3222–3223 (1983).

[21] N.G. Hadjiconstantinou, A.L. Garcia, M.Z. Bazant, and G. He. Statistical error in particle simulations of hydrodynamic phenomena. *Journal of Computational Physics*, **187**, pp. 274–297 (2003).

[22] G. Chen and I.D. Boyd. Statistical error analysis for the Direct Simulation Monte Carlo technique. *Journal of Computational Physics*, **126**, pp. 434–448 (1996).

[23] F.J. Alexander, A.L. Garcia, and B.J. Alder. Cell size dependence of transport coefficients in stochastic particle algorithms. *Physics of Fluids*, **10**, pp. 1540–1542 (1998).

[24] A.L. Garcia and W. Wagner. Time step trunctation error in Direct Simulation Monte Carlo. *Physics of Fluids*, **12**, pp. 2621–2633 (2000).

[25] N.G. Hadjiconstantinou. Analysis of discretization in the Direct Simulation Monte Carlo. *Physics of Fluids*, **12**, pp. 2634–2638 (2000).

[26] D.J. Rader, M.A. Gallis, J.R. Torczynski, and W. Wagner. Direct Simulation Monte Carlo convergence behavior of the hard-sphere-gas thermal conductivity for Fourier heat flow. *Physics of Fluids*, **18**, pp. 077102 (2006).

[27] G.A. Bird. New chemical reaction model for Direct Simulation Monte Carlo studies. In B.D. Shizgal, editor, *Rarefied Gas Dynamics: theory and simulations, proceedings of the 18th international symposium*, pp. 185–196 (1994).

[28] G.A. Bird. *Molecular Gas Dynamics*. Clarendon Press, Oxford (1976).

[29] I.D. Boyd. Conservative species weighting scheme for the Direct Simulation Monte Carlo method. *Journal of Thermophysics and Heat Transfer*, **10**, pp. 579–585 (1996).

[30] G.A. Bird. Private communication (2005).

[31] *Tecplot 10 User Manual*. Tecplot, Inc., Bellevue, Washington (2005).

[32] W. Gropp, E. Lusk, N. Doss, and A. Skjellum. A high-performance, portable implementation of the MPI message passing interface standard. *Parallel Computing*, **22**, pp. 789–828 (1996).

[33] *X-Stream User Manual*. The Netherlands Organization for Applied Scientific Research TNO, Delft, The Netherlands (2005).

[34] P. Simons, A. Twerda, R. Verweij, J. Wang, F. Simonis, A. Lankhorst, and B. Paarhuis. X-Stream: the most comprehensive glass furnace simulation tool. In *Proceedings of 2002 Glass Odyssey, 6th European Society of Glass (ESG) Conference*, pp. B1–2 (2002).

[35] J. Verkaik, C. Vuik, B.D. Paarhuis, and A. Twerda. The deflation accelerated Schwarz method for CFD. In V.S. Sunderam, editor, *Proceedings of the International Conference on Computational Science 2005 (ICCS 2005)*, pp. 868–875 (2005).

[36] P. Wesseling. *Principles of Computational Fluid Dynamics*. Springer-Verlag, Berlin (2001).

[37] *X-GUI User's Manual*. The Netherlands Organization for Applied Scientific Research TNO & Femsys Ltd., Eindhoven, The Netherlands (2003).

[38] *FEMGV 7 Release Notes*. Femsys Ltd., Leicester, UK (2004).

[39] I.A. Sadarjoen. *Extraction and Visualization of Geometries in Fluid Flow Fields*. PhD thesis, Delft University of Technology, The Netherlands (1999).

[40] D.N. Kenwright and D.A. Lane. Interactive time-dependent particle tracing using tetrahedral decomposition. *IEEE Transactions on Visualization and Computer Graphics*, **2**, pp. 120–129 (1996).

[41] M.P. Garrity. Raytracing irregular volume data. *Computer Graphics*, **24**, pp. 35–40 (1990).

[42] L.A. Gochberg, R.G. Wilmoth, and A. Krishnan. Radial transition flow between parallel disks: Comparison of computations and experiments. In R. Brun, R. Campargue, R. Gatignol, and J.-C. Lengrand, editors, *Rarefied Gas Dynamics, proceedings of the 21st international symposium - volume 1*, pp. 703–710 (1999).

[43] J.C. Shih, C.-M. Ho, J. Liu, and Y.-C. Tai. Monatomic and polyatomic gas flow through uniform microchannels. In C.T. Avedisian, editor, *Microelectromechanical systems (MEMS), proceedings of the 1996 International Mechanical Engineering Congress and Exposition*, pp. 197–203 (1996).

[44] C. Xie, J. Fan, and C. Shen. Rarefied gas flows in micro-channels. In A.D. Ketsdever and E.P. Muntz, editors, *Rarefied Gas Dynamics, proceedings of the 23rd international symposium*, pp. 800–807 (2003).

[45] H. Legge. Shear stress and pressure in plume impingement flow. In V. Boffi and C. Cercignani, editors, *Rarefied Gas Dynamics, proceedings of the 15th international symposium - volume 1*, pp. 523–538 (1986).

[46] H. Legge. Plume impingement forces on inclined flat plates. In A.E. Beylich, editor, *Rarefied Gas Dynamics, proceedings of the 17th international symposium*, pp. 955–962 (1991).

[47] S. Döring. Experimental plume impingement heat transfer on inclined flat plates. Technical Report 222-90 A 36, DLR (1990).

[48] H. Liu, J. Fan, and C. Shen. Validation of a hybrid grid scheme of DSMC in simulating three-dimensional rarefied gas flows. In A.D. Ketsdever and E.P. Muntz, editors, *Rarefied Gas Dynamics, proceedings of the 23rd international symposium*, pp. 382–389 (2003).

[49] T. Hyakutake and M. Nishida. DSMC simulation of normal, parallel and oblique jet impingements on a flat plate. In R. Brun, R. Campargue, R. Gatignol, and J.-C. Lengrand, editors, *Rarefied Gas Dynamics, proceedings of the 21st international symposium - volume 2*, pp. 561–568 (1999).

[50] P.K. Shufflebotham, T.J. Bartel, and B. Berney. Experimental validation of a direct simulation by Monte Carlo molecular gas flow model. *Journal of Vacuum Science and Technology B*, **13**, pp. 1862–1866 (1995).

[51] T.J. Bartel. Private communication (2005).

[52] D.A. Russell. Density disturbance ahead of a sphere in rarefied supersonic flow. *Physics of Fluids*, **11**, pp. 1679–1685 (1968).

[53] J.-S. Wu, K.-C. Tseng, and T.-J. Yang. Parallel implementation of DSMC using unstructured mesh. *International Journal of Computational Fluid Dynamics*, **17**, pp. 405–422 (2003).

[54] J.-S. Wu and K.-C. Tseng. Parallel DSMC method using dynamic domain decomposition. *International Journal for Numerical Methods in Engineering*, **63**, pp. 37–76 (2005).

[55] R. Dorsman, J.F.M. Velthuis, J.P. Zijp, A.M.B. van Mol, and C.R. Kleijn. Zinc deposition experiments for validation of Direct Simulation Monte Carlo calculations of rarefied internal gas flows. Accepted for publication in the Journal of Vacuum Science and Technology A (2007).

[56] G.A. Bird. Direct simulation and the Boltzmann equation. *Physics of Fluids*, **13**, pp. 2676–2681 (1970).

[57] J.N. Moss and G.A. Bird. Direct simulation of transitional flow for hypersonic reentry conditions. *AIAA paper 84-0223* (1984). Published in the proceedings of the 22nd AIAA Aerospace Sciences Meeting.

[58] A. Kersch, W. Morokoff, and C. Werner. Selfconsistent simulation of sputter deposition with the Monte Carlo method. *Journal of Applied Physics*, **75**, pp. 2278–2285 (1994).

[59] M.L. Hudson and T.J. Bartel. Direct Simulation Monte Carlo computation of reactor-feature scale flows. *Journal of Vaccum Science and Technology A*, **15**, pp. 559–563 (1997).

[60] Y. Sakiyama, S. Takagi, and Y. Matsumoto. Full simulation of silicon chemical vapor deposition process. In T.J. Bartel and M.A. Gallis, editors, *Rarefied Gas Dynamics, 22nd International Symposium*, pp. 206–213 (2001).

[61] R. Dorsman and C.R. Kleijn. Heat transfer in very low pressure stagnation flow CVD reactors. In M.D. Allendorf, F. Maury, and F. Teyssandier, editors, *Chemical Vapor Deposition XVI and EUROCVD 14*, pp. 171–178 (2003).

[62] 'CVD-X' is a general purpose Navier-Stokes and DSMC flow solver developed by TU Delft and The Netherlands Organization for Applied Scientific Research (TNO - Department Industry and Science - PO Box 155, 2600 AD Delft, The Netherlands).

[63] M.L. Hitchman and K.F. Jensen. *Chemical Vapor Deposition - Principles and Applications*. Academic Press, London (1993).

[64] B.S. Meyerson. Low-temperature silicon epitaxy by ultrahigh vacuum/chemical vapor deposition. *Applied Physics Letters*, **48**, pp. 797–799 (1986).

[65] R.C. Weast, M.J. Astle, and W.H. Beyer, editors. *CRC Handbook of Chemistry and Physics*. CRC Press, Boca Raton, Florida, 64th edition (1983).

[66] A. Askey, S.B. Lyon, G.E. Thompson, J.B. Johnson, G.C. Wood, P.W. Sage, and M.J. Cooke. The effect of fly-ash particulates on the atmospheric corrosion of zinc and mild steel. *Corrosion Science*, **34**, pp. 1055–1081 (1993).

[67] American Society for Testing and Materials. *1997 Annual Book of ASTM Standards, volume 03.02*, chapter G1 - Standard Practice for Preparing, Cleaning, and Evaluating Corrosion Test Specimens. ASTM, West Conshohocken, PA (1997).

[68] M.E. Coltrin, R.J. Kee, G.H. Evans, and E. Meeks. *SPIN user manual, version 3.83*. Reaction Design, San Diego (1991).

[69] *FLUENT 5 User's manual*. Fluent Inc., Lebanon (USA) (1998).

[70] N. Shibata and S. Zembutsu. A boundary layer model for the MOCVD process in a vertical cylinder reactor. *Japanese Journal of Applied Physics*, **26**, pp. 1416–1421 (1987).

[71] O. Boulon, R. Mathes, and J-P. Thibault. Direct simulation Monte Carlo method for molecular and transitional flow regimes in vacuum components with static and moving surfaces. *Journal of Vacuum Science and Technology A*, **17**, pp. 2080–2085 (1999).

[72] T.L. Hu and N.G. Glumac. The effects of temperature jump on cvd modeling. *Chemical Vapor Deposition*, **8**, pp. 205–212 (2002).

[73] R.M. Tiggelaar, R. Dorsman, J.W. Berenschot, C.R. Kleijn, M.C. Elwenspoek, and J.G.E. Gardeniers. Widening of deposited thin-film metal patterns on non-planar surfaces using a shadow mask micromachined in Si(110). Submitted to the Journal of Vacuum Science and Technology A (2007).

[74] R.M. Tiggelaar, P.W.H. Loeters, P. van Male, R.E. Oosterbroek, J.G.E. Gardeniers, M.H.J.M. de Croon, J.C. Schouten, M.C. Elwenspoek, and A. van den Berg. Thermal and mechanical analysis of a microreactor for high temperature catalytic gas phase reactions. *Sensors and Actuators A*, **112**, pp. 267–277 (2004).

[75] R.M. Tiggelaar, P. van Male, J.W. Berenschot, J.G.E. Gardeniers, R.E. Oosterbroek, M.H.J.M. de Croon, J.C. Schouten, A. van den Berg, and M.C. Elwenspoek. Fabrication of a high-temperature microreactor with integrated heater and sensor patterns on an ultrathin silicon membrane. *Sensors and Actuators A*, **119**, pp. 196–205 (2005).

[76] R. Dorsman and C.R. Kleijn. A general correction to surface reaction models based on reactive sticking coefficients. *Chemical Vapor Deposition*, **13**, pp. 91–97 (2007).

[77] H. Motz and H. Wise. Diffusion and heterogeneous reaction 3: Atom recombination at a catalytic boundary. *Journal of Chemical Physics*, **32**, pp. 1893–1894 (1960).

[78] C.J. Giunta, J.D. Chapple-Sokol, and R.G. Gordon. Kinetic modeling of the chemical vapor deposition of silicon dioxide from silane or disilane and nitrous oxide. *Journal of the Electrochemical Society*, **137**, pp. 3237–3253 (1990).

[79] M. Frenklach and H. Wang. Detailed surface and gas-phase chemical kinetics of diamond deposition. *Physical Review B*, **43**, pp. 1520–1545 (1991).

[80] M.E. Coltrin, R.J. Kee, and G.H. Evans. A mathematical model of the fluid mechanics and gas-phase chemistry in a rotating disk chemical vapor deposition reactor. *Journal of the Electrochemical Society*, **136**, pp. 819–829 (1989).

[81] M.D. Allendorf and R.J. Kee. A model of silicon carbide chemical vapor deposition. *Journal of the Electrochemical Society*, **138**, pp. 841–852 (1991).

[82] T.J. Mountziaris and K.F. Jensen. Gas-phase and surface reaction mechanisms in MOCVD of GaAs with trimethyl-gallium and arsine. *Journal of the Electrochemical Society*, **138**, pp. 2426–2439 (1991).

[83] M.E. Coltrin, R.J. Kee, F.M. Rupley, and E. Meeks. *Surface Chemkin III*. Reaction Design, San Diego (1996).

[84] R. Dorsman and C.R. Kleijn. A critical evaluation of surface reaction models based on reactive sticking coefficients. In A. Devi, R. Fischer, H. Parala, M.D. Allendorf, and M. Hitchman, editors, *Proceedings of EUROCVD-15*, pp. 65–72 (2005).

[85] J.H. Jeans. *The Dynamical Theory of Gases*. Cambridge University Press (1925).

[86] G.A. Bird. Simulation of multi-dimensional and chemically reacting flows. In R. Campargue, editor, *Rarefied Gas Dynamics, proceedings of the 11th international symposium - volume 1*, pp. 365–388 (1979).

[87] J. Balakrishnan, I.D. Boyd, and D.G. Braun. Monte Carlo simulation of vapor transport in physical vapor deposition of titanium. *Journal of Vacuum Science and Technology A*, **18**, pp. 907–916 (2000).

Dankwoord

Dit boekje markeert de afsluiting van een bijzondere tijd. Ik heb hier vijf jaar aan mogen werken, en ik heb er van genoten. Het was echt een taak die bij mij past, maar die ik zeker niet alleen aan kon. Veel mensen hebben wezenlijk bijgedragen aan het boekje dat u nu vasthoudt.

Allereerst wil ik mijn promotor Chris Kleijn bedanken. Hij vroeg mij, nog tijdens mijn studie natuurkunde, of ik interesse had in een promotieplaats. Daar hoefde ik niet lang over na te denken, en zo begon het avontuur. Chris, ik wil je bedanken voor je dagelijkse begeleiding van mijn project. Je hebt me enorm geholpen om mijn onderzoek te structureren en richting te geven, en je hebt mij ook de ruimte gegeven om mijzelf te ontwikkelen. Onze gezamelijke reizen naar Parijs, Bari (met je gezin), Bochum en Sint Petersburg zal ik nooit vergeten (vooral de vliegreis naar Rusland!). Als laatste wil ik je nog een pluim geven voor je ongeëvenaarde nakijksnelheid. Door snel je goed onderbouwde verbeterpunten aan mij terug te geven heb je er in grote mate aan bijgedragen dat dit boekje zo mooi op tijd af is gekomen.

Naast Chris waren er ook drie mensen vanuit TNO betrokken bij mijn project: Han Velthuis, Ton van Mol en Peter Paul van't Veen. Jullie bijdragen in de begeleidingsgesprekken heb ik erg gewaardeerd, en vooral ook jullie inzet om het validatie experiment van de grond te krijgen. Zonder jullie hulp was dat nooit gelukt.

Bij het uitvoeren van het genoemde experiment (bij TNO Einhoven) was ook de hulp van Leo T. en later ook Leo H. onmisbaar. Jullie hebben heel wat problemen opgelost, en nog belangrijker, jullie hebben er alles aan gedaan om de opstelling te optimaliseren volgens mijn (soms wel exotische) wensen. Daarnaast wil ik Johan Zijp bedanken voor zijn interesse in het project en zijn vakinhoudelijke bijdragen. Ook Frank, Gerwin en Wouter wil ik graag bedanken voor alle gezelligheid tijdens de thee en lunchpauzes. Ik zal de vele dartwedstrijdjes nooit vergeten!

Naast de velen dagen die ik naar Eindhoven afgereisd ben voor het experiment, heb ik ook een tijdje bij TNO Delft rondgelopen om met X-Stream te stoeien. Onder de gezellige begeleiding van Aris en Luuk is dat zeer voorspoedig verlopen, en ben ik niet de weg kwijt geraakt in de enorm uitgebreide X-Stream code. In dezelfde periode is ook de samenwerking met Marcel begonnen. Ik heb het contact met jullie als heel prettig ervaren, en ik zie ernaar uit om met jullie samen te blijven werken.

Naast dit alles heb ik vakinhoudelijk ook nog samengewerkt met Jouke (BSc student), Corina Dam (Radboud Universiteit Nijmegen), Roald Tiggelaar (Universiteit Twente) en Jorrit Posthuma-de Boer (DelftChemTech). Jouke, je was een bijzondere student. Corina en Roald, nogmaals bedankt voor die mooie publicaties waar mijn naam boven mag prijken. Jorrit, ik hoop dat al die simulaties van mij je verder zullen helpen om de MultiTRACK uiteindelijk te begrijpen.

Naast het contact met mijn dagelijkse begeleider Chris, lopen er natuurlijk nog veel meer mensen op het lab rond. Ik heb in die jaren heel wat kamergenoten versleten: Andreas, Martin, Wouter, Hugo, Marco, Axel, Michael, Giannandrea, Roberto, Usama, Snezana en Anton. De één heb ik wat langer gezelschap mogen houden dan de ander, maar zonder jullie zou het wel erg stil zijn geweest. Bedankt!

Ook Roel en Jos van't W. mogen in dit rijtje niet ontbreken, ook al hebben we nooit een kamer gedeeld. Ik heb jullie, en ook Marco, aan het eind van mijn promotie best regelmatig opgezocht, vooral vanwege het feit dat we min of meer tegelijkertijd bezig waren met afronden. Een vraagje over Latex, Tecplot of Gnuplot is aan jullie altijd wel besteed. Ook het bespreken van mogelijke werkgevers bracht een welkome afwisseling in de dagen die voornamelijk met schrijven en plaatjes maken gevuld waren.

Peter Bloom heeft, in zijn functie als systeembeheerder, een hard gewerkt aan de uitbreidingen en de stabiliteit van het cluster. Peter, je bijdrage aan het welzijn van het cluster was van onschatbare waarde, en daarnaast was het ook gewoon heel gezellig om even bij te kletsen. Mede door inzet van jouw kennis draait Linux al jaren probleemloos op mijn PC thuis.

Verder dank aan de andere promovendi, post-docs, stafwerkers en hoogleraren en uiteraard ook de ondersteuners op het secretariaat, in de werkplaats en van CSU. Zonder jullie is het lab niet compleet!

Hoe leuk en gezellig het werk ook was, het was (en is) altijd heerlijk om na een dag hard werken weer thuis te komen bij mijn vrouw Nellie, en mijn dochters Paula en Suzanne. Ik geniet enorm van de liefde die jullie me geven, en ook van jullie steun voor mijn promotie. Het was lang niet altijd makkelijk, maar jullie steun was er altijd. Ook wil ik God, mijn Vader in de Hemel, bedanken voor zijn liefde en zorg voor ons. Zonder Hem kan ik niets doen.

List of publications

- R. Dorsman and C.R. Kleijn, *Heat Transfer in Very Low Pressure Stagnation Flow CVD Reactors*, In: M.D. Allendorf, F. Maury and F. Teyssandier (eds.), Proceedings of Chemical Vapor Deposition XVI and EUROCVD 14, The Electrochemical Society, Pennington, NJ, 2003, pp. 171-178.
- C.E.C. Dam, A.P. Grzegorczyk, P.R. Hageman, R. Dorsman, C.R. Kleijn and P.K. Larsen, *The effect of HVPE reactor geometry on GaN growth rate-experiments versus simulations*, Journal of Crystal Growth, **271**, 2004, pp. 192-199.
- R. Dorsman and C.R. Kleijn, *A Critical Evaluation of Surface Reaction Models Based on Reactive Sticking Coefficients*, In: A. Devi, R. Fisher, H. Parala, M.D. Allendorf and M. Hitchman (eds.), Proceedings of EUROCVD-15, The Electrochemical Society, Pennington, NJ, 2005, pp. 65-72.
- R. Dorsman, J.F.M. Velthuis, A.M.B. van Mol and C.R. Kleijn, *Zinc Deposition Experiments for Validation of DSMC Calculations of Internal Flows*, To be published in the proceedings of the 25th International Conference on Rarefied Gas Dynamics.
- R. Dorsman and C.R. Kleijn, *A General Correction to Surface Reaction Models Based on Reactive Sticking Coefficients*, Chemical Vapor Deposition, **13**, 2007, pp. 91-97.
- R. Dorsman, C.R. Kleijn, J.F.M. Velthuis, J.P. Zijp and A.M.B. van Mol, *Zinc Deposition Experiments for Validation of Direct Simulation Monte Carlo Calculations of Rarefied Internal Gas Flows*, Journal of Vacuum Science and Technology A (in press, 2007).
- R.M. Tiggelaar, R. Dorsman, J.W. Berenschot, C.R. Kleijn, M.C. Elwenspoek and J.G.E. Gardeniers, *Widening of Deposited Thin-Film metal patterns on non-planar surfaces using a shadow mask micromachined in Si(110)*, Submitted to the Journal of Vacuum Science and Technology A.
- C.R. Kleijn, R. Dorsman, K.J. Kuijlaars, M. Okkerse and H. van Santen, *Multi scale modeling of chemical vapor deposition processes for thin film technology*, Journal of Crystal Growth (in press, 2007).

About the author

Ruurd Dorsman was born on September 18, 1977 in Heinenoord, the Netherlands. In 1996, he graduated from secondary school (VWO) at the Scholengemeenschap Johannes Calvijn in Rotterdam. The same year, he started his Applied Physics studies at the Delft University of Technology. During his studies, he was an active member of the Christian students association 'C.S.R. Delft'. In 2002, he received his MSc degree based on his research entitled 'PIV Measurements and Numerical Simulations of Laminar Flows in a Kenics Static Mixer'. The research for this MSc thesis was preformed at the 'Kramers Laboratorium voor Fysische Technologie' (currently a part of the Multi-Scale Physics department). Immediately following his MSc, he started his PhD project in the same group.

Ruurd is married to Nellie, and is the father of two daughters, Paula (2001) and Suzanne (2003).